



Calhoun: The NPS Institutional Archive
DSpace Repository

Theses and Dissertations

1. Thesis and Dissertation Collection, all items

2021-12

STUDY OF COMPOSITE STRUCTURES SUBJECTED TO UNDERWATER SHOCK LOADING

Achor, Caleb H.

Monterey, CA; Naval Postgraduate School

<http://hdl.handle.net/10945/68689>

This publication is a work of the U.S. Government as defined in Title 17, United States Code, Section 101. Copyright protection is not available for this work in the United States.

Downloaded from NPS Archive: Calhoun



Calhoun is the Naval Postgraduate School's public access digital repository for research materials and institutional publications created by the NPS community. Calhoun is named for Professor of Mathematics Guy K. Calhoun, NPS's first appointed -- and published -- scholarly author.

Dudley Knox Library / Naval Postgraduate School
411 Dyer Road / 1 University Circle
Monterey, California USA 93943

<http://www.nps.edu/library>



**NAVAL
POSTGRADUATE
SCHOOL**

MONTEREY, CALIFORNIA

THESIS

**STUDY OF COMPOSITE STRUCTURES SUBJECTED
TO UNDERWATER SHOCK LOADING**

by

Caleb H. Achor

December 2021

Thesis Advisor:

Young W. Kwon

Co-Advisor:

Jarema M. Didoszak

Approved for public release. Distribution is unlimited.

THIS PAGE INTENTIONALLY LEFT BLANK

REPORT DOCUMENTATION PAGE			<i>Form Approved OMB No. 0704-0188</i>	
Public reporting burden for this collection of information is estimated to average 1 hour per response, including the time for reviewing instruction, searching existing data sources, gathering and maintaining the data needed, and completing and reviewing the collection of information. Send comments regarding this burden estimate or any other aspect of this collection of information, including suggestions for reducing this burden, to Washington headquarters Services, Directorate for Information Operations and Reports, 1215 Jefferson Davis Highway, Suite 1204, Arlington, VA 22202-4302, and to the Office of Management and Budget, Paperwork Reduction Project (0704-0188) Washington, DC, 20503.				
1. AGENCY USE ONLY (Leave blank)		2. REPORT DATE December 2021	3. REPORT TYPE AND DATES COVERED Master's thesis	
4. TITLE AND SUBTITLE STUDY OF COMPOSITE STRUCTURES SUBJECTED TO UNDERWATER SHOCK LOADING			5. FUNDING NUMBERS	
6. AUTHOR(S) Caleb H. Achor				
7. PERFORMING ORGANIZATION NAME(S) AND ADDRESS(ES) Naval Postgraduate School Monterey, CA 93943-5000			8. PERFORMING ORGANIZATION REPORT NUMBER	
9. SPONSORING / MONITORING AGENCY NAME(S) AND ADDRESS(ES) N/A			10. SPONSORING / MONITORING AGENCY REPORT NUMBER	
11. SUPPLEMENTARY NOTES The views expressed in this thesis are those of the author and do not reflect the official policy or position of the Department of Defense or the U.S. Government.				
12a. DISTRIBUTION / AVAILABILITY STATEMENT Approved for public release. Distribution is unlimited.			12b. DISTRIBUTION CODE A	
13. ABSTRACT (maximum 200 words) Underwater explosions (UNDEX) produce severe and complex loadings in naval applications. Increased use of composite materials in naval applications requires better understanding of how composite structures will respond and survive an UNDEX. A legacy underwater shock loading method, using liquid nitrogen, was implemented to study the dynamic structural response and failure of flat carbon composite plates. Pressure data was collected using different layouts to study directionality and to characterize the pressure profile of this loading method. A composite test rig was built and utilized to hold composite plates under different backing conditions, water-back (WB) and air-back (AB). Strain response data was collected and analyzed for each composite plate tested. A comparison of water-back and air-back backing conditions was made to better understand the effects of Fluid Structure Interaction in these contrasting backing conditions. Imagery of failure regions was collected, compared, and characterized. Further research is required to validate and more deeply explain the AB and WB comparison results obtained in this research. A compressed air shock pipe underwater release (CASPUR) system was designed and built. Successful initial operational testing of CASPUR was completed. Future pressure profile characterization of CASPUR is needed. Assessment of its efficacy in providing more consistent loading and structure response compared to that of the legacy loading system is required.				
14. SUBJECT TERMS underwater explosions, UNDEX, composite, underwater shock loading, dynamic response and failure, water-back, WB, air-back, AB, compressed air shock pipe underwater release, CASPUR			15. NUMBER OF PAGES 189	
			16. PRICE CODE	
17. SECURITY CLASSIFICATION OF REPORT Unclassified	18. SECURITY CLASSIFICATION OF THIS PAGE Unclassified	19. SECURITY CLASSIFICATION OF ABSTRACT Unclassified	20. LIMITATION OF ABSTRACT UU	

THIS PAGE INTENTIONALLY LEFT BLANK

Approved for public release. Distribution is unlimited.

**STUDY OF COMPOSITE STRUCTURES SUBJECTED TO UNDERWATER
SHOCK LOADING**

Caleb H. Achor
Lieutenant, United States Navy
BS, United States Naval Academy, 2015

Submitted in partial fulfillment of the
requirements for the degree of

MASTER OF SCIENCE IN MECHANICAL ENGINEERING

from the

**NAVAL POSTGRADUATE SCHOOL
December 2021**

Approved by: Young W. Kwon
Advisor

Jarema M. Didoszak
Co-Advisor

Garth V. Hobson
Chair, Department of Mechanical and Aerospace Engineering

THIS PAGE INTENTIONALLY LEFT BLANK

ABSTRACT

Underwater explosions (UNDEX) produce severe and complex loadings in naval applications. Increased use of composite materials in naval applications requires better understanding of how composite structures will respond and survive an UNDEX. A legacy underwater shock loading method, using liquid nitrogen, was implemented to study the dynamic structural response and failure of flat carbon composite plates. Pressure data was collected using different layouts to study directionality and to characterize the pressure profile of this loading method. A composite test rig was built and utilized to hold composite plates under different backing conditions, water-back (WB) and air-back (AB). Strain response data was collected and analyzed for each composite plate tested. A comparison of water-back and air-back backing conditions was made to better understand the effects of Fluid Structure Interaction in these contrasting backing conditions. Imagery of failure regions was collected, compared, and characterized. Further research is required to validate and more deeply explain the AB and WB comparison results obtained in this research. A compressed air shock pipe underwater release (CASPUR) system was designed and built. Successful initial operational testing of CASPUR was completed. Future pressure profile characterization of CASPUR is needed. Assessment of its efficacy in providing more consistent loading and structure response compared to that of the legacy loading system is required.

THIS PAGE INTENTIONALLY LEFT BLANK

TABLE OF CONTENTS

I.	INTRODUCTION.....	1
A.	BACKGROUND AND LITERATURE REVIEW	1
	1. Loading Mechanisms	1
	2. Fluid-Structure Interface	3
	3. Past and Present Experimental Efforts.....	4
	4. Failure Characterization	5
B.	OBJECTIVES	5
II.	METHODOLOGY	9
A.	ANECHOIC WATER TANK.....	9
B.	COMPOSITE TEST RIG	11
	1. Box Design	12
	2. Rail Design.....	17
C.	COMPOSITE PLATES	19
D.	SENSORS AND DATA ACQUISITION	21
	1. Strain Measurement	21
	2. Pressure Measurement	29
E.	LIQUID NITROGEN	31
F.	CASPUR	33
	1. CASS Design.....	34
	2. STR Design	42
	3. Shock Pipe Assembly Design	47
III.	TEST SEQUENCING	53
A.	PRESSURE SENSORS	55
B.	SINGLE SQUARE PLATE WATER BACK.....	57
C.	SINGLE SQUARE PLATE AIR BACK	58
D.	DOUBLE SQUARE PLATE WATER BACK.....	61
IV.	RESULTS AND DISCUSSION	63
A.	PRESSURE RESULTS	63
	1. Linear Layout.....	64
	2. Triangular Layout	70
	3. Standard Layout	73
B.	STRAIN RESULTS	74
	1. Uni-directional Composite (0°)	76
	2. Three-layer Composite (0-90-0°)	84

3.	Four-layer Composite (0-90-90-0°).....	94
V.	CONCLUSIONS	103
VI.	FUTURE WORK.....	105
	APPENDIX A. WHEATSTONE BRIDGE	107
	APPENDIX B. CASPUR OPERATING, TESTING, AND DAQ GUIDE	115
	APPENDIX C. STRAIN RESULTS.....	143
A.	SAMPLE 3, THREE-LAYER COMPOSITE, WB, STRAIN	143
B.	SAMPLE 6, FOUR-LAYER COMPOSITE, WB, STRAIN	145
C.	SAMPLE 7, FOUR-LAYER COMPOSITE, AB, STRAIN	148
	APPENDIX D. PRESSURE RESULTS.....	151
A.	LINEAR LAYOUT PRESSURE RESULTS.....	151
B.	TRIANGULAR LAYOUT PRESSURE RESULTS	154
C.	STANDARD LAYOUT PRESSURE RESULTS	157
1.	Sample 3, Three-layer composite, WB, Pressure	157
2.	Sample 6, Four-layer composite, WB, Pressure.....	158
3.	Sample 7, Four-layer composite AB, Pressure.....	160
	LIST OF REFERENCES.....	161
	INITIAL DISTRIBUTION LIST	165

LIST OF FIGURES

Figure 1.	Surface phenomena for 250-lb HBX-1 at 50-ft depth. Source: [4].....	3
Figure 2.	AWT, top view, showing anti-reflective redwood panels	10
Figure 3.	AWT, side view, showing layered design for damping.....	11
Figure 4.	Overall box design: (a) front view, (b) side view, (c) top view	12
Figure 5.	Backer rod installation to fill internal frame groove to prevent water intrusion	13
Figure 6.	Waterproof sealant used to ensure AB backing condition.....	13
Figure 7.	Layering sequence composite plate installation to box: (a) back window, (b) composite plate, (c) front window.....	14
Figure 8.	Window design for (a) back window and (b) zoomed view of step	15
Figure 9.	Back window design, restricts movement of plate in x-y directions	15
Figure 10.	Front window design, restricts movement of plate in z-direction	16
Figure 11.	(a) Backing clamps (b) retainer-clips for clamped boundary condition	17
Figure 12.	CTR rail design: (a) initial and (b) modified	18
Figure 13.	Overall modified rig design	19
Figure 14.	Cross ply fiber orientations: (a) 0° , (b) $0-90-0^\circ$, (c) $0-90-90-0^\circ$	21
Figure 15.	Three-directional strain gage rosette.....	22
Figure 16.	Wire routing from strain gages	23
Figure 17.	Strain gage wire lead divider to preventing shorting during testing.....	23
Figure 18.	Wheatstone bridge with potentiometers.....	24
Figure 19.	Quarter bridge I circuit layout. Adapted from [22].....	25
Figure 20.	Power supply for Wheatstone quarter bridge I, power turned off	26
Figure 21.	DAQ: SCB68-A NI DMM.....	27

Figure 22.	DAQ: signal processing, NI PXIe-6358	28
Figure 23.	Underwater blast pressure sensor, 138 Series (short length). Source: [26].	29
Figure 24.	Pressure sensor anchor design with hole through bolt shown in top left	30
Figure 25.	Model 482C signal conditioner for pressure data collection	30
Figure 26.	BNC 2110 AI interface with PCB signal conditioner.....	31
Figure 27.	PPV anchor attachment.....	32
Figure 28.	(a) Installed K-type industrial air compressed tank, (b) CGA-590 connection fitting, side-view, (c) CGA-590 connection fitting, front view (brass material).....	34
Figure 29.	Four-port, stainless steel, two-stage regulator, with attached CGA-to-NPT adapter brass fitting	35
Figure 30.	Inlet and outlet HPG-1 and LPG-2 regulator pressure gages	37
Figure 31.	First check-valve, regulator backflow protection	38
Figure 32.	¼ tube connection union tee fitting for venting and isolation	38
Figure 33.	Primary two-way isolation cut-off and venting valve.....	39
Figure 34.	Reducing elbow for hose performance and longevity	40
Figure 35.	Flexible hose for out of water to in-water connection for testing.....	41
Figure 36.	(a) Overall STR design without carriage installed, (b) wet feet guards, (c) recessed guard attachment points	43
Figure 37.	STR in place in AWT (a). Carriage installed onto quad-rails (b).	44
Figure 38.	Carriage design: top-view (a), side-view (b), front-view (c)	46
Figure 39.	Carriage design, front-view, rotational stops	47
Figure 40.	Overall shock tube assembly, (a) side-view, (b) top-view.....	48
Figure 41.	300lb RF flange.....	50
Figure 42.	Rupture disk holder, FAH series: (a) side-view, (b) front-view	50

Figure 43.	Rupture disk holder design: above-view.....	51
Figure 44.	Non-fragmenting stainless-steel rupture disk: (a) inlet side (b) outlet side	52
Figure 45.	Test layout at R = 0.61 m (24 in): (a) top-view, (b) side-view	54
Figure 46.	Pressure sensor layouts: (a) linear (b) triangular (c) standard	56
Figure 47.	Steel piping added to holding tray to overcome buoyant force of CTR.....	59
Figure 48.	CTR stability rails for AB testing	60
Figure 49.	Wire routing for AB CFRP testing set-up.....	61
Figure 50.	Recovered failed pressure vessels from pressure characterization testing	63
Figure 51.	Linear pressure sensor layout. R1 = 0.46 m, R2 = 0.3 m, and R3 = 0.15m	65
Figure 52.	Pressure profile characterization, linear, R = 0.46 m, Run 1	66
Figure 53.	Maximum pressure distribution statistics	67
Figure 54.	Exponential fit for maximum pressure profile.....	68
Figure 55.	Triangular pressure sensor layout and PPV positioning, R = 0.3 m.....	70
Figure 56.	Pressure characterization, triangular results, R = 0.3 m, Run 1	72
Figure 57.	Directionality analysis, triangular results summary, R = 0.3 m	73
Figure 58.	Standard pressure sensor layout for strain DAQ.....	74
Figure 59.	Strain gage numbering sequence, and pressure correlation	76
Figure 60.	Failure of AB Sample 1, unidirectional carbon composite plate, R = 0.46 m	77
Figure 61.	Back side of AB Sample 1, failure characterization, R = 0.46 m.....	78
Figure 62.	Failure of WB Sample 2, unidirectional carbon composite plate, R = 0.46 m	79
Figure 63.	Back side of WB Sample 2, failure characterization, R = 0.46 m	80

Figure 64.	Overall pressure profile (left), plate failure loading (right), AB Sample 1, R = 0.46 m	80
Figure 65.	Overall pressure profile (left), plate failure loading (right), WB Sample 2, R = 0.46 m	81
Figure 66.	Strain response, AB Sample 1 (0°), R = 0.46 m, failure run	82
Figure 67.	Strain response, WB Sample 2 (0°), R = 0.46 m, failure run	83
Figure 68.	Front failure characteristics of WB Sample 3, R = 0.46 m.....	86
Figure 69.	WB Sample 3, failure characterization, R = 0.46 m: (a) back side, (b) zoomed local failure back side, (c) local failure at corner on front of plate.....	87
Figure 70.	Back failure characteristics of AB Sample 4, R = 0.76 m	88
Figure 71.	Front failure characteristics of AB Sample 4, R = 0.76 m.....	89
Figure 72.	Overall pressure profile (left), plate failure loading (right), WB Sample 3, R = 0.46 m	90
Figure 73.	Overall pressure profile (left), plate failure loading (right), AB Sample 4, R = 0.76 m	90
Figure 74.	Strain response, WB Sample 3 (0-90-0°), R = 0.46 m, failure run.....	91
Figure 75.	Strain response, AB Sample 4 (0-90-0°), R = 0.76 m, failure run.....	92
Figure 76.	Normalized WB and AB max x-strain result comparison until failure (0-90-0): (left) tension, (right) compression	93
Figure 77.	Normalized WB and AB max y-strain result comparison until failure (0-90-0): (left) tension, (right) compression	93
Figure 78.	Failure of WB Sample 6, four-layer carbon composite plate, R = 0.15 m	94
Figure 79.	(a) Back side, (b) front side, of WB Sample 6, failure characterization, R = 0.15 m.....	95
Figure 80.	Failure of AB Sample 7, test run 4, R = 0.3 m	96
Figure 81.	Failure characterization, AB Sample 7, R = 0.3 m	96
Figure 82.	Overall pressure profile (left), plate failure loading (right), WB Sample 6, R = 0.15 m	97

Figure 83.	Overall pressure profile (left), plate failure loading (right), AB Sample 7, R = 0.3 m	97
Figure 84.	Maximum nodal pressures for WB Sample 6 and AB Sample 7	98
Figure 85.	Strain response, WB Sample 6 (0-90-90-0°), R = 0.15 m, failure run	99
Figure 86.	Strain response, AB Sample 7 (0-90-90-0°), R = 0.3 m, failure run	100
Figure 87.	Normalized WB and AB max x-strain result comparison until failure (0-90-90-0): (left) tension, (right) compression.....	101
Figure 88.	Normalized WB and AB max y-strain result comparison until failure (0-90-90-0): (left) tension, (right) compression.....	101
Figure 89.	Power supply, at 10V VEX setting	107
Figure 90.	Correct banana plug connections from power supply to Wheatstone bridge	108
Figure 91.	Wheatstone bridge input nodes	109
Figure 92.	Continuity check function selected on DMM.....	110
Figure 93.	Internal node location for bridge needing repair.....	112
Figure 94.	Wheatstone bridge internal board, blue wire repair site example.....	113
Figure 95.	Wheatstone bridge, internal view, top board, resistors.....	114
Figure 96.	Valve labels for CASPUR operating procedures.....	115
Figure 97.	NI Suite, power button shown for system start-up	117
Figure 98.	Proper BNC and ICP® sensor connection to signal conditioner for Channel 1	119
Figure 99.	Signal conditioner light indicators	120
Figure 100.	NI Max, Test Panels interface.....	121
Figure 101.	Gasket used for flange to holder sealing for CASPUR.....	122
Figure 102.	Flange block set-up for shock pipe length adjustment.....	124
Figure 103.	Flange block side view for 2-inch NPT threaded fitting tightening procedure.....	125

Figure 104.	Wire routing for AB set-up	127
Figure 105.	Zip-tie placement to prevent strain gage damage	128
Figure 106.	Back composite plate with wire routing and duct seal	129
Figure 107.	DAQmx Acquire NI function	132
Figure 108.	Configuration for strain DAQ in Signal Express	133
Figure 109.	Configuration for pressure DAQ in Signal Express	135
Figure 110.	Save function for Signal Express	136
Figure 111.	Signal save settings, strain, Signal Express	137
Figure 112.	File save settings, strain, Signal Express	138
Figure 113.	Signal logging selection for DAQ in Signal Express.....	140
Figure 114.	Strain response, WB Sample 3 (0-90-0°), R = 0.61 m, Run 1	143
Figure 115.	X-direction, maximum strain trends, AB and WB, 0–90-0: tension (left), compression (right)	144
Figure 116.	Y-direction, maximum strain trends, AB and WB, 0–90-0: tension (left), compression (right)	144
Figure 117.	Strain response, WB Sample 6 (0-90-90-0°), R = 0.61 m, Run 1.....	145
Figure 118.	Strain response, WB Sample 6 (0-90-90-0°), R = 0.46 m, Run 2.....	146
Figure 119.	Strain response, WB Sample 6 (0-90-90-0°), R = 0.3 m, Run 3.....	147
Figure 120.	Raw x-direction, maximum strain trends, AB and WB, 0–90-90-0: tension (left), compression (right).....	147
Figure 121.	Raw y-direction, maximum strain trends, AB and WB, 0–90-90-0: tension (left), compression (right).....	148
Figure 122.	Strain response, AB Sample 7 (0-90-90-0°), R = 0.61 m, Run 1	148
Figure 123.	Strain response, AB Sample 7 (0-90-90-0°), R = 0.46 m, Run 2	149
Figure 124.	Pressure characterization, linear layout, R = 0.46 m, Run 2.....	151
Figure 125.	Pressure characterization, linear layout, R = 0.46 m, Run 3.....	152

Figure 126.	Pressure characterization, linear layout, R = 0.46 m, Run 4.....	153
Figure 127.	Pressure characterization, triangular layout, R = 0.3 m, Run 2	154
Figure 128.	Pressure characterization, triangular layout, R = 0.3 m, Run 3	155
Figure 129.	Pressure characterization, triangular layout, R = 0.3 m, Run 4	156
Figure 130.	Pressure characterization, triangular layout, R = 0.3 m, Run 5	157
Figure 131.	Overall pressure profile (left), plate failure loading (right), WB Sample 3, Run 1, R = 0.61 m.....	157
Figure 132.	Overall pressure profile (left), plate failure loading (right), WB Sample 6, Run 1, R = 0.61 m.....	158
Figure 133.	Overall pressure profile (left), plate failure loading (right), WB Sample 6, Run 2, R = 0.61 m.....	158
Figure 134.	Overall pressure profile (left), plate failure loading (right), WB Sample 6, Run 3, R = 0.46 m.....	159
Figure 135.	Overall pressure profile (left), plate failure loading (right), WB Sample 6, Run 4, R = 0.3 m.....	159
Figure 136.	Overall pressure profile (left), plate failure loading (right), AB Sample 7, Run 1, R = 0.61 m.....	160
Figure 137.	Overall pressure profile (left), plate failure loading (right), AB Sample 7, Run 2.....	160

THIS PAGE INTENTIONALLY LEFT BLANK

LIST OF TABLES

Table 1.	Material properties of carbon fiber plates tested. Adapted from [20].....	20
Table 2.	Fiber orientation & thickness of CFRP plates	20
Table 3.	Maximum pressure results summary as function of R.....	69
Table 4.	Carbon fiber composite plate test matrix results.....	102

THIS PAGE INTENTIONALLY LEFT BLANK

LIST OF ACRONYMS AND ABBREVIATIONS

AB	air-back
AI	analog input
AWG	American Wire Gage
AWT	anechoic water tank
CASPUR	compressed air shock pipe underwater release
CASS	compressed air supply system
CTR	composite test rig
CFRP	carbon fiber reinforced polymer
CGA	Compressed Gas Association
DAQ	data acquisition system
DMM	digital multimeter
F_B	buoyant force
FSI	fluid-structure interaction
GF	gage factor
HP	high pressure
LN2	liquid nitrogen
LP	low pressure
NI	National Instruments
NPS	Naval Postgraduate School
NPT	National Pipe Taper
P_0	near-instantaneous maximum peak pressure
PET	polyethylene terephthalate
PTFE	polytetrafluoroethylene
PPV	PET pressure vessel
R	stand-off distance
RF	raised face flange
R_L	lead resistance
STR	shock test rig
UNDEX	underwater explosion
V	voltage, volts

V_{EX}	excitation voltage
V_o	voltage, out
V_r	voltage, ratio
WB	water-back
θ	decay-constant
Ω	resistance, ohms

ACKNOWLEDGMENTS

Thank you Professor Kwon for being so supportive over the last year especially through the design and implementation of CASPUR. You always made yourself available to talk, even on the weekends, when I realized I made a mistake or forgot something in the design and I greatly appreciated that. You never criticized me, but you were encouraging with any idea or observation I made even if it did not come to fruition. I will miss our Tuesday meetings, but I will say it is a relief to finally be done with my thesis!

Thank you Professor Didoszak for always making time to talk, especially when I was frustrated or stuck on a problem with the research. I appreciated your voice of reason when things were a little chaotic, and for your enthusiasm and support to finally get a new design built and successfully tested. Your approachability was significant for me to know that I could bring anything up that I needed to.

Professor Seivwright, thank you for your willingness to help me at any point with my new design, even though I was not one of your thesis students. The time and input you gave made the completion of the new design possible. Your hands-on expertise and your skill for teaching has made a real positive impression on me. Professor Dausen, thank you as well for jumping in with little heads ups to help me get through several of the design hurdles that I did not know how to get over or around. Thank you for investing your time in me and my research, and for your consistently positive outlook regardless of the current situation. Thank you Professor Luhrs for your guidance on the compression fittings, and for pointing me to so many resources that were pivotal to the new shock loading design coming to completion. Thank you, Professor Ansell, for your assistance with the liquid nitrogen and for your insight on important material considerations for the new design.

Big thanks to John Mobley for all of his support in the machine shop for the large number of cuts and parts made in each iteration of the designs. I appreciate the time you gave to teach me about some of your craft, and your sense of humor was always well timed when I was getting too stressed out about how things were going with my thesis. I would

seriously not have finished my thesis and got done all that I did if it had not been for your help, so thank you very much.

I am extremely grateful to my life group for their support, encouragement, unity of mind and heart, and prayer through my entire time at NPS. You were a family to Molly and me in the midst of being so far from most of our family, and that was huge, especially with the overarching impacts of COVID.

To my lovely, kind, and ever-patient wife Molly, I love you so much, and thank you for loving me so well through all of the hard parts of grad school. You felt the brunt of way too many late nights and long days apart from one another, and I am so glad that is finally behind us. You always brought the best timed and much needed humor to bring perspective to grad school when it felt overwhelming with no end in sight. I am so proud of what you accomplished with the teaching credential program at CSUMB, and the kids in New England have an incredibly caring, smart, gentle, and super prepared teacher coming their way!

I. INTRODUCTION

A. BACKGROUND AND LITERATURE REVIEW

The use of composite materials in marine and naval applications has a relatively recent history, traced to World War II [1]. In naval applications, composite structures provide several advantages not found in traditional shipbuilding materials. Several of these benefits include high strength to weight ratio, potential fuel savings in ship design due to a lower overall total displacement, and excellent non-susceptibility to corrosion [1]. Additionally, a unique benefit that composite materials provide for naval applications is its relatively low reflectivity in the electro-magnetic spectrum compared to metals, thereby reducing detectability and increasing stealth [1]. Several disadvantages inherent to composite materials are minimal resistance to damage from impact energy, sudden failure due to its brittleness, and a propensity to degrade over time in extended exposures to a marine environment [2-3]. Furthermore, the shorter history of composite use compared to use of metal or wood means large gaps still exist in experimental data coupled with accurate modeling [3].

1. Loading Mechanisms

In naval ship applications unique requirements exist to ensure the vessel will not only survive but retain some of its performance under extreme loading conditions. One of the most complex and intense loading conditions for naval vessels is the event of an underwater explosion (UNDEX). An excellent primer by Costanzo, explaining the basics of each phase of UNDEX, summarizes overarching principles [4]. For brevity here, important shock wave characteristics, cavitation, bubble dynamics, and reflection will be outlined as they occur in time. Detonation of an explosive generates a supersonic shock wave radially from the charge center while also forming a spherical gas bubble produced from the chemical reactants. Properties of the shock wave can be considered to behave more acoustically linear outside of 2–3 charge radii [4]. This delineation is described as the demarcation between near-field and far-field UNDEX. Near field proves more complex to analyze and model because of its highly non-linear behavior [4]. Far-field pressure $P(t)$

produced by the shock wave is characterized as an exponentially decaying curve such as [5]:

$$P(t) = p_0 e^{-t/\theta} \quad (1)$$

where peak pressure, p_0 , is defined as the nearly instantaneous pressure spike on the order of micro-seconds, and θ is the decay time, describing how long it takes for the pressure to decrease to 37% of p_0 [6]. For widely used conventional explosives, the maximum peak pressure and the decay constant were experimentally derived using the charge mass, W (kg), and stand-off distance, R (m). Stand-off distance is measured radially from the charge center to the far-field point of interest in meters [4–6]. Although an enormous difference in scaling existed from the experimental results of TNT to the methods used in this research, these general principles of stand-off distance, charge mass, and decay constant were utilized in this research.

Cavitation occurs in two primary forms: bulk cavitation at the water's surface, and local cavitation at the fluid-structure interface [4,7]. Cavitation is present where a reflective wave creates high localized tensile stresses in the fluid resulting in a low-pressure area of gas and water droplets [2,4,7]. Bulk cavitation can produce a secondary pulse back into the fluid medium, but of greater concern is the momentary interruption of contact between the fluid and the structure of interest. This localized occurrence can lead to a damaging reloading of the structure as the hydrostatic pressure rapidly closes this vaporous void [7].

At a subsonic rate, the gas bubble continues to expand outwards until its pressure front and maximum radius is arrested and reversed by the surrounding hydrostatic pressure. If sufficient energy is initially present at detonation, successive expansion and contraction of this bubble will occur until the entire energy of the bubble is released due to its surface travel or fully dissipated into the surrounding water. This phenomenon is shown clearly in Figure 1 where the dome and successive sprays exceed the surface tension of the water [4]. Depending on the proximity of the initial bubble collapse to a submerged structure, these pressure pulses can result in severe damage [2,4].

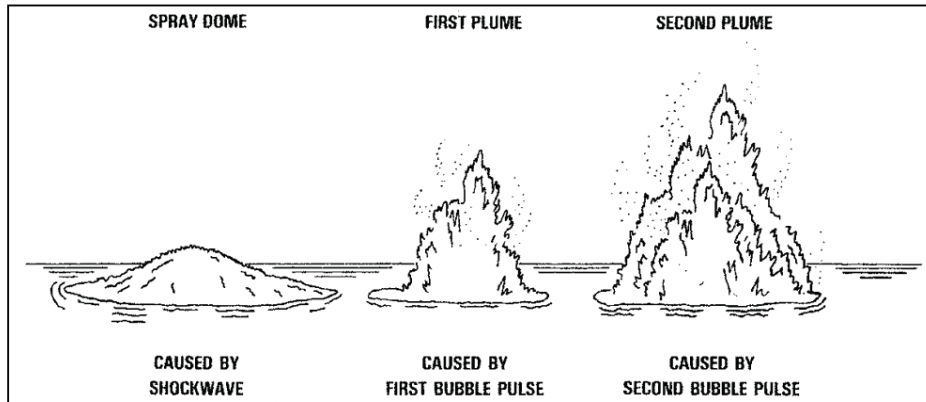


Figure 1. Surface phenomena for 250-lb HBX-1 at 50-ft depth. Source: [4].

2. Fluid-Structure Interface

As a result of the loading mechanisms discussed, the dynamics between the fluid medium and the structure itself are extremely complex to analyze and accurately predict. In both air and water environments the coupling that occurs between the fluid and structure itself is called fluid-structure interaction (FSI) [8]. In terms of acoustic impedance, composites generally share similar impedance values with water allowing for a more pronounced added mass effect to a submerged structure when encountering impulsive loading thereby increasing the effects of drag [8-9]. Acoustically speaking, impedance is a function of the density of the medium the sound wave is propagating through as well the speed of sound through that medium [9]. Similar impedance values promote continued propagation of the sound wave, whereas impedance mismatch leads to significant wave reflection [9]. By describing the fluid medium that is on the near and far side of a structure, we are defining the backing condition of the structure. Two contrasting backing conditions were examined in this research related to impedance: Air Back (AB) Water Back (WB). An example of each of these backing conditions can be found in naval ship design. An AB example would be a crew member space or void near the ship hull where air is on the far side of the structure and seawater is on the near side of the structure. A fuel tank or ballast tank also near the ship hull would be an example of a WB condition where water and or some type of liquid exists on both sides of the structure. It is the impedance mismatch between the structure and fluid interface that can cause complex response and failure

phenomena in the structure. If the density of the structure and incoming shock wave medium are similar, the energy will continue to translate through the structure itself if water is on the other side. In the case where air is on the far side away from the incoming shock front, the impedance mismatch can result in a much larger reflection of energy back in the direction of the initial shock front [10]. Both backing conditions produce markedly different effects on capacity of the composite structure to dissipate impulse energy, total deflection of the structure as well as strain rate [10-14].

3. Past and Present Experimental Efforts

Full-scale shock trials by UNDEX are reserved for combatant vessels to demonstrate a naval vessel's capability to retain its structural integrity and combat readiness under these extreme loading conditions. Full-scale testing removes the need for scaling, provides valuable data on not just the hull response, but also on the resilience of the engineering and combat systems onboard. Additionally, boundary conditions no-longer play as significant of a roll in material response and failure. Frequently in a laboratory environment is difficult to force a large-scale behavior in a small-scale specimen. This is commonly seen in stress concentrations along clamped or bolted boundaries when evaluation of the transient response of a material is more desirable in the center of a specimen as in a simply supported case [2-3]. A recent review in 2019 on fiber reinforced composites by Mouritz gives thoughtful perspective on the strengths and weaknesses of lab-scale testing compared to that of large-scale [2]. Several drawbacks of a large-scale UNDEX are the significant financial expense of the event, the negative environmental impact on marine life, and the time required for the planning and instrumentation installation for the test event [2,9]. Conversely, laboratory testing provides potential for excellent repeatability under controlled conditions, lower cost per test, and the capacity to make rapid design changes in concert with theoretical and numerical modeling and simulation advances.

Tran et al. helpfully summarizes the common past and present testing methods to replicate the underwater shock loading on composite materials due to UNDEX [1]. Mouritz, Sanders, and Buckley designed a large steel cylinder lined with plastic to

minimize wave reflection and provided capability for both AB and WB backing test conditions [10]. This set-up utilized live explosives producing peak pressures 15% higher than TNT [10]. LeBlanc and Shukla were one of the first to implement a water-filled shock tube [1]. Their system currently only allows for AB configurations and utilizes live explosives to generate a planar shock wave down the shock tube [1]. A different shock tube variation, which supports AB and WB test conditions, utilizes a gas gun design to rapidly drive a projectile against a flyer plate [15]. By changing the projectile velocity with this configuration, loading pressures could be obtained as high as 300 MPa [15]. A large strength in all these designs allows for live failure characterization in the composite specimens, as well as deflection measurements through a type of high-speed digital image correlation [1]. Additionally, they provide the capacity for testing of curved surfaces which is understood to have more complex transient response than that of a flat plate [2]. Schiffer and Tagarielli further improved the shock tube concept by constructing one that is fully transparent, allowing for observation and characterization of behavior of localized cavitation [14,16-17]. Most recently, LiVolsi designed and implemented a similar cubic tank utilized in this research to examine the effects of environmental parameters on AB and WB flat plates utilizing a small mass explosive charge [13].

4. Failure Characterization

Characterization of the different failure modes in composites can be described by matrix cracking, delamination, and fiber fracture [2-3]. Matrix cracking occurs where the layers between both individual laminates as well as between the fibers themselves exhibits cracking. Delamination occurs when the adhered bond between the fibers and the binding matrix is broken [18]. Fiber fracture is simply where the fiber itself has broken, which can be seen in both contact and non-contact impulsive loading.

B. OBJECTIVES

To the best knowledge of the author the literature review revealed a lack of breadth and depth in experimental efforts to test specimens in both backing conditions AB and WB. It is more common for an investigation to be made of varying coating type or thickness or evaluating the performance and behavior of different materials within a series of tests. When

both backing conditions are evaluated it is often done in a separate manner vice a comparative one. This could be a result of the difficulty to design a testing apparatus with the capacity to have two very different backing conditions. Most testing apparatus in use are currently designed to test in just one backing condition. Additionally, certain apparatus is more conducive for high-speed image capture, and the backing condition can limit the imagery that can be collected. Since naval vessels commonly have structures that contain both backing conditions, as seen in a ship hull or conversely ship tanks, it is important to better understand how composite materials would behave under these backing conditions.

This implication led to the first objective of this thesis work: to use an existing experimental shock loading method to provide further insight in how composites respond and fail under dynamic loading due to underwater shock loading. Additionally, an objective was to examine how the backing condition of a structure influences composite response and failure underwater. Specifically, this will be accomplished by fabricating and implementing a composite test rig (CTR) that is capable of testing flat composite plates, fully submerged, with contrasting backing conditions and identical clamped boundary conditions on the front and back of the box. Prior to composite plate testing, characterization of pressure profiles, using liquid nitrogen as the charge source, will be completed. Then plates with similar fiber orientations and thicknesses will be evaluated under similar loading conditions and at the same progression of stand-off distances until failure. Pressure data will be collected as well as strain data for correlation of loading to deformation as well as correlation of failure characterization under contrasting backing conditions. Investigation of the strain response, and correlation of local vs. global failure due to backing condition will be examined across different cross-ply laminate orientations. Experimental results will then be used to strengthen numerical models and validate or challenge existing theory.

The second objective was to design, assemble, and test a new and unique underwater shock loading apparatus at the Naval Postgraduate School (NPS). A primary design goal for this new system was to provide repeatable results in loading and composite structure response. Additionally, this new design will provide future opportunity to test stronger materials at higher and more rapid loading rates closer to those produced by the institutions referenced in the earlier section of this chapter. Ultimately, the second objective was to be accomplished

through the design and implementation of the Compressed Air Shock Pipe Underwater Release (CASPUR) system, outfitted with an industrial grade non-fragmenting stainless-steel rupture disk. Rapid failure of the rupture disk is the trigger mechanism for shock propagation towards the composite structure of interest. Successful execution of the CASPUR system will provide excellent control of position, directionality, and magnitude of the underwater shock loading which was more difficult to achieve with the current liquid nitrogen loading method.

THIS PAGE INTENTIONALLY LEFT BLANK

II. METHODOLOGY

A. ANECHOIC WATER TANK

Laboratory testing was conducted in a square 28.32 m³ (1000 ft³) anechoic water tank (AWT). Drawings provided by NAVFAC, shown in Figures 2 and 3, indicate the foundation of the AWT has a layered design identical on all five sides. These layers are comprised of redwood panels, cement plaster, gunite, sand, and concrete, all designed to withstand and dampen the effects of UNDEX in a laboratory environment. The 45° redwood panels installed on all faces of the AWT are designed to reduce reflection of the shock waves to the greatest extent possible. This helps to ensure the pressure measured by the pressure transducers is primarily from that initial steep shock front and not from reflected sources. For our research, we wanted to ensure reflective wave energy has minimal effect on the primary loading measured by the sensors to simplify our analysis. The CTR and loading source were positioned at the center of the tank to ensure reflective energy did not disturb the data acquisition process. This was assured by the longer time it took for a non-direct wave to travel from the source to the wall of the AWT or the surface and then to target, than the time the incident shock front took to reach the target from the source.

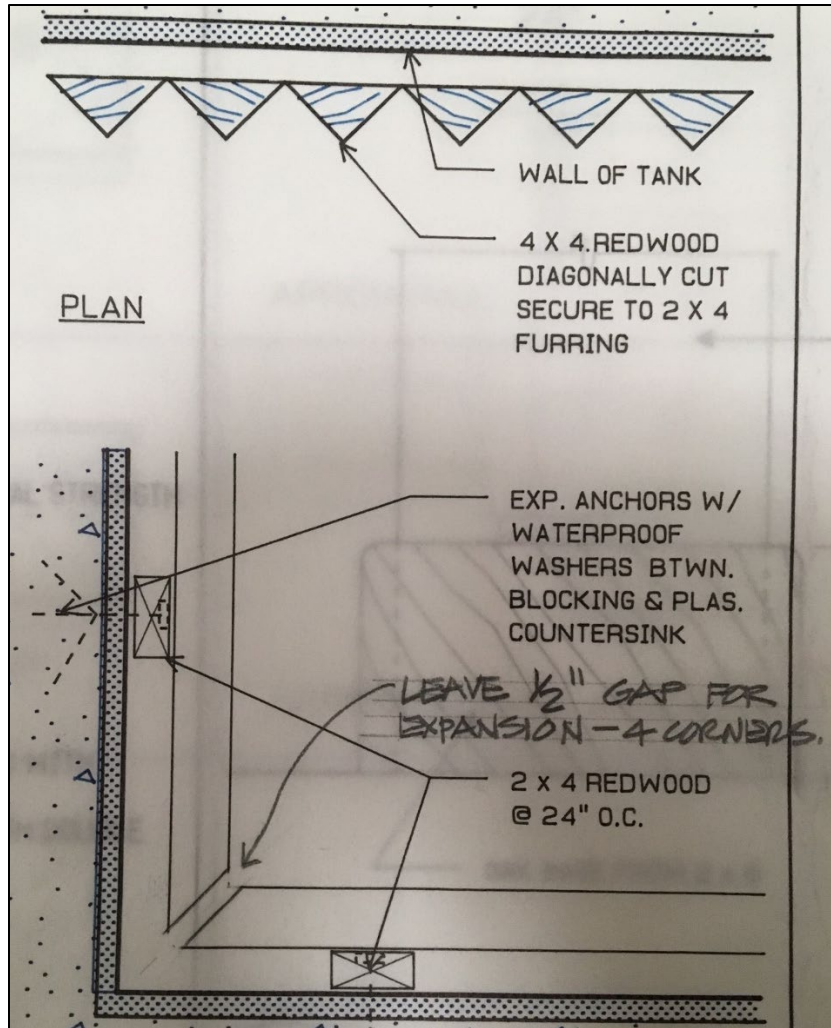


Figure 2. AWT, top view, showing anti-reflective redwood panels

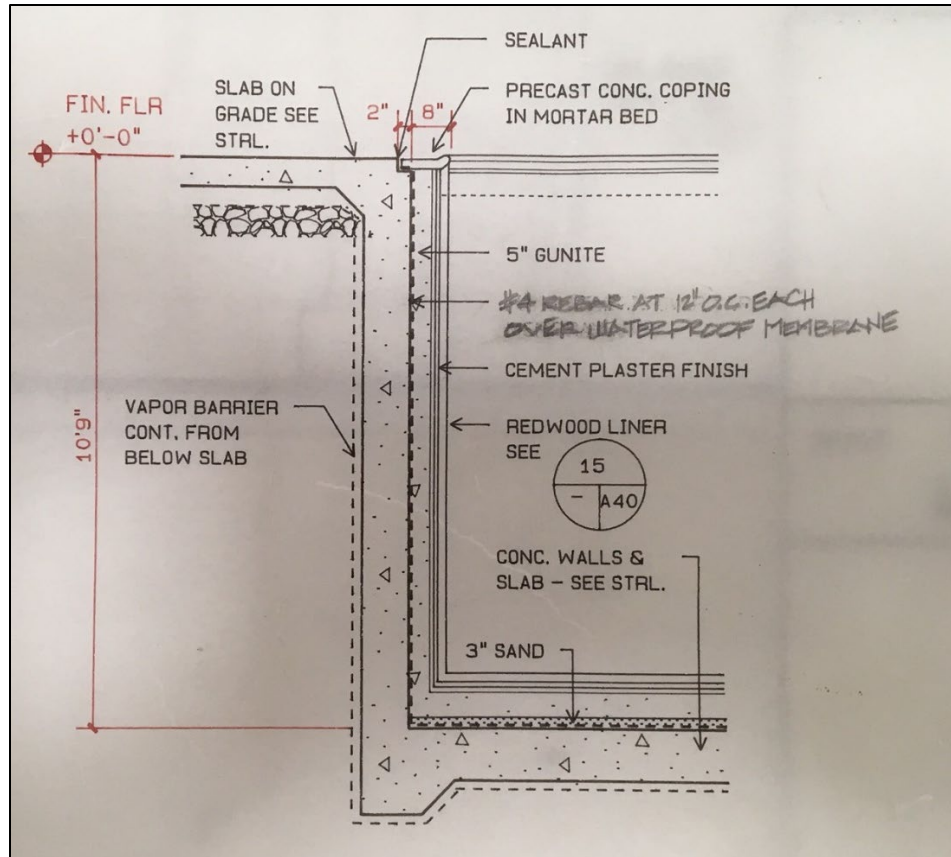


Figure 3. AWT, side view, showing layered design for damping

The AWT was filled with tap water. The water level was monitored and maintained to ensure the center of the composite plate remained at the half-depth of the water level. Waterproof portable illumination was used in the tank between test events to check integrity of the test plates prior to proceeding to a closer stand-off distance. The top of the AWT was spanned with six aluminum I-beams which were covered with plywood sheets 1.27 cm thick (0.5in).

B. COMPOSITE TEST RIG

Aluminum slotted framing, plates, brackets, gussets, screws, nuts, and clamps were used to build the composite test rig (CTR). Two main sections comprised the CTR: the box and the rails. Heavier material utilization was intentional for the overall CTR design to reduce the energy absorption of the rig and maximize the energy transfer from the shock front into the composite test plates. Keeping the rig as stationary as possible during testing

while retaining mobility to support different stand-off distance test runs was integral for the CTR to be an effective design.

1. Box Design

The primary function of the box was to rigidly hold the composite plates in a clamped boundary condition, and facilitated AB and WB backing conditions. Overall box design can be seen in Figure 4, with dimensions of 0.47 m tall, 0.47 m wide, and 0.39m deep (18.5in by 18.5 by 15.5in), with a mass of 34.47 kg (76 lbs).

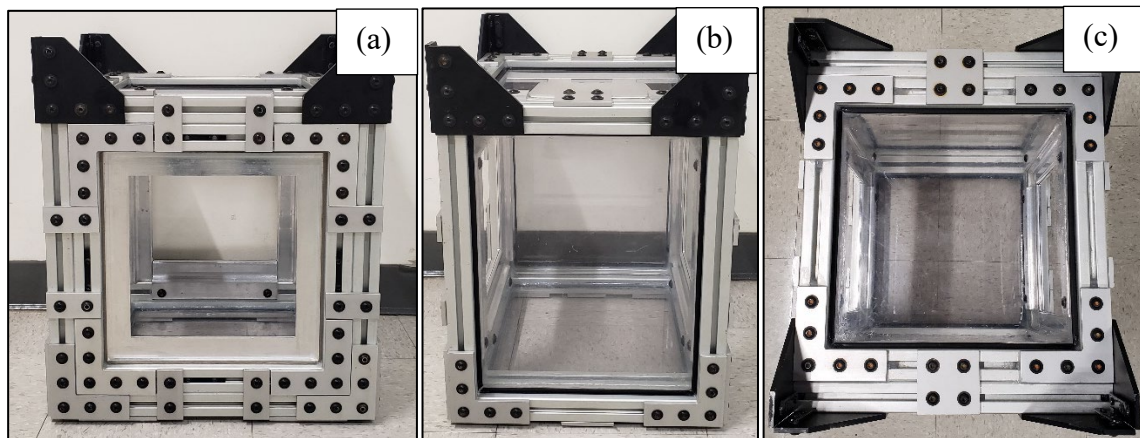


Figure 4. Overall box design: (a) front view, (b) side view, (c) top view

Plexiglass panels 5.76 mm thick (0.23 in) thick were installed on all faces of the box except for the front and back. This provided the ability to confirm the AB backing condition exists (i.e., no water leaking into the box) as well as opportunity for future live imagery capture. Gaps between the plexiglass panels and the internal slot of the framing were filled with a gasket around the perimeter of the panel to ensure water tightness of the box. Seams of the box that were metal to metal contact provided the greatest path for water intrusion. Internal slots were initially filled with backer rod as shown in Figure 5. Then silicone caulk was applied over the backer rod as an additional measure to prevent water intrusion into the box shown in Figure 6. Silicone caulk was used to seal every internal and external seam to ensure water tightness for AB testing.

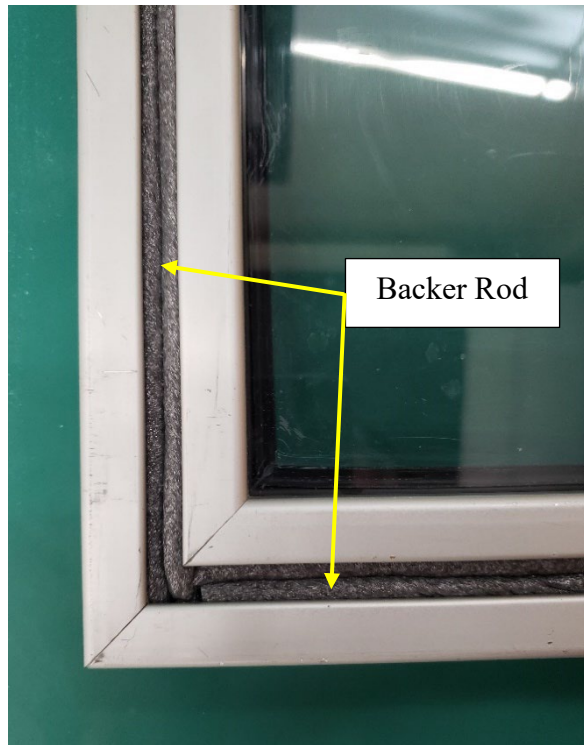


Figure 5. Backer rod installation to fill internal frame groove to prevent water intrusion



Figure 6. Waterproof sealant used to ensure AB backing condition

Square Carbon Fiber Reinforce Polymer (CFRP) plates were fixed to the box by layering it between the front and back windows as seen in Figure 7. The back window remained permanently installed, cut to fit in the internal t-slot frame of the box to provide watertight integrity for AB testing. A step was machined into the back window with a depth of 4.3 mm which can be observed in Figure 8. Depth of the step was chosen to make the stacked height of the test plates and the top window to exceed the height of the back window. This ensured the s-shaped retainer clamps attached to the front window provided a secure and even clamped boundary condition around the perimeter of the CFRP plate. Step perimeter was designed with a 1 mm gap between the step sides and the test plate to accommodate for variations in plate size. Pre-stress or damage to the test plate prior to testing was prevented by this built-in tolerance. Additionally, the step was designed to prevent movement of the plate in the x and y-directions shown in Figure 9. Movement of the test plate in the z-direction was restricted by the front window shown in Figure 10. Outer dimensions of the front window were machined to fit tightly inside the outer perimeter of the back-window step.

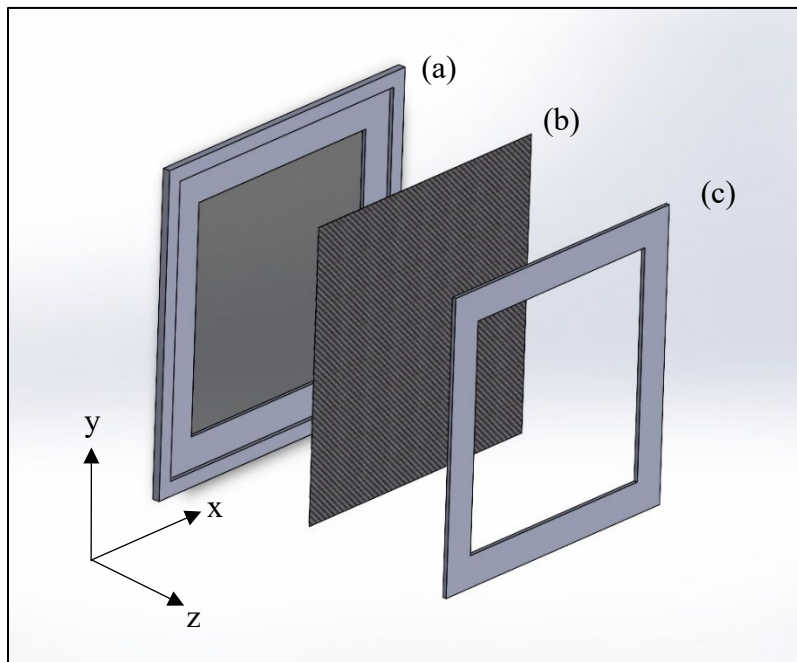


Figure 7. Layering sequence composite plate installation to box: (a) back window, (b) composite plate, (c) front window

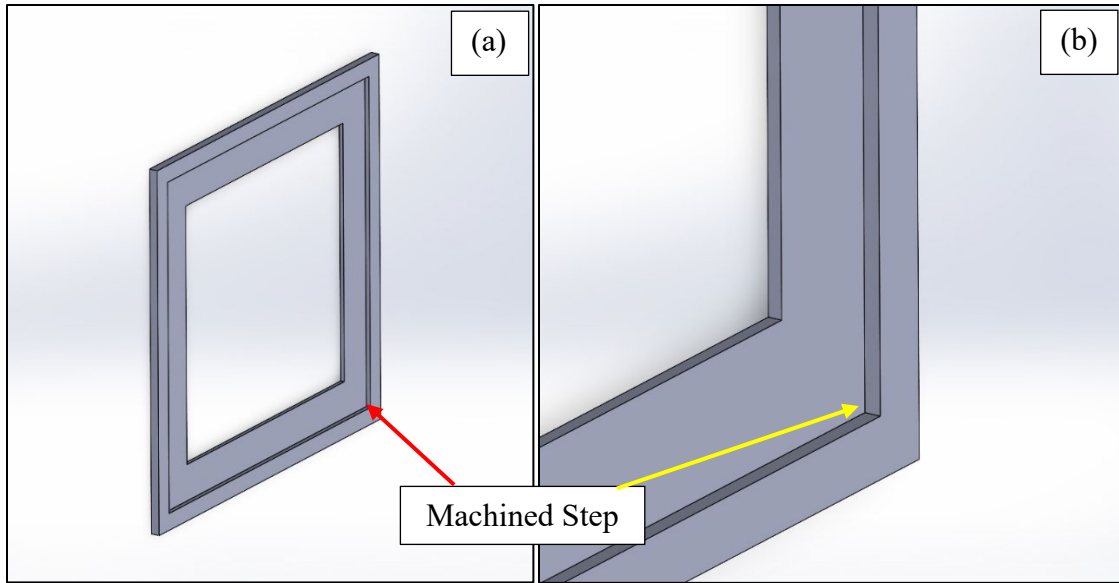


Figure 8. Window design for (a) back window and (b) zoomed view of step

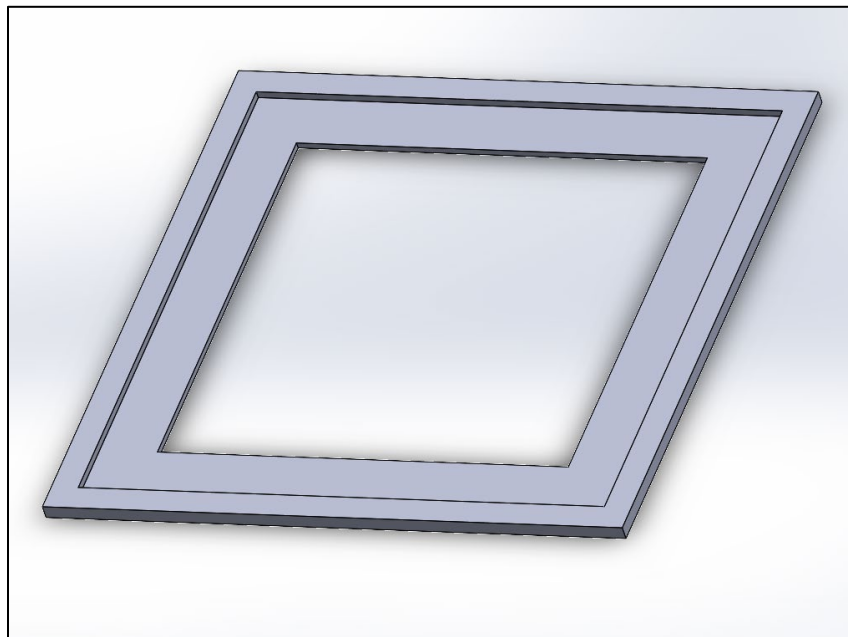


Figure 9. Back window design, restricts movement of plate in x-y directions

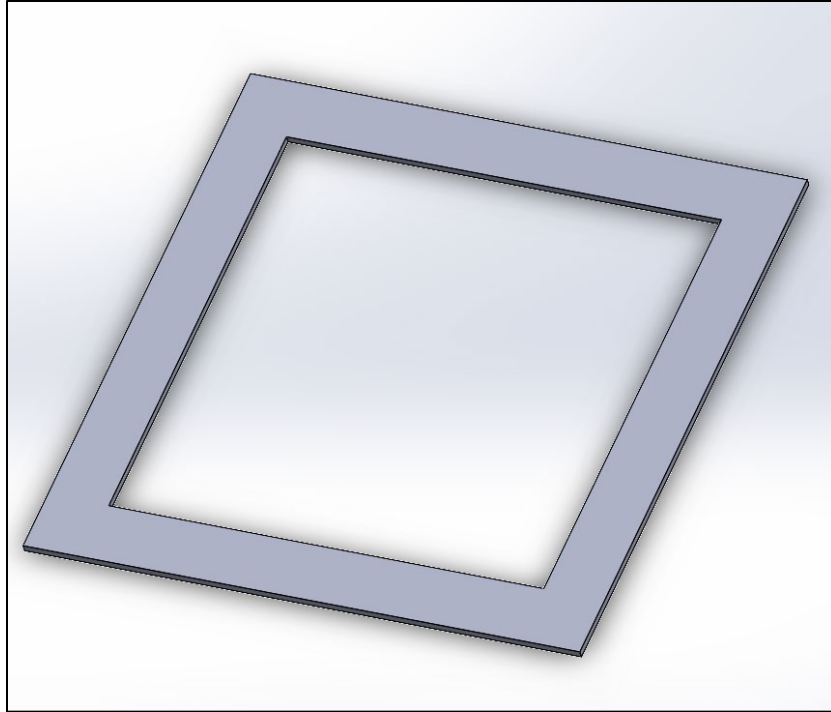


Figure 10. Front window design, restricts movement of plate in z-direction

S-shaped retainer clips were used on all four sides of the front window to provide a secure clamped boundary condition on all four sides as shown in Figure 11. All through window dimensions were cut to be 0.24 m by 0.24 m (9.5 in by 9.5 in), so no overlap existed between the backing clamps, the back window, and the front window.

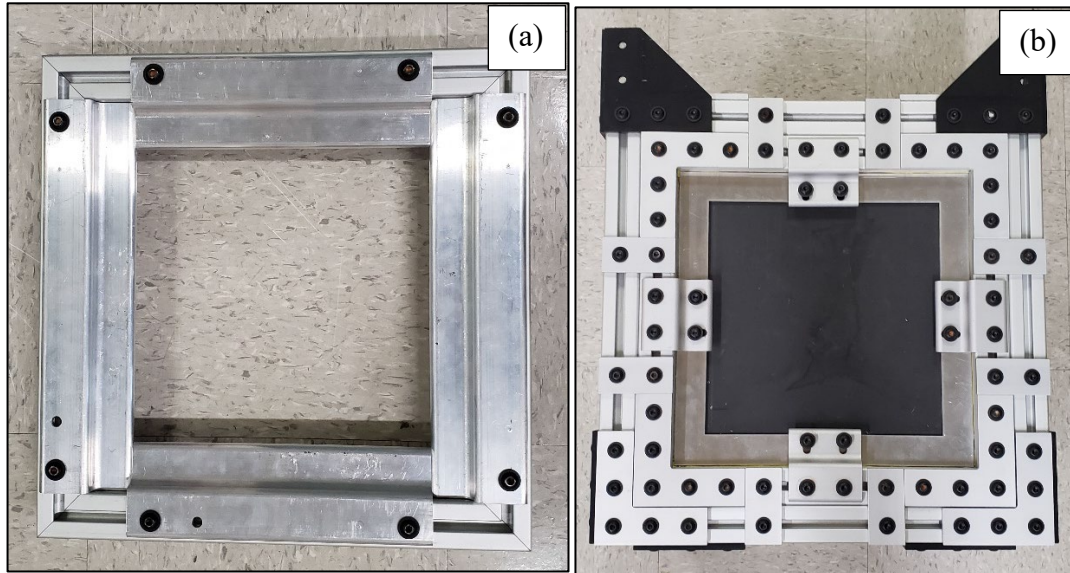


Figure 11. (a) Backing clamps (b) retainer-clips for clamped boundary condition

2. Rail Design

The primary function of the rail design was to facilitate vertical and longitudinal placement of the box. Vertical rail length is fixed at 1.75 m (69 in), while cross rails spanned the I-beams at 0.94 m (37 in). Mass of the rails was determined to be 29.03 kg (64 lbs). Vertical rails assisted as guides during the more complex experimental set-up for AB testing. When the box was fully submerged, the center of the composite plate rested at the half-depth of the water in the AWT. Water level was monitored and maintained to ensure the composite test plate remained at the half-depth of the AWT. Rail design required modification to support AB testing due to increase in buoyancy force, F_B . A holding tray was added to the top of the rig so additional mass could be added above the waterline to overcome the net F_B of the CTR during AB testing. Original and modified CTR designs are provide in Figures 12 and 13.

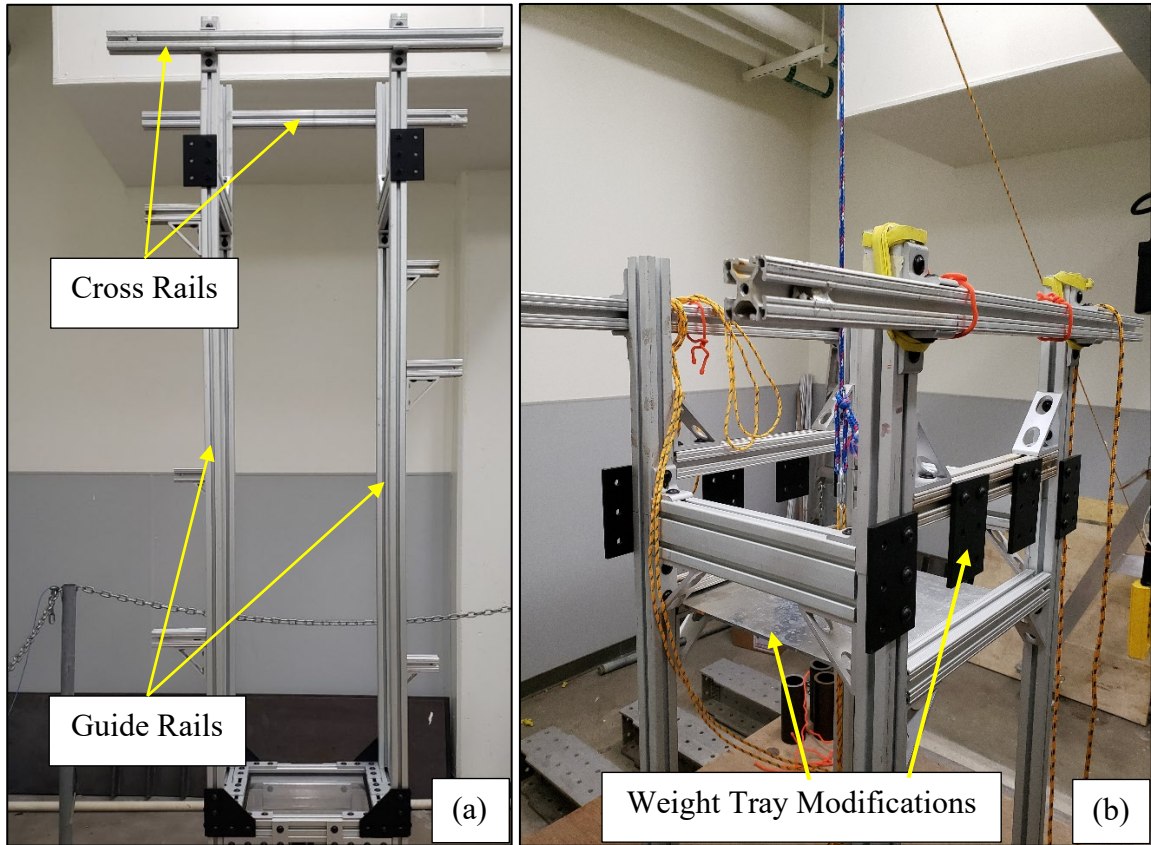


Figure 12. CTR rail design: (a) initial and (b) modified

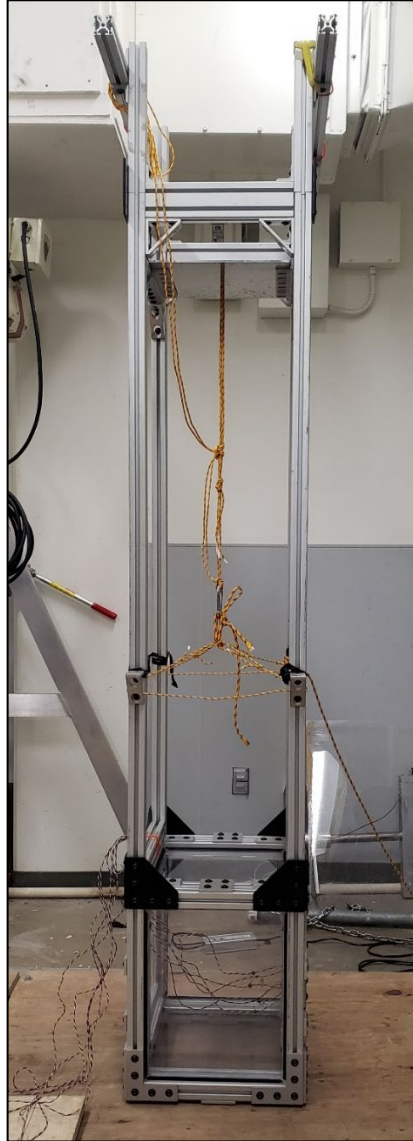


Figure 13. Overall modified rig design

C. COMPOSITE PLATES

A composite material is generally defined as a man-made heterogeneous material that consists primarily of a matrix and dispersed phase, where in this research, the dispersed phase was comprised of carbon fibers, and the matrix consisted of a polymer resin (CFRP) [19]. Carbon fiber has both excellent performance properties in high temperature and high specific strength which is defined by strength divided by specific gravity [19]. The resin acts as a binder to fibers and protects from direct damage to impact, rubbing, or scraping

[19]. Laminates are a subset structural composite material which often exploits the directionally dependent strength of the fibers by layering them in different orientations to limit a dominating weak direction for the material [19].

Eight flat square CFRP plates, nominally 0.30 m by 0.30 m (12in by 12in), were used for testing in this research. Material properties of the Carbon fiber composite plates used for this research are summarized in Table 1 [20]. A summary of the sample dimensions and fiber layering orientations for each plate that was tested is provided in Table 2.

Table 1. Material properties of carbon fiber plates tested. Adapted from [20].

Experimental Plate Material Properties			
Property	QTY	Units	Description
E_L	111.5×10^9	GPa	Longitudinal Elastic Modulus
E_T	7.61×10^9	GPa	Transverse Elastic Modulus
ν_{LT}	0.2	NA	In-Plane Poisson's Ratio
G_{LT}	2.89×10^9	GPa	In-Plane Shear Modulus
G_{TT}	2.88×10^9	GPa	Out-of-plane Shear Modulus

Table 2. Fiber orientation & thickness of CFRP plates

Sample ID	Orientation (°)	Thickness (mm)	Gage Factor
1	0	0.52	1.2
2	0	0.55	1.2
3	0-90-0	0.38	1.3
4	0-90-0	0.38	1.2
5	0-90-90-0	0.53	1.3
6	0-90-90-0	0.53	1.3
7	0-90-90-0	0.55	1.3
8	0-90-90-0	0.55	1.3

Fiber-Matrix layout for each sample type is provided in the Figure 14. Bending strength of the CFRP plates was identified as the weakest about the x-axis. The greatest resistance to strain was about the y-axis. Therefore, failure was expected to occur parallel to the fiber direction for the near and far fiber layers along the x-axis. This means higher strain values were anticipated in the y-direction and lower strain values in the x-direction.

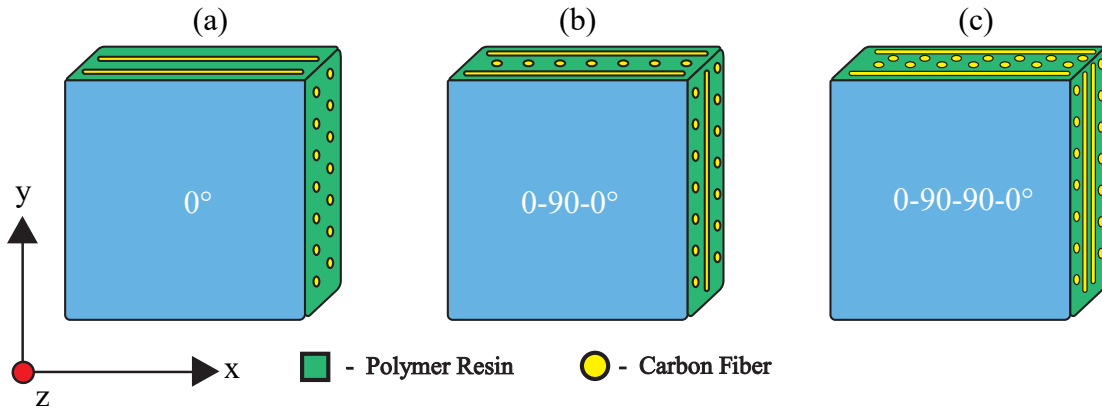


Figure 14. Cross ply fiber orientations: (a) 0°, (b) 0–90–0°, (c) 0–90–90–0°

D. SENSORS AND DATA ACQUISITION

1. Strain Measurement

Three-directional strain gage rosettes were used, having 0–45–90° orientations available for data collection. Because of the limitation of the data acquisition system (DAQ), only the 0° and 90° directions could be evaluated for each sample tested. Strain gage rosettes used for the composite plates were 20 mm long and 16 mm wide. Three strain gages were attached at the vertical centroid of each plate and spaced evenly apart at 5.08 cm (2 in). Strain gages were attached in the same manner as described by Crow using a multi-step sample preparation process [21]. All strain gages had identical resistance values of 350 ohms (Ω). Gage factor(s) (GF) for all plates was 1.3 except for Samples 1, 2, and 4 which had a GF of 1.2. GF refers to the sensitivity of the strain gage to small changes of resistance in the gage when deformed, and is defined by the following equation [22]:

$$GF = \frac{\Delta R/R}{\Delta L/L} \quad (2)$$

GF values for each CFRP provided in Table 1 were entered in the DAQ prior to testing. For each composite plate, all strain gages had the same GF. Six wires measuring 2.9464 m (116 in) were soldered to identical strain gages for data collection, show in Figure 15.

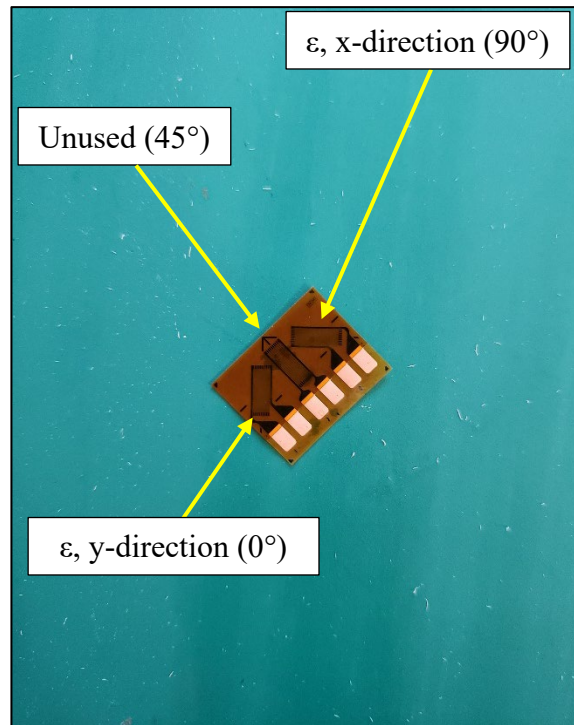


Figure 15. Three-directional strain gage rosette

Dow Corning[®] 3140 MIL-A-46146 RTV coating was applied over the strain gages and their respective wired connections to protect from any water contact. Strain wire leads were fed through the back of the box over the cross-rails to AWT deck level to prevent water contact with the wire leads pictured in Figure 16. Sitting on top of the box at the back was an additional aluminum cross-rail to secure the wire leads, preventing pre-strain on the gages as well as catastrophic damage to them while positioning the CTR. To prevent strain gage wire to wire contact, a foam barrier was used on the top of the wood deck outside of the AWT as shown in Figure 17.

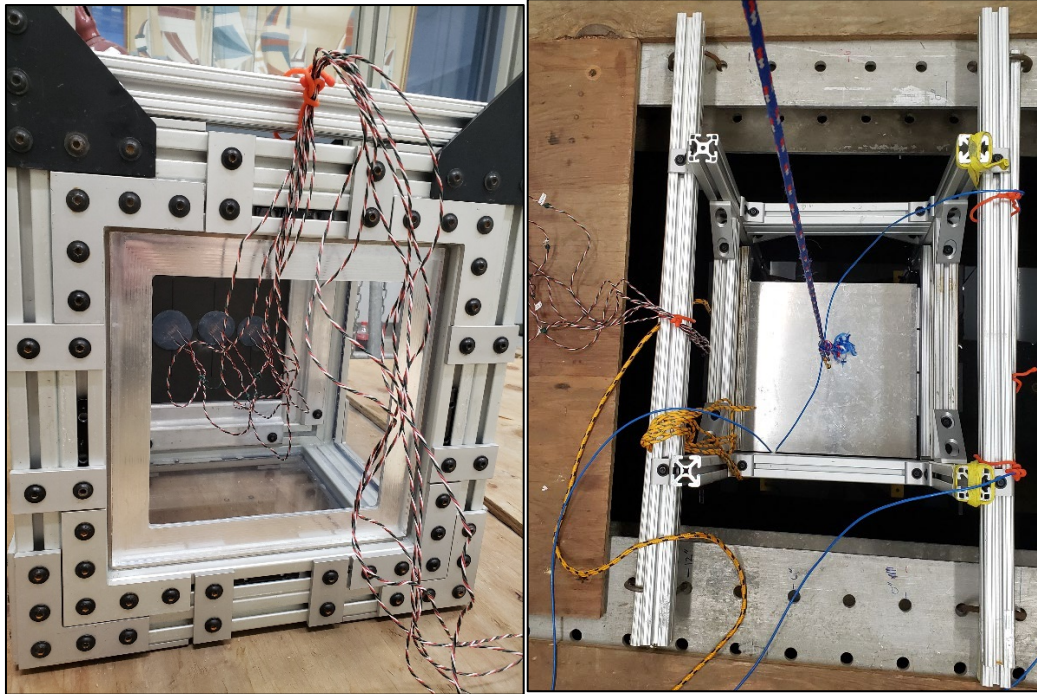


Figure 16. Wire routing from strain gages

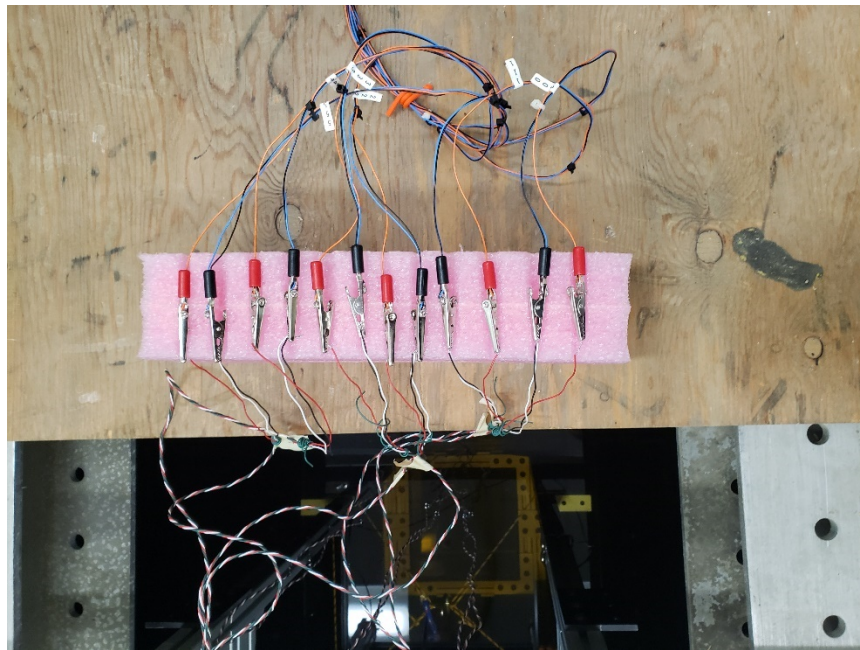


Figure 17. Strain gage wire lead divider to preventing shorting during testing

Strain wire leads were connected to the Wheatstone bridge wire leads with the alligator clips shown in Figure 17. Wire length from the alligator clips to the bridge was measured to be 5.59 m per strand (220 in). This experimental set-up used a Wheatstone quarter bridge I circuit shown in Figure 18.



Figure 18. Wheatstone bridge with potentiometers

Wheatstone bridge theory provides a direct relationship between the micro changes in resistance across a strain gage to a small voltage change across two opposing nodes

(Nodes 1 & 2 in Figure 19) in the circuit of the bridge. The governing equation for strain when using this bridge configuration is given by the following equation [23]:

$$strain (\varepsilon) = \left(\frac{-4V_r}{GF[1+2 \times V_r]} \right) \times \left(1 + \frac{R_L}{R_G} \right) \quad (3)$$

where R_L is the resistance of the lead wires which is the total length of the wires from the strain gages on the composite plate to the Wheatstone bridge.

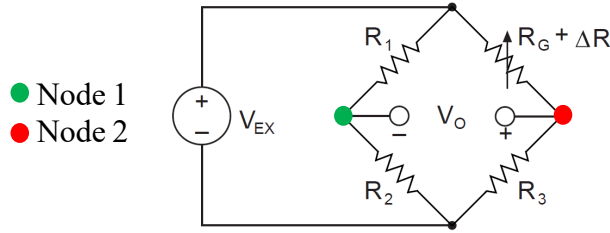


Figure 19. Quarter bridge I circuit layout. Adapted from [22].

Lead resistance describes the resistance incurred due to the length of the wires themselves from the strain gages to Wheatstone bridge. Actual values for lead resistance remain generally standardized across manufacturers. R_L values are based off the core type, i.e., stranded or solid (stranded was used in this set-up), number of strands (7 were counted), and diameter of wire itself excluding the insulating thickness (0.404 mm was measured with a digital micrometer). All wires from the strain gages to the bridge were 26 American Wire Gage (AWG). Using these values for stranded 26 AWG wire the lead resistance was determined to be $130\Omega/1000m$, resulting in a R_L of 1.0918Ω for this lab configuration [24]. R_G is the known resistance of the strain gages provided by the manufacturer. Values for R_G across all strain gages used was 350Ω . An additional known value provided by the strain gage manufacturer was GF . For this research, the GF s used is listed in Table 1. V_r is defined as the Voltage Ratio, which is further defined as [23]:

$$V_r = \frac{V_{o(strained)} - V_{o(unstrained)}}{V_{EX}} \quad (4)$$

Excitation voltage, V_{EX} (sometimes spelled VEX), is the voltage being supplied externally from a power source to the Wheatstone bridge. A 12V capable, 6214C HP power source was used for this research shown in Figure 20.



Figure 20. Power supply for Wheatstone quarter bridge I, power turned off

V_{EX} values for this research remained constant at 10V, optimized using guidelines outlined by National Instruments® (NI) for optimal strain data collection [25]. Voltage out, V_o , refers to a measured voltage on the quarter bridge I circuit and is further described in the following paragraphs [23]. Typical circuit configuration of a quarter bridge I is provided in Figure 19, where one of the four resistors, R_4 , in the circuit is replaced by the strain gage on the composite plate [23].

A quarter bridge II configuration would refer to a dummy strain gage being used in the circuit, which is not a configuration utilized in this research but is supported by the DAQ suite. The black knobs indicated with the red arrows on Figure 18 act as manually adjustable potentiometers to balance the bridge. Each potentiometer is connected to one full quarter bridge circuit, where eight quarter bridge configurations reside internally to the Wheatstone bridge box in Figure 18. A balanced bridge requires the resistance across Node 1 and Node 2 in Figure 19 to be equal which then results in a 0V reading across the nodes referred to as V_o . For accurate strain data to be collected by the DAQ, the overall strain system must start at this 0V point where the bridge is balanced.

If a potentiometer were not available, data would be collected in the unstrained state of the CFRP plate and those $V_{o(\text{unstrained})}$ values would be subtracted from $V_{o(\text{strained})}$ values collected during the UNDEX event. Consequently, for the purpose of this research the use of potentiometers used in this lab set-up, makes the reasonable assumption for $V_{o(\text{unstrained})}$ to be zero, provided the bridge properly balanced. Since V_o unstrained is assumed to be zero, V_r is then directly related to $V_{o(\text{strained})}$ divided by V_{EX} . A SCB-68A from NI, pictured in Figure 21, acts as a digital multi-meter (DMM) to measure and record analog input (AI) V_o , across Node 1 and Node 2.



Figure 21. DAQ: SCB68-A NI DMM

The V_o values are fed internally from the SCB-68A to the NI Xie-1071 chassis via the NI PXIe-6358 shown in Figure 22. Sampling collection capacity for the PXIe-6358 is rated at 1.25×10^6 samples/second/channel. Both strain data and pressure data are received and processed through the PXIe-6358. Total samples and sampling rate were set to 200k samples and 20 kHz respectively. This was to ensure the transient nature of the dynamic shock loading and plate deformation was fully captured.

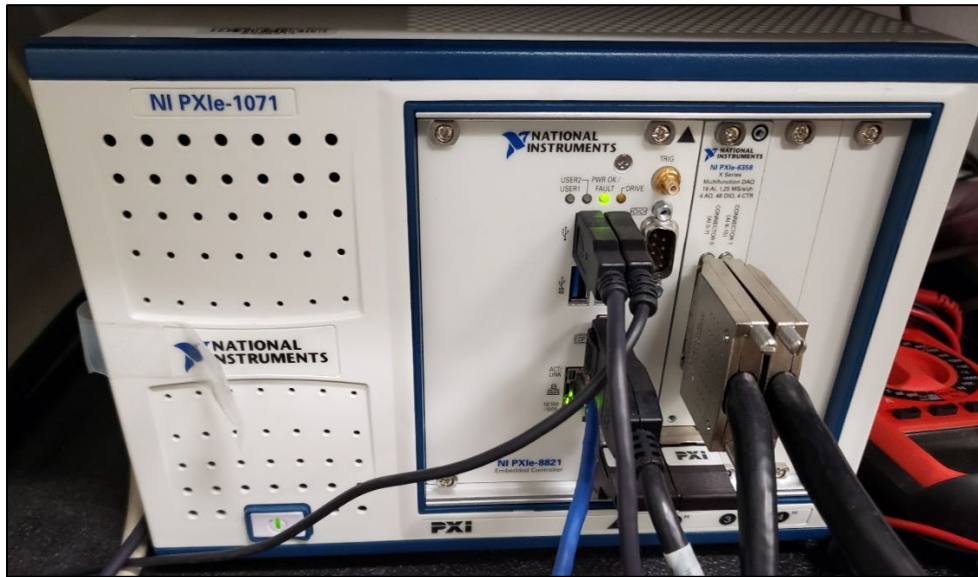


Figure 22. DAQ: signal processing, NI PXIe-6358

Strain is ultimately calculated internally by the DAQ using Equations (3) and (4). Voltage changes due to resistance across the bridge exhibits a non-linear relationship, making it impossible to correct strain data collected from an unbalanced bridge. Consequently, it was imperative the input values for Equations (3) and (4) previously discussed are properly determined and inputted into the DAQ prior to collecting any live strain results.

2. Pressure Measurement

To measure the dynamic pressure of the shock front, three underwater blast sensors were utilized from PCB Piezotronics®. Model 138A10 was used for all dynamic pressure measurements shown in Figure 23.

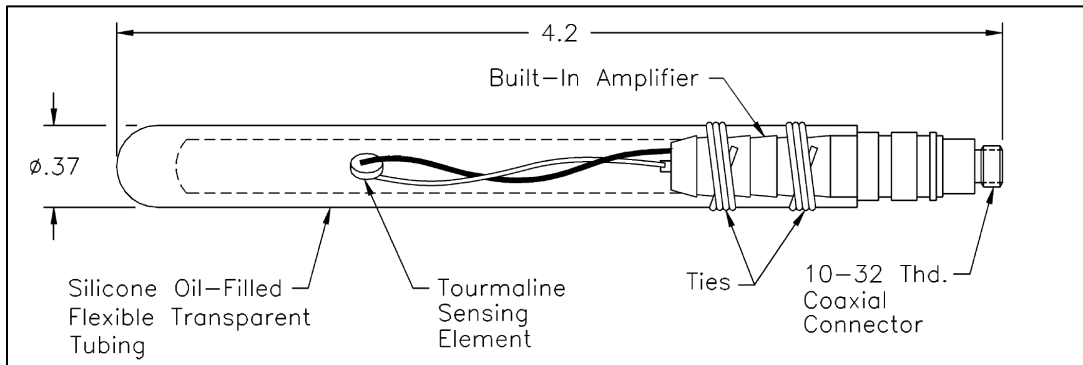


Figure 23. Underwater blast pressure sensor, 138 Series (short length). Source: [26].

All three pressure sensors used in this research were anchored above the coaxial connector with 449g, 450g, and 450g, of weight respectively. Anchors consisted of galvanized bolts with their centers bored through to permit the flexible silicone tubing of the sensor to fit through the bolt hole. This eliminated the need to use monofilament line as the connection point between the sensor and the anchor, which helped to effectively reduce the laboratory set-up time required especially for AB testing. The final set-up included additional nuts and washers to achieve the optimal anchor weight needed for the sensors is shown in Figure 24.

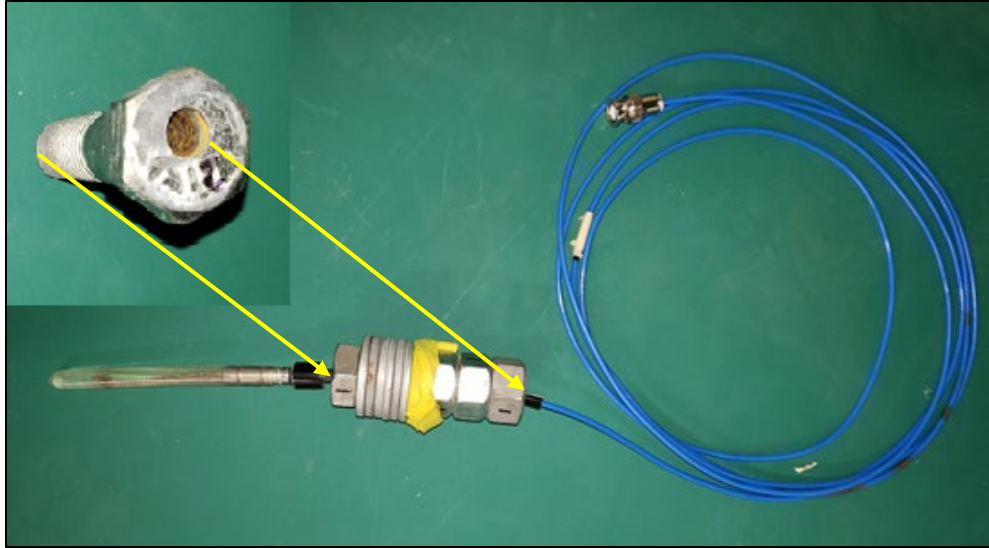


Figure 24. Pressure sensor anchor design with hole through bolt shown in top left

Voltage measurements from the blast sensors move directly to the DC signal conditioner as an AI shown in Figure 25. From the signal conditioner the AIs are transported over three BNC cables to the first NI piece of equipment, the NI BNC 2110 pictured in Figure 26. From the BNC 2110, the signals move to the NI PXIe-6358 for signal conditioning, data processing, and export.

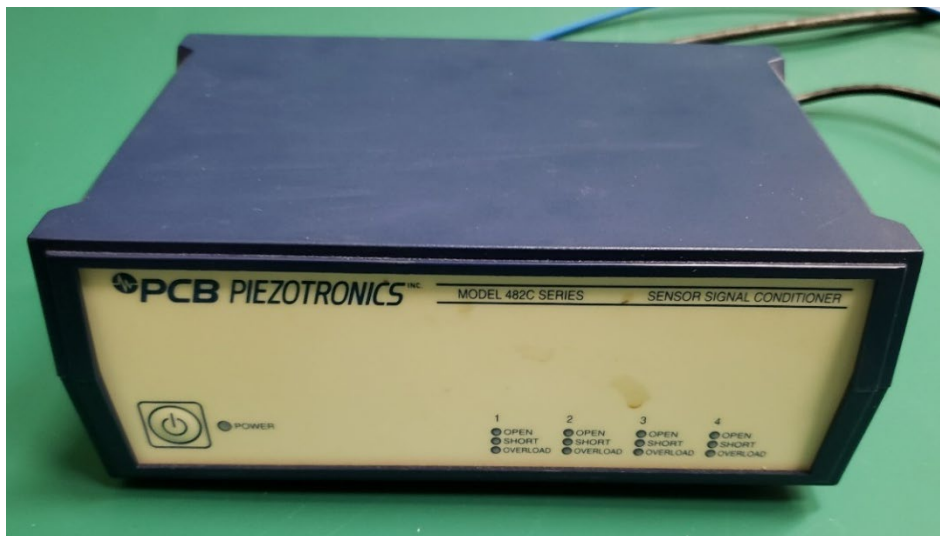


Figure 25. Model 482C signal conditioner for pressure data collection

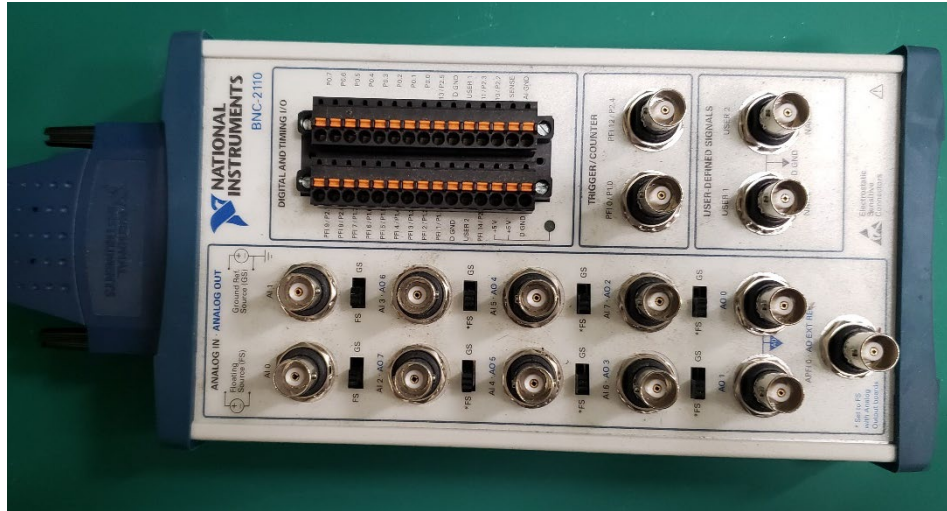


Figure 26. BNC 2110 AI interface with PCB signal conditioner

E. LIQUID NITROGEN

Two different loading methods were used to induce underwater shock loading on the different composite plates. The first method used a similar process conducted by Crow, using a polyethylene terephthalate (PET) pressure vessel (PPV) filled with liquid nitrogen (LN₂), which induced rapid failure of the pressure vessel underwater [21]. LN₂ has an expansion ratio of 1:694 and a vaporization point of -195.8°C (-320.5°F) [27]. Therefore, approximately 50 mL of LN₂ at ambient temperature can produce 32.45 liters of nitrogen gas if permitted to expand fully. Approximately 50 mL of LN₂ was used for each test run conducted with LN₂, where the filled PPV was attached to a monofilament line for anchoring once the bottle was in the AWT as shown in Figure 27. Vaporization of the liquid nitrogen led to rapid expansion of the bottle due to accumulated nitrogen gas. Once the bottle ruptured the expanding pressure wave propagated out towards the composite plate fixed to the CTR.



Figure 27. PPV anchor attachment

Several drawbacks were identified for this shock loading method. One limitation for this method was the inability to control the orientation (vertical, horizontal, angled etc.) of the PPV upon entry into the AWT once testing commenced. This means variation and effects of directionality of the propagating force were anticipated. Failure mechanics of the PPV were thought to be inconsistent in regard to failure location on the PPV. This meant even if the orientation and position of the bottle could be controlled, the region where the PPV fails could not be. Increased variation of directionality of the loading force was expected because of this observation. Additionally, the quantity of liquid nitrogen could not be precisely measured for each test run which made it difficult to replicate the amount of liquid nitrogen used test to test. It was posited this led to result in greater variation of the maximum pressures measured by the lab instrumentation. Furthermore, burst pressures and material properties were not readily available to the public from Coca-Cola[®]'s or Dr. Pepper[®]'s 16.9 oz PET bottles, making it harder to validate the pressures measured by the pressure sensors at failure. Finally, since the end goal was to design and implement an experimental method that resembles loading behavior and response more similar to that in naval applications, the total energy imparted by this loading method as well as its decay constant associated with it, meant it presented greater difficulty for accurate scaling and analysis.

F. CASPUR

The Compressed Air Shock Pipe Underwater Release (CASPUR) system was designed to replace the LN₂ shock loading method, to provide a more repeatable result, yielding consistent loading data for each successive test run. This method allowed for precise control of the directionality of the shock loading against the composite plate as well as a predictable and known magnitude of the loading. Three primary sections comprise the CASPUR system: the compressed air-supply system (CASS), the Shock Test Rig (STR) (analogous to the CTR rail design), and the shock pipe assembly, which includes the shock pipe itself and the rupture disk and holder. Since this research was primarily concerned with naval applications, good corrosion resistance of the system materials was integral to the performance, safe operation, and longevity of the system. Bearing this in mind, stainless steel 304 or 316 was utilized for every fitting except for two fittings which will be described in greater detail in the forthcoming sub-sections of this chapter.

All fittings were intentionally kept as small as was practicable for two primary reasons. First, smaller fittings were more readily available off the shelf if future modifications were needed for CASPUR. Second, 6.35 mm (0.25 in) fittings were intended to reduce a jetting effect towards the plate at the moment of pressure release when the rupture disk fails. The desired result are bubble mechanics similar to those described in the literature review in a non-contact UNDEX event. By keeping the fitting size small up to the shock pipe assembly, greater control was gained over the volume of compressed air released into the AWT. Due to the speed of propagation of the shock front, the effect of bleed off air pressure that remained in the CASS was assumed to be negligible in its added loading effect on the CFRP plate. Testing CASPUR to obtain pressure characterization as well as capturing high-speed imagery underwater would be integral to validating this assumption. Tightening all compression fittings was conducted in accordance with the manufacturer's guidance, and threaded fittings were sealed using 6.35 mm (0.25 in) and 12.7 mm (0.5 in) polytetrafluoroethylene (PTFE) tape. The following components comprise the CASS portion of the CASPUR system design:

1. CASS Design

a. Tank

A 17.93 MPa (2,600 psi) Industrial Air grade, Type K, tank was used as the compressed air supply for CASPUR, and is shown in Figure 28. The tank volume is 0.044 m³, stands 129.54 cm tall, with a diameter of 22.86 cm [28].



Figure 28. (a) Installed K-type industrial air compressed tank, (b) CGA-590 connection fitting, side-view, (c) CGA-590 connection fitting, front view (brass material)

This tank is connected downstream via a Compressed Gas Association (CGA)-590 adapter to a 6.35 mm (0.25 in) National Pipe Taper (NPT) adapter fitting to allow for

conventional components to be connected in series. The CGA-590 adapter is pictured in Figure 29, and it is connected directly into the High-Pressure inlet port of the two-stage regulator.

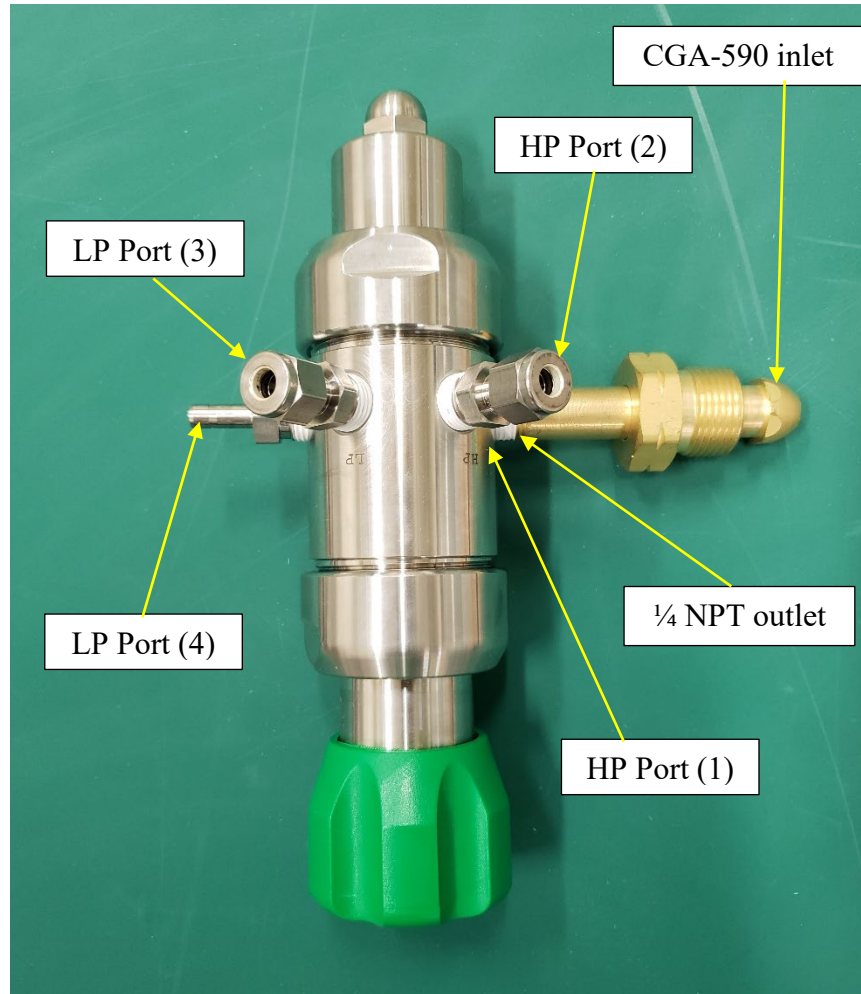


Figure 29. Four-port, stainless steel, two-stage regulator, with attached CGA-to-NPT adapter brass fitting

The CGA-590 adapter is made of brass and was one of only two non-stainless-steel components of the entire CASS and the shock assembly. This was because the female inlet of the compressed gas tank is also made of brass, and so the material similarity ensured a leak tight seal between these two components.

b. Regulator

A two-stage, stainless steel single knob regulator, seen in Figure 29, was rated for 0–3.45 MPa (500 psi) outlet pressure. This regulator provided sufficient supply pressure to break the rupture disk. This operating pressure range was also chosen so that stronger materials can be tested in future unto failure. Pressure in the CASS equalized downstream of the regulator to the set low-pressure (LP) outlet pressure of the regulator. Two-stage regulators provide more control of the fill rate of the system and less fluctuation of the incoming pressure from the supply side which were both desirable features for this research application. The two-stage regulator installed for this design has four total ports, two high-pressure (HP) and two LP ports also annotated on Figure 29. The first HP port (1) acts as the inlet from the compressed air tank to the rest of the CASS, and the second HP port (2) provides connection for gage (1) shown in Figure 30, which gives general readings of the current tank pressure. Connections for the HP port (2) and LP port (3) are threaded NPT-to-tube adapter fittings to allow for custom alignment of the gages facing the system operator. The first LP port (3) acts as the secondary gage connection point to provide a general reading of the pressure in the downstream portion of the CASS up to the rupture disk, and the second LP port (4) acts as the downstream outlet for the regulator to begin filling the CASS. LP port (4) has a ¼ NPT-to-tube adapter fitting for direct connection to the first check-valve.

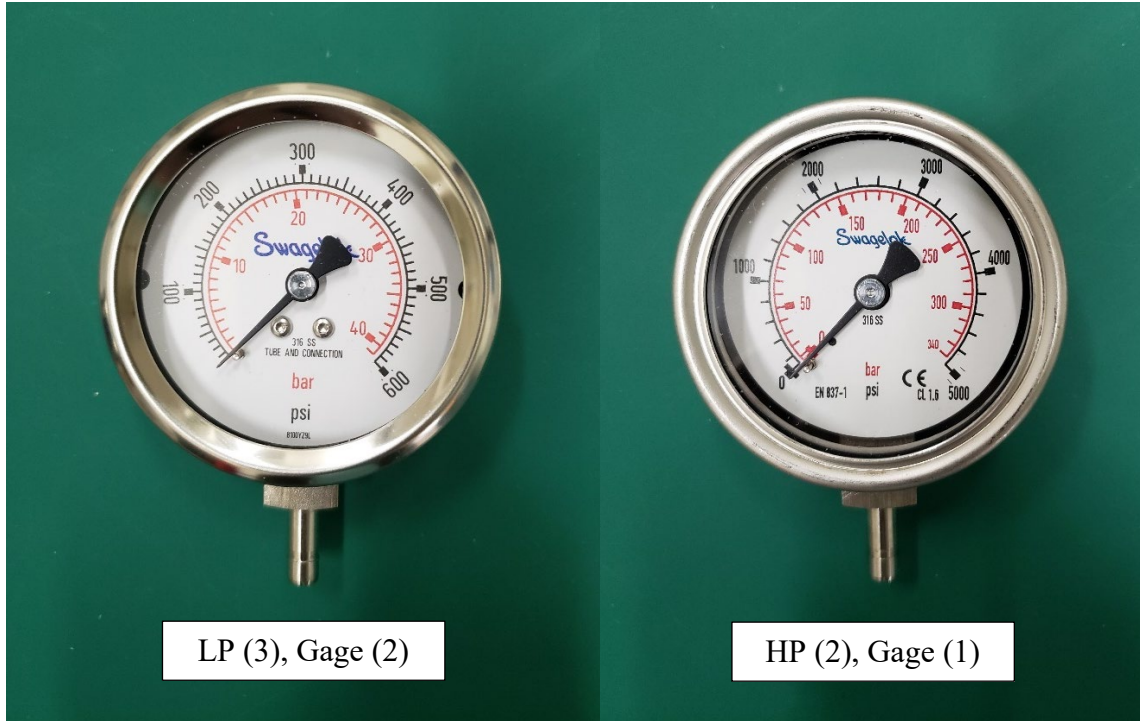


Figure 30. Inlet and outlet HPG-1 and LPG-2 regulator pressure gages

c. Check-valve

This first check valve pictured in Figure 31, primarily provided back-flow protection for the regulator. The check valve requires 68.95 kPa (10 psi) to fully open and can withstand sufficient back pressure, although very little was expected for this specific open loop system. A union tee is connected directly in series downstream of the first check-valve.

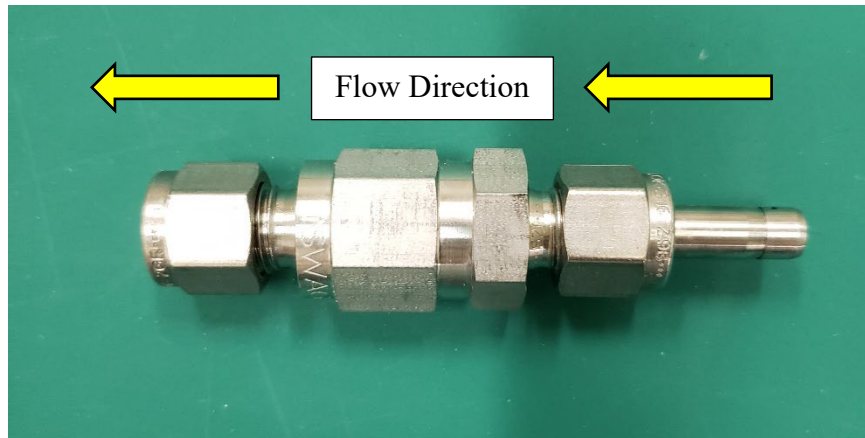


Figure 31. First check-valve, regulator backflow protection

d. Union tee

The union tee seen in Figure 32 was used to provide both a venting connection and cut-off connection for the overall system.

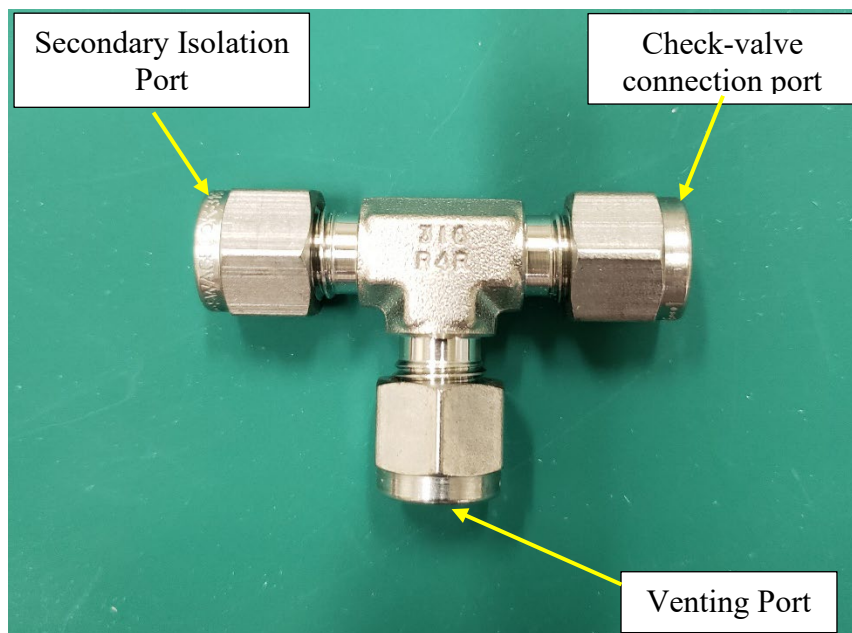


Figure 32. 1/4 tube connection union tee fitting for venting and isolation

For the safety of the operators and care of the CASPUR system, it was imperative that the entire system be completely de-pressurized when testing was not being conducted.

This union tee provided that necessary connection to the first vent and cut-off valve to accomplish this.

e. Primary safety cut-off and vent valve

The two-way isolation valve, shown in Figure 33, ensured the system line can be fully depressurized between the compressed air tank and the rupture disk in the shock assembly. In the event the rupture disk does not break, CASPUR would need to be fully de-pressurized prior to investigating any source of error. Additionally, the cut-off valve reduces the long-term loads on the regulator which the regulator was not designed for.

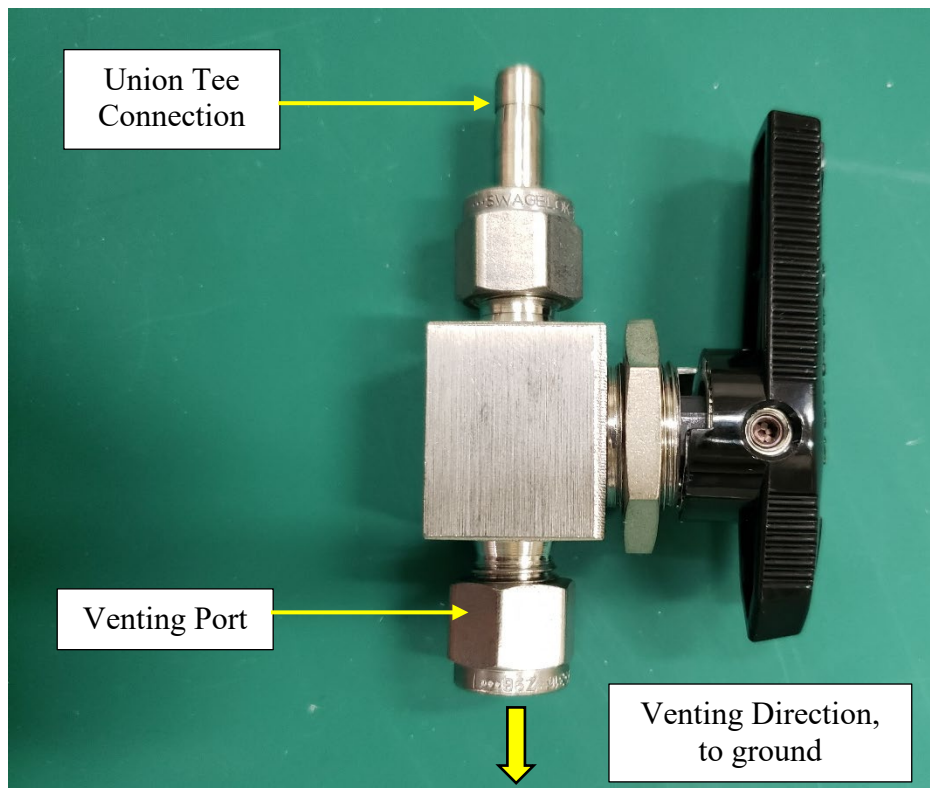


Figure 33. Primary two-way isolation cut-off and venting valve

f. Secondary cut-off valve

This valve is identical in form and capabilities as the primary cut-off valve and provided redundant isolation capacity of the high-pressure portion of the system to the low-pressure side.

g. Reducing elbow

The reducing elbow shown in Figure 34 reduces the overall long-term stress on the flexible hose that connects the rigid portion of the CASS to the moving carriage and shock assembly on the STR. Stress was reduced in the hose by concentrating the load on the center of the hose body and away from its end connection tube fittings. A reducing elbow ensured the bends in the flexible hose are focused away from its end fittings towards the center of the hose length where it is best designed to flex without incurring any damage.



Figure 34. Reducing elbow for hose performance and longevity

h. Flexible hose

A custom length 9.14 m (30 ft) 316-SS braided flexible hose show in Figure 35 was used as a flexible connection between the first check valve near the second safety cut-off

valve and the final tube to NPT adapter fitting. A p-shaped enclosure affixed to the STR was designed to provide room for the flexible hose when coiled properly to expand and contract without adversely stressing the hose during the raising and lowering of the shock assembly via the carriage.



Figure 35. Flexible hose for out of water to in-water connection for testing

i. Tube to NPT adapter

A 6.35 mm (0.25 in) tube adapter fitting to a 12.7 mm (0.5in) NPT fitting permitted the system to utilize a modular design with all threaded components downstream of this final compression tube fitting. This NPT adapter fitting connected the tube fitting to a larger NPT threaded fitting, which enabled the first incremental increase of the diameter of the CASS up to the final 5.08 cm flange and rupture disk assembly. This is considered the last

component of the CASS, marking the transition to the shock pipe assembly portion of CASPUR.

2. STR Design

The shock test rig was built with similar components and materials as the CTR. A primary design goal of the STR was to provide a near rigid housing for the shock assembly to reduce energy loss and dissipation into the STR and maximize energy translation through the water into the CFRP sample plates. The STR stands 3.66 m (144 in) tall, and the 0.91 m (36 in) wet end feet rested perpendicular to the redwood panels on the bottom of the AWT for overall stability. The 0.92 m (36.25 in) dry end feet rested on the deck of the lab room outside of the AWT. Total weight of the STR exceeded 113.40 kg (250 lbs). Both legs along with a cross-rail support seen in Figures 36 and 37, provided a significant counter moment to the overall structure, which prevented tipping of the STR. This also ensured a solid test foundation for the shock pipe assembly. Four quad-rails provided a fixed track for the carriage to travel vertically into and out of the tank. Mechanical stops were installed on all four quad-rails so that when the carriage is fully submerged, the center of the shock tube assembly rested at the half-depth of the AWT as seen in Figure 36 (a). Tolerance was designed into the rail system to prevent binding from occurring between the carriage and the quad rails. Protective pine coverings were cut and installed with recessed connection points to protect the redwood panel bottom of the AWT from being damaged during installation, seen in Figure 36 (a) and (b).

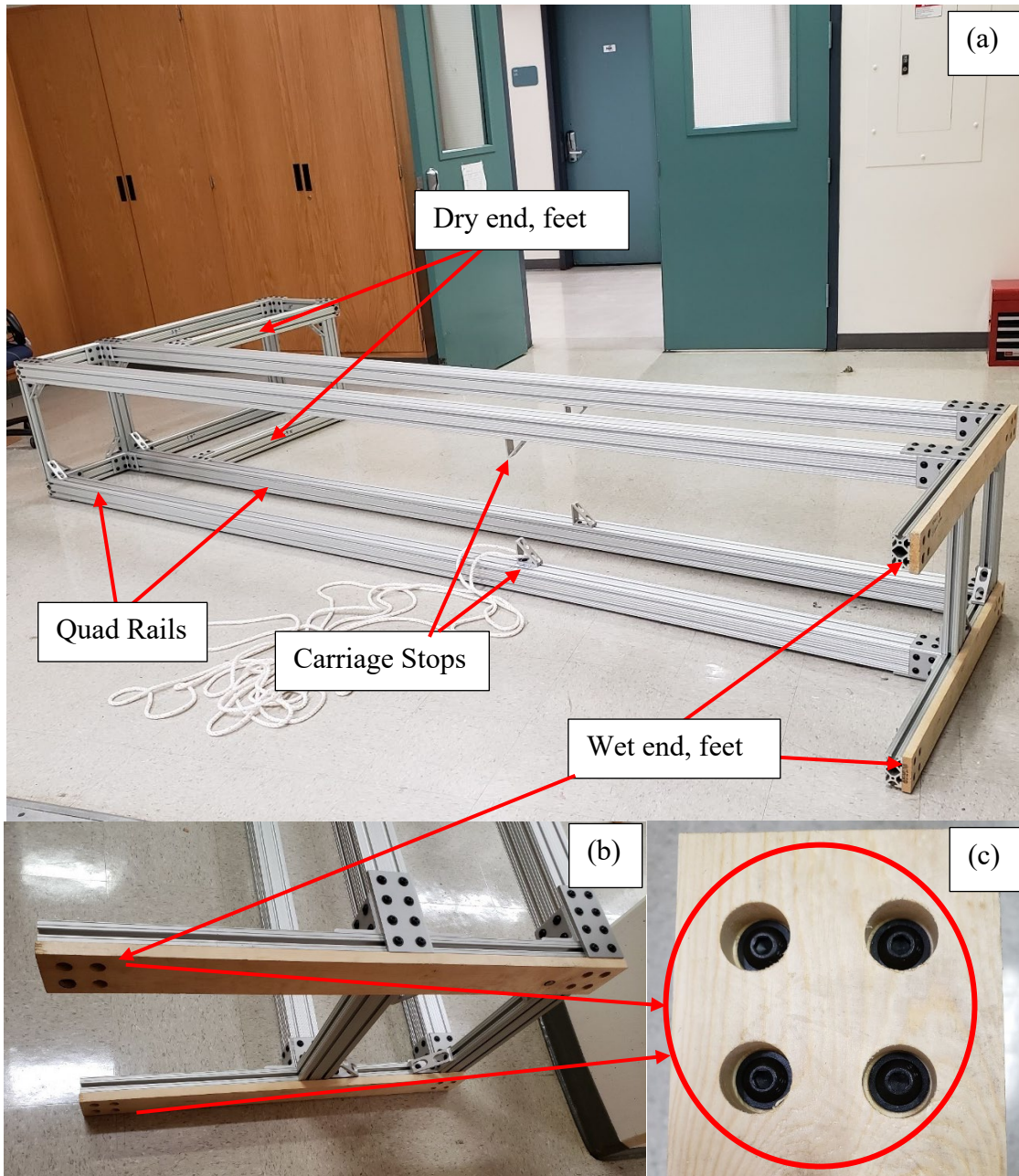


Figure 36. (a) Overall STR design without carriage installed, (b) wet feet guards, (c) recessed guard attachment points

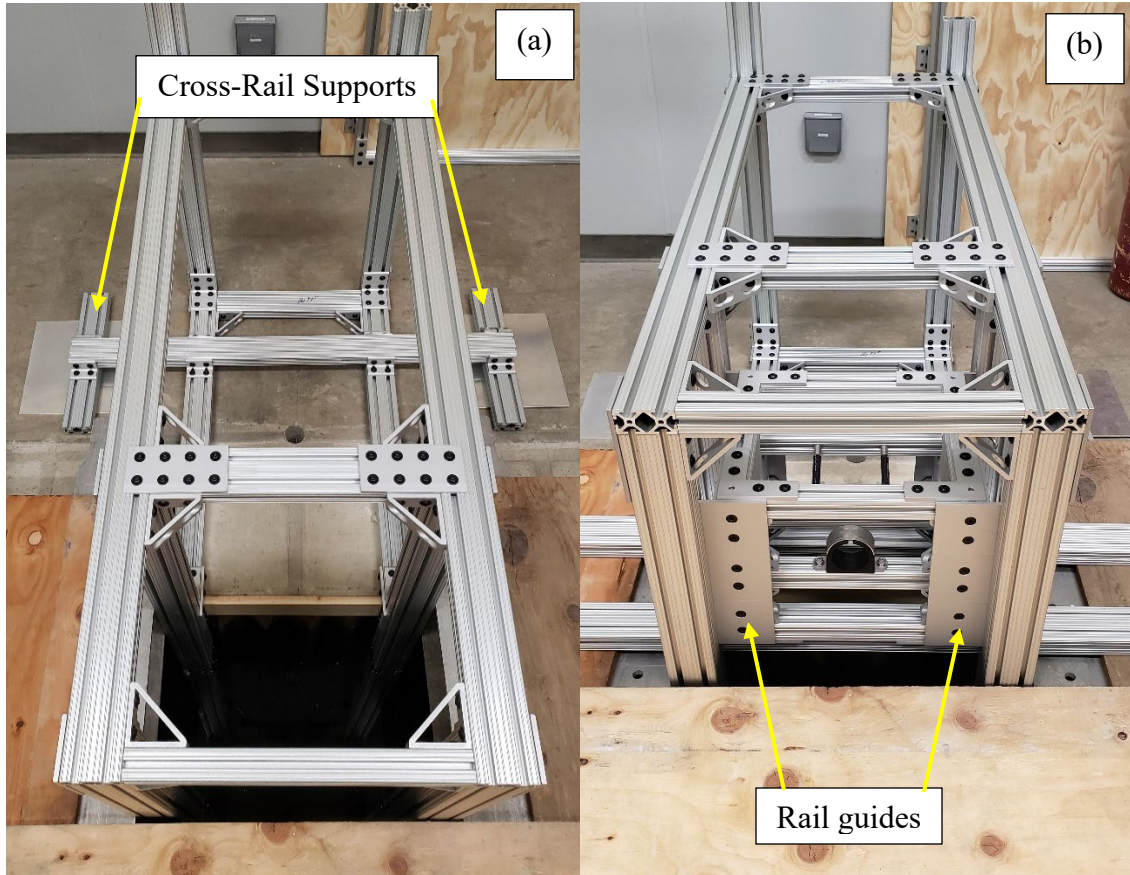


Figure 37. STR in place in AWT (a). Carriage installed onto quad-rails (b).

A total of 12 rail guides, six front and six in back are shown in Figure 37 (b) above, were installed on the exterior of the carriage to provide a smooth vertical travel of the shock tube assembly. The rail guides also ensured the carriage remained at a fixed position in the x-direction in the tank, even after the rupture disk broke. Eye bolts were fixed to the midpoint of each of the opposing sides of the carriage to provide a hoist point for raising and lowering the carriage seen in Figure 38 (a). Three cross-rails, back (1), middle (2), front (3), sat on the interior of the carriage to provide support underneath the shock tube assembly, and ensured the shock tube sat completely parallel to the x-plane as shown in Figure 38 (b). It was imperative for the shock tube assembly to sit as near parallel to the x-plane as possible to reduce inconsistencies in pressure loading magnitudes and the potential for unwanted directionality of the shock loading.

A 10.16 cm (4 in) U-bolt cushion was installed, primarily to prevent movement in the z-direction of the shock assembly shown in Figure 38 (b) and (c). Since the U-bolt width exceeded the diameter of the seams of the threaded 5.08 cm elbow, two additional rotational pipe stops were added to the middle rail (2) of the carriage to further prevent any rotational movement about the z-axis seen in Figure 39. A 5.08 cm (2 in) outer diameter vibration damping clamp was installed around the body of the pipe body to dissipate the energy transferred into the STR and the CASS when failure of the rupture disk occurred. This clamp also contributed to the resistance of the movement of the shock tube assembly in all three primary axes of rotation.

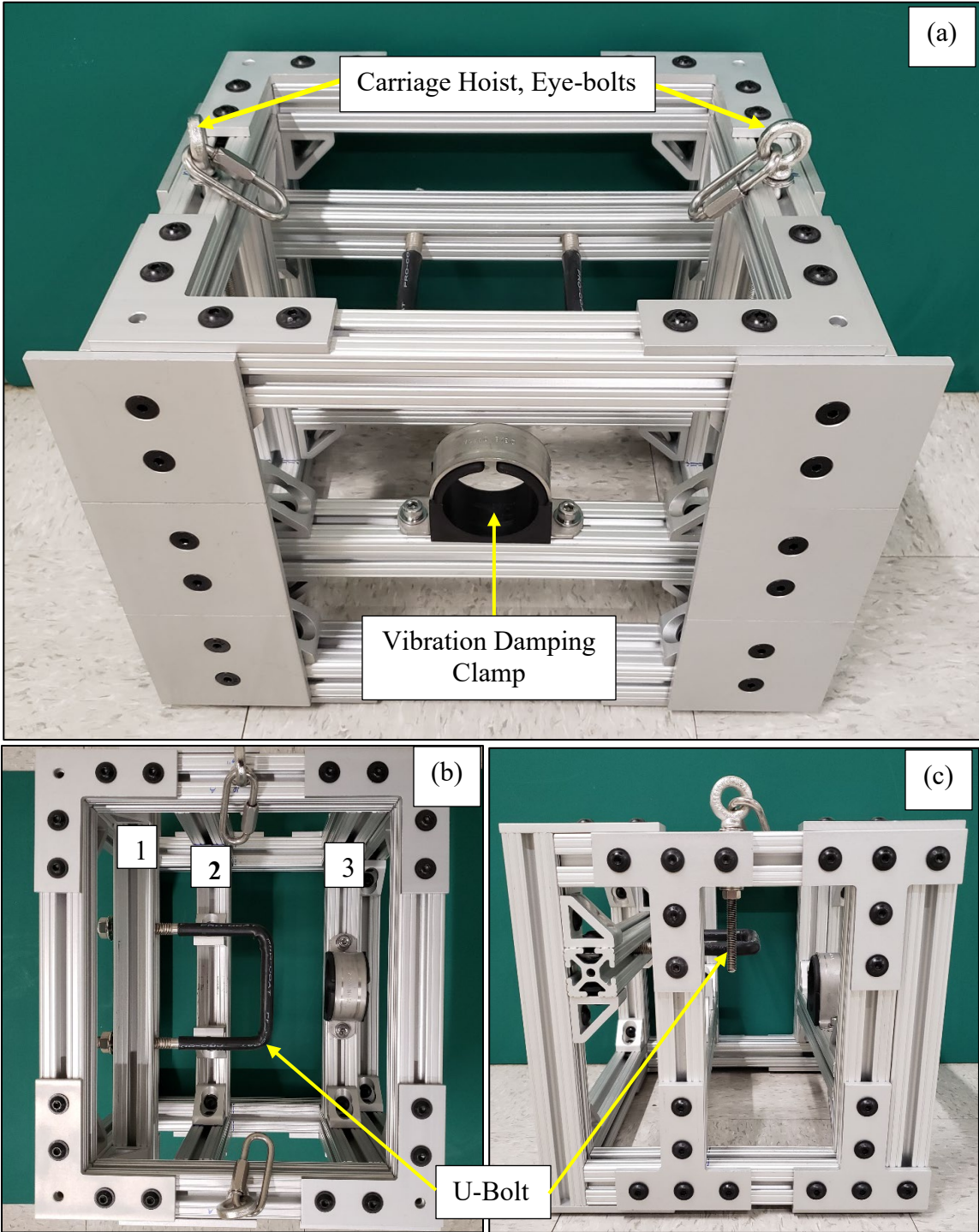


Figure 38. Carriage design: top-view (a), side-view (b), front-view (c)

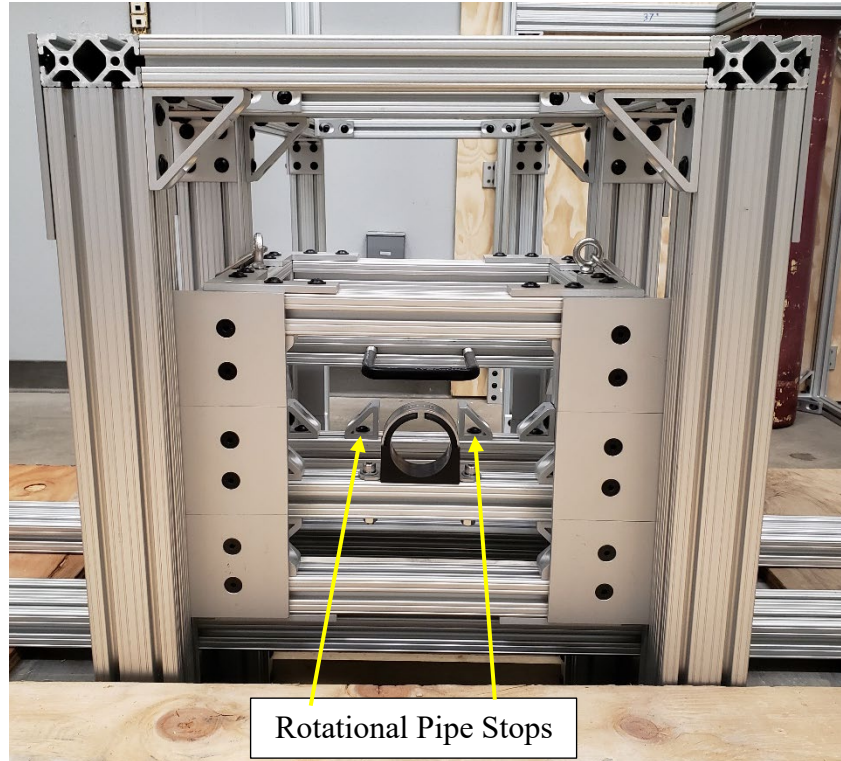


Figure 39. Carriage design, front-view, rotational stops

3. Shock Pipe Assembly Design

The shock pipe assembly consists of all 5.08 cm (2 in) fittings beginning at the hex bushing reducing adapter up to the final outlet flange of the assembly as delineated in Figure 40 (a). Threaded pipe connections were chosen between the elbow and the rupture disk assembly so that the internal volume of the shock tube could be altered. Under the LN₂ loading method, the internal volume of the PPV was approximately 500 cm³. For continuity of loading methods, a 0.15 m (6 in) length section of pipe was first used which is approximated to provide 500 cm³ of air volume prior to expansion. This volume accounted for the contribution of the space between the pipe section and the rupture disk assembly as well as the space after the 5.08 cm (2 in) hex reducer up to the inlet pipe section.

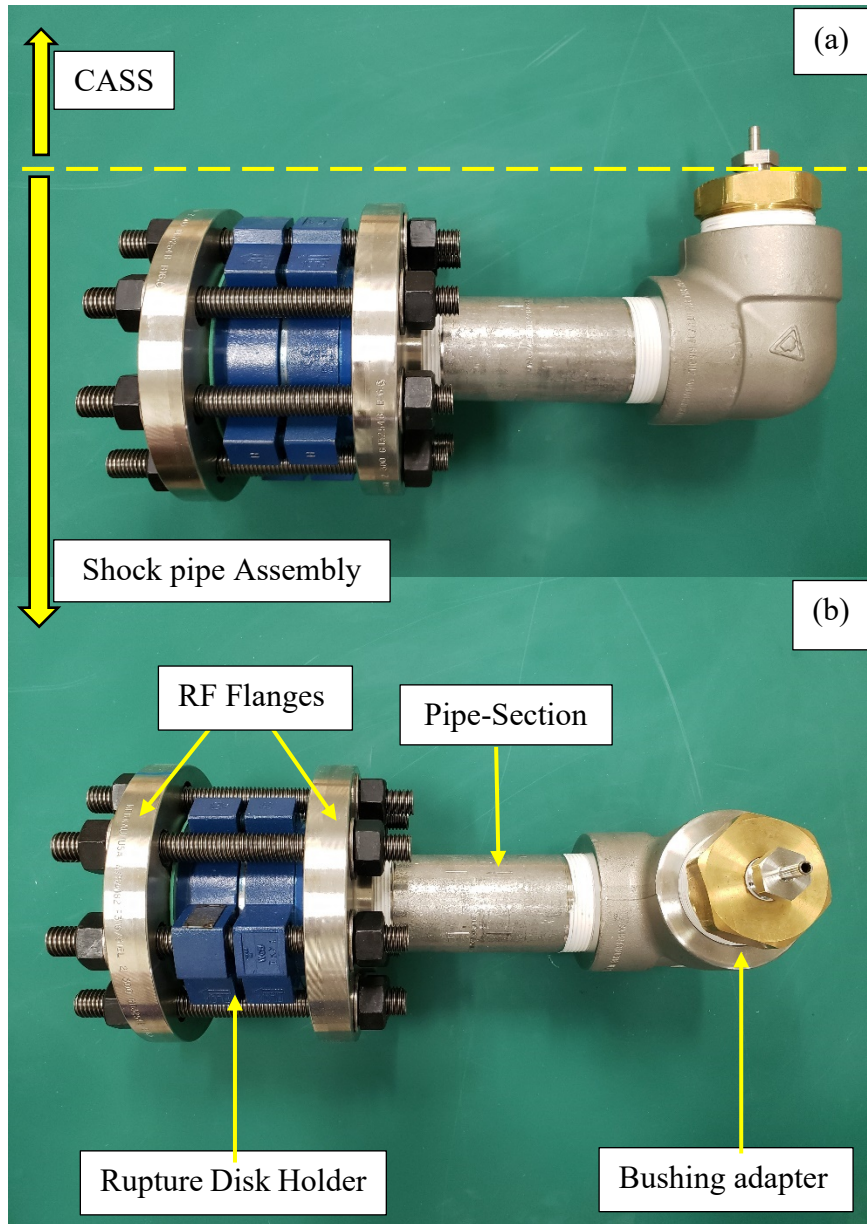


Figure 40. Overall shock tube assembly, (a) side-view, (b) top-view

a. Hex bushing reducer adapter

The bushing reducing adapter is a 12.77 mm (0.5in) NPT to 5.08 cm (2 in) NPT brass fitting to the 316-SS 5.08 cm (2in) elbow. This was the second and last brass fitting of CASPUR, other than the CGA-590 adapter. Due to material shortages present in the

industry for this size of threaded pipe fitting at the time of purchase, this alternate fitting was selected for its optimal corrosion resistance for a fully submerged application. Galvanic corrosion was not anticipated as long as the neighboring components to the brass reducer are dried at the completion of the day's testing [29]. Leakage at this dissimilar metal interface had potential for occurrence and was mitigated using a thread PTFE sealant [29].

b. Flanges

Due to the pressure range requirements for this initial proof of concept design, 300lb flanges, with eight 19.05 cm (7.5 in) studs, were required to be utilized shown in Figure 41. These flanges are pressure rated for 5.10 MPa (740 psi). Raised face (RF) flanges were chosen to provide the best seal between the flanges, gaskets, and the rupture disk holder. 1.59 mm (0.06 in) thick Garlock[®] gaskets were used for sealing the space between the rupture disk holder and the RF flanges. A specialty 300lb rated, Zook[®] FAH series, rupture disk holder shown in Figure 42 and 43, made of carbon steel, was used for this design.



Figure 41. 300lb RF flange

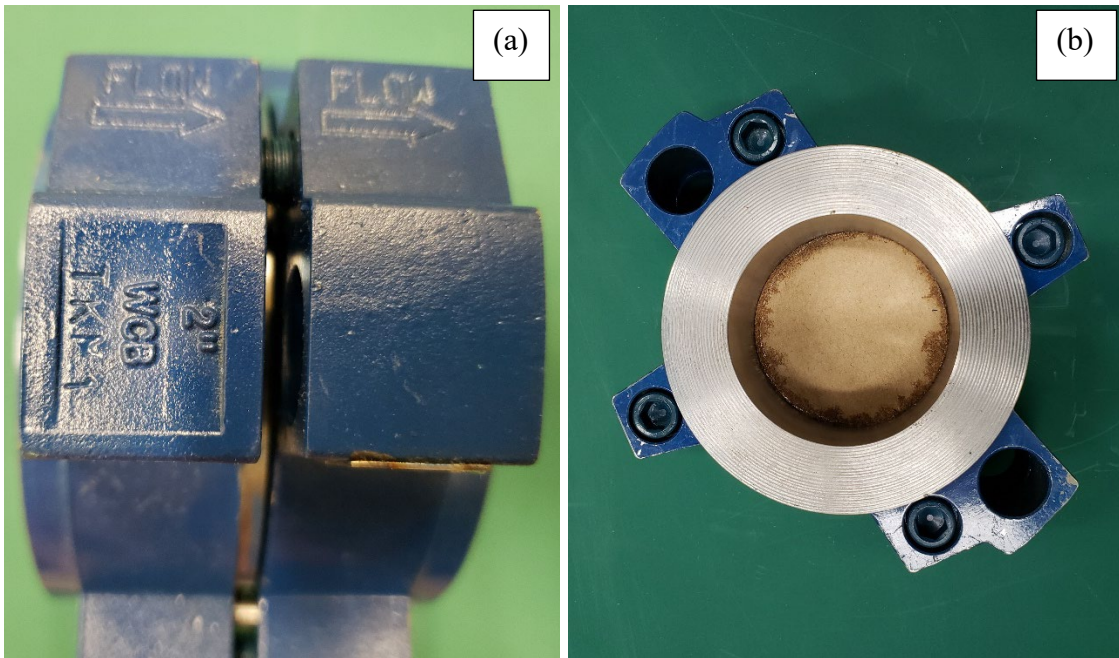


Figure 42. Rupture disk holder, FAH series: (a) side-view, (b) front-view

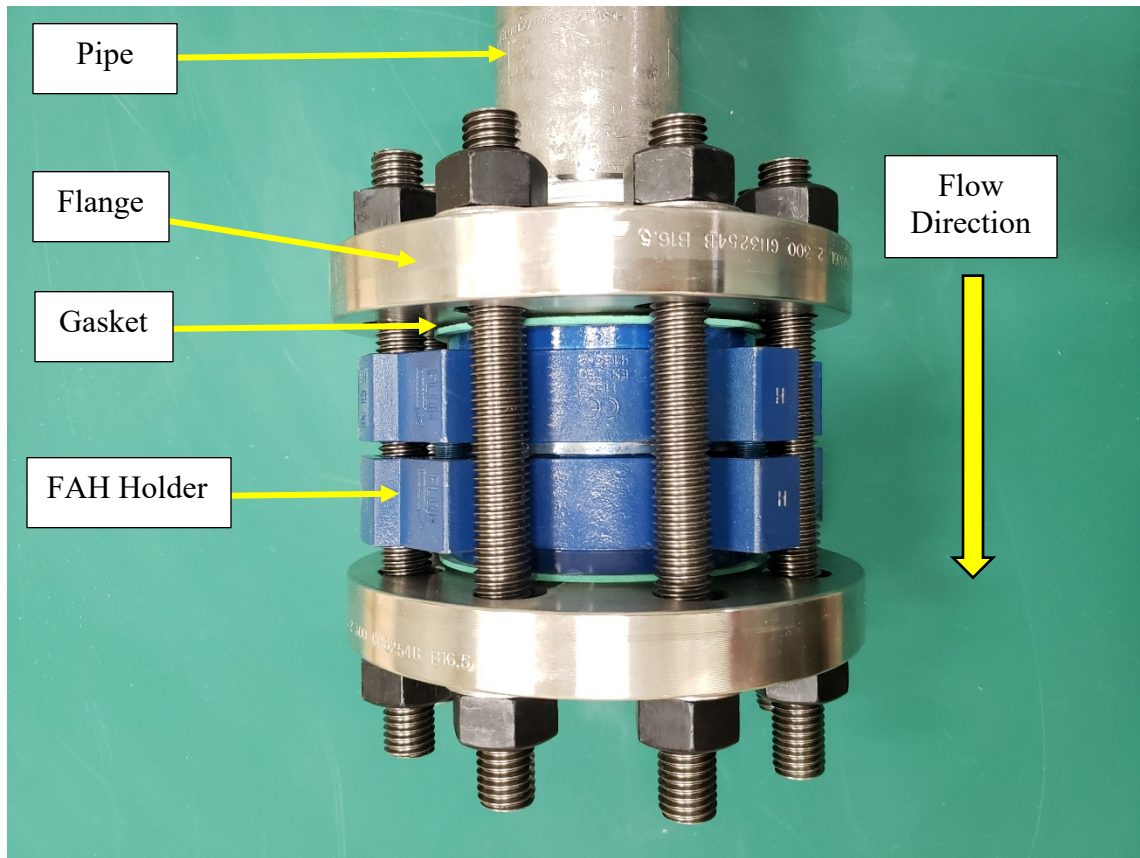


Figure 43. Rupture disk holder design: above-view

Torque requirements for the rupture disk holder and the bolted flanges spanning the holder were followed in accordance with the specification from the rupture disk manufacturer. Rupture disks were manufactured from 316 Stainless Steel to a specified rupture pressure of 2.07 MPa (300 psi) (+\ -5%). Rupture disks used for this research had an inner opening diameter of 5.08 cm (2 in) and can be seen in Figure 44.



Figure 44. Non-fragmenting stainless-steel rupture disk: (a) inlet side (b) outlet side

III. TEST SEQUENCING

The test sequencing for this research progressed in four phases A through D. Each sample was tested comparatively with a similar series of stand-off distances, using approximately the same volume of liquid nitrogen, but with alternate backing conditions of AB and WB. The testing sequence for each sample began at 0.61 m (24 in) and then moved closer at intervals of 0.15 m/test run (6 in/test run) until failure was observed in the composite plate shown in Figure 45. The closest the specimens were to the charge was 0.15 m (6 in) which delineates the divide of the near field/far-field [4]. Primarily, this minimum stand-off distance was to avoid fragmentation potential with both the plate and the sensors from the charge debris.

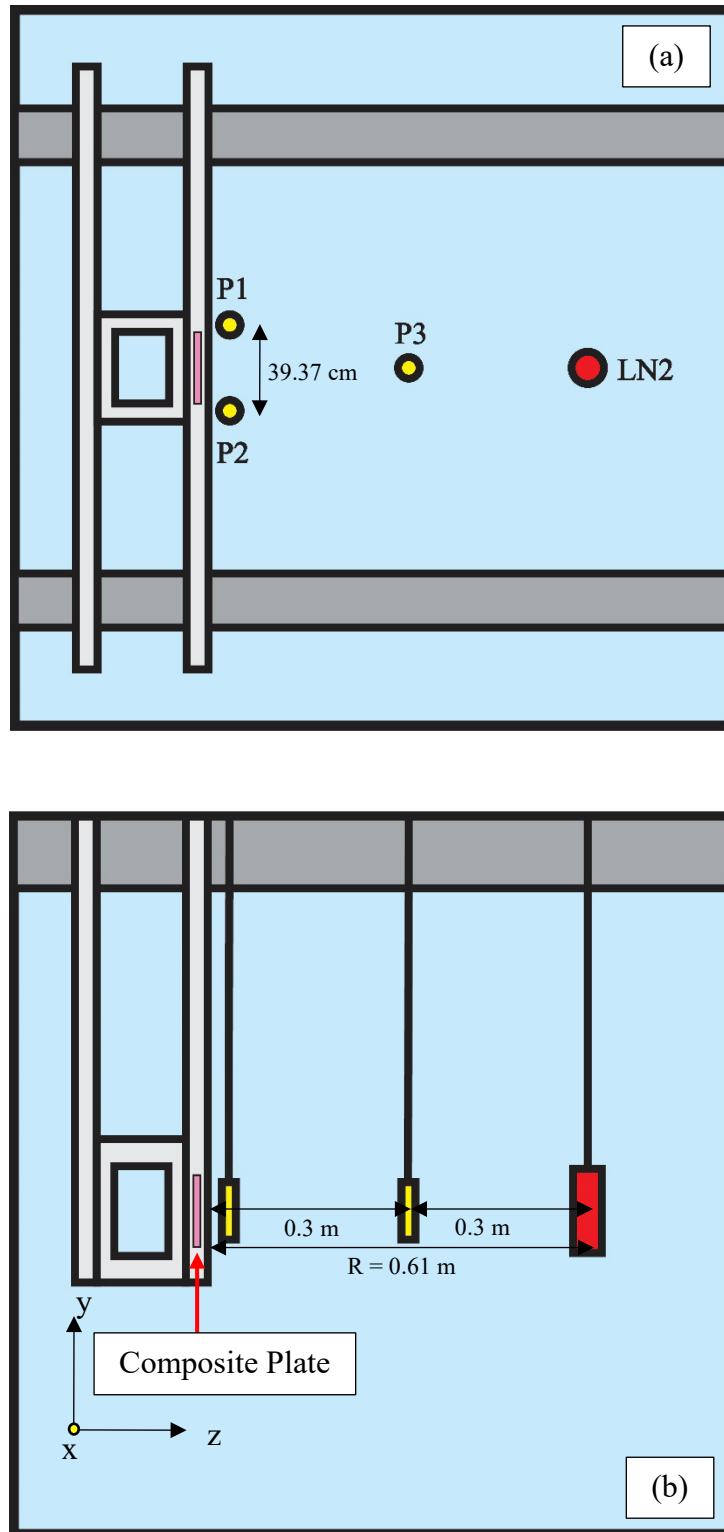


Figure 45. Test layout at $R = 0.61$ m (24 in): (a) top-view, (b) side-view

A. PRESSURE SENSORS

The aim of the first phase of testing was to establish the efficacy of the pressure sensors and to characterize the pressure profile using LN2 without any composite plates in the AWT. For this testing phase, the CTR was not in the water. The only items suspended in the AWT were the three underwater blast sensors and the PPV filled with 50 mL of LN2. Three different layouts were implemented throughout this research and are shown Figure 46 looking from above down onto the experimental layout. The first two layouts, linear and triangular, were used for Phase A in the test sequencing. The standard layout was used for Phases B-D. A linear layout was used to determine the effective attenuation of the shock wave through the water. This layout provided characterization of the pressure profile in comparison to the pressure profiles of more conventionally used explosives.

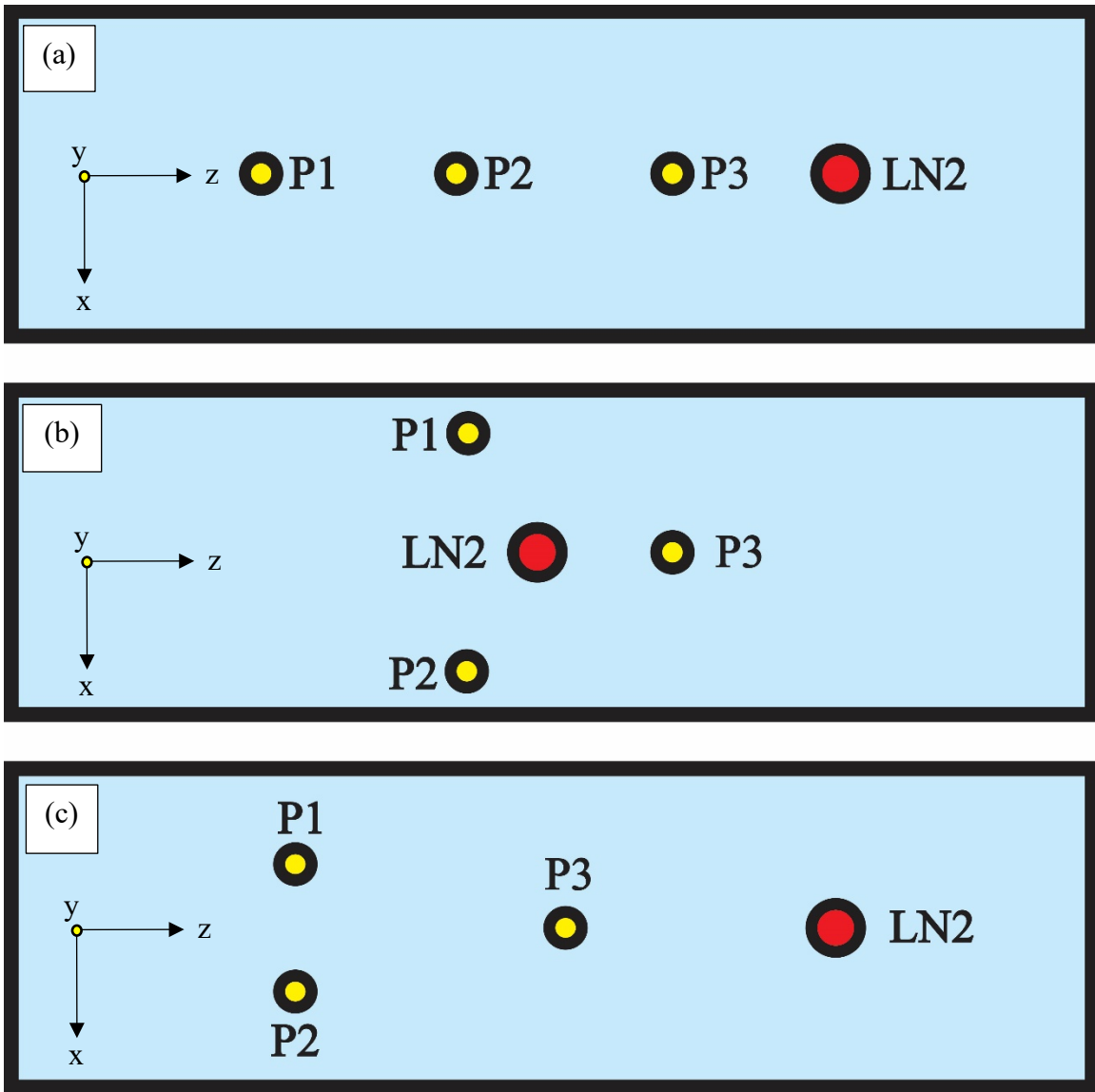


Figure 46. Pressure sensor layouts: (a) linear (b) triangular (c) standard

A linear layout provided a resource to curve fit the data and extrapolate backwards for a better estimate of the true peak pressure that occurred at the center of the charge. This layout also helped to validate if the shock pressure of our loading source followed that of an exponentially decaying curve over time and stand-off distance. Pressure sensors can only be placed so close to the charge source, so that the true peak pressure will likely be missed due to the instantaneous dissipation of energy into the surrounding fluid medium [30]. Reasonable extrapolation through curve fitting will be pursued in the results section

for further pressure analysis. Because opportunities for inconsistency were believed to exist in the loading mechanism, as discussed in the LN2 portion of Chapter II, this helped to quantify how significant those inconsistencies might be. The second pressure sensor layout, described as triangular, where each sensor was equidistant from the loading source at $R = 0.3 \text{ m}$ (12 in) is shown in Figure 46 (b). The primary purpose of this layout was to examine whether directionality existed in the shock front from the PPV. A perfectly vertical orientation of the bottle was not assumed, and failure location of the PPV was assumed to vary between each PPV. This layout helped to understand whether the bubble formation as well as pressure front radiated spherically as is observed in conventional explosives. The sensors were energized via the signal conditioner and were provided sufficient time to normalize prior to data collection. Once the pressure sensors normalized, their functionality was confirmed by utilizing the NI Max application to observe the live signal of the sensor and its proportional response to an applied small static load. A GoPro[®] camera was utilized to observe the geometry of the initial bubble expansion, contraction, and venting, as well as the failure sequence of the PPV.

B. SINGLE SQUARE PLATE WATER BACK

Phase B of this research investigated the response and failure of composite structures using the LN2 loading method in a WB backing condition. This set-up followed Crow's experimental set-up closely to provide continuity of research prior to significantly changing the experimental set-up [21]. Water back for the purposes of this research describes the fluid medium at the front of the CFRP plate to be water and the fluid medium of the back of the CFRP plate to be water. In this design water was able to move freely in out of the box, which is a distinct difference between the design of LiVolsi's experimental apparatus for WB and AB testing [13]. Primary initial changes to the test rig in this research from Crow's were the reduction of the window size to 0.24 m by 0.24 m (9.5 in by x 9.5 in). The modifications made in this test rig provided flexibility in future test set-up schemes which was not available in the original CTR [21]. Additionally, this rig suspended the composite plate at the exact half-depth of the AWT. This was to provide symmetry to the greatest extent possible for each stand-off distance and backing condition tested. For the single square plate water-back, the samples were fixed to the front of the box of the CTR.

Clamped boundary conditions were used for each sample set-up for both water-back and air-back. This boundary condition was expected to lead to stress concentration near the front and rear backing clamps as described in the literature review [2].

C. SINGLE SQUARE PLATE AIR BACK

Phase C of this research explored the response and failure of composite structures due to underwater shock loading in an AB backing condition and used the LN2 loading method. AB, for the purposes of this research, describes the fluid medium in contact with the front of the CFRP plate to be water and the fluid medium in contact with the back of the plate to be air. For the air-back set-up, it took several iterations for the box to achieve sufficient watertight integrity so that a true air-back environment was achieved. A CFRP plate, nominally 0.3 m by 0.3 m (12 in by 12 in) plate of varying thickness was used to seal off the back of the box.

When the backing condition changed for the box from WB to AB, the buoyancy of the box was evaluated so that the CTR still rested on the deck of the AWT. F_B calculations were made for the box utilizing Archimedes' Principle to estimate the F_B generated by the CTR. The rails were removed from the CTR and weighed on a scale, and similarly the box was weighed individually to determine the net F_B by subtracting the weight of the rig from F_B . The mass of the CTR was found to be 63.50 kg (140 lbs) by weighing it on an industrial scale, and the net buoyant force then was determined to be 23.38 kg (51.55 lbs). A holding tray was made at the top of the rig which allowed for additional weight to be added to the rig as it is submerged into the tank. 38 kg of steel pipe sections were added in the following manner in Figure 47 to overcome the F_B on the test rig.

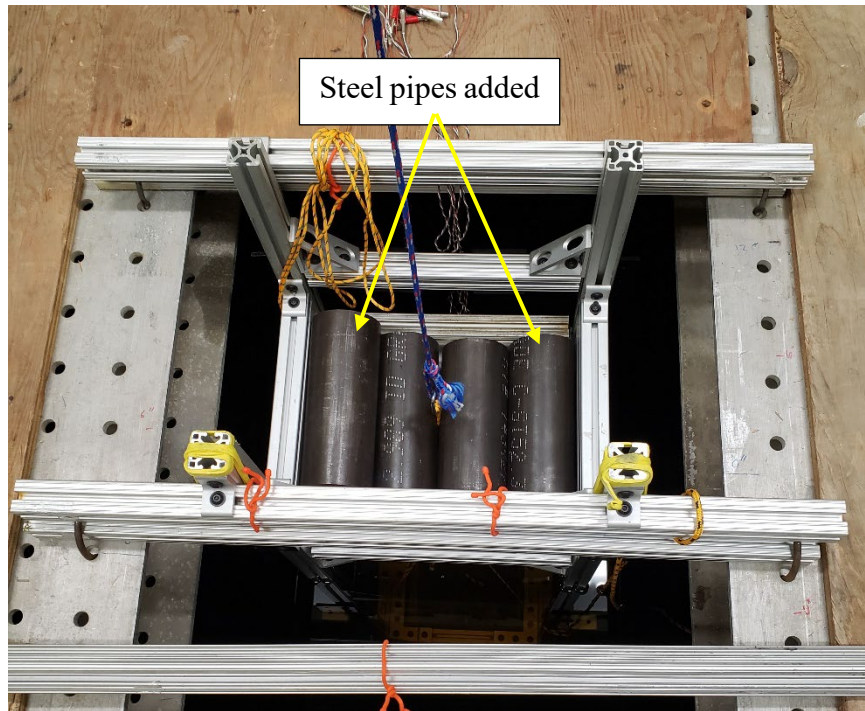


Figure 47. Steel piping added to holding tray to overcome buoyant force of CTR

Due to the load limits of the pulley system being used to raise and lower the test rig in and out of the AWT, the additional weight was not placed on the tray of CTR until the box touched the water. Once all four pipe sections were added, F_B was sufficiently overcome by the weight of CTR, so it rested securely on the deck of the AWT. Finally, because the additional weight of the rig was added higher up on the test rig, the overall stability of the rig was negatively impacted since the center of gravity moved upwards significantly. Instability of the CTR in the AB condition was reduced by fixing two cross bars perpendicular to the aluminum I-beams shown in Figure 48. This reduced the moment arm of the test rig and its tendency to lay down forward or backward prior to being fully submerged.

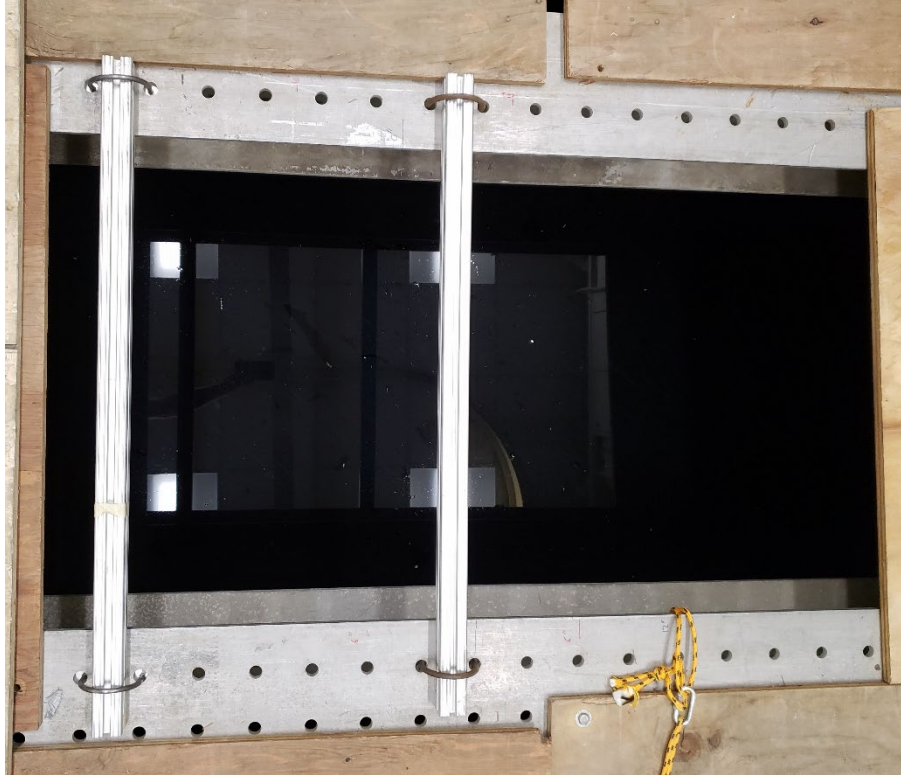


Figure 48. CTR stability rails for AB testing

Finally, to prevent leakage into the box during AB testing while still maintaining a pathway for the strain data to move from the plate to the DAQ, the back of the box was sealed off with a previously used composite plate, and the wires were fed through an orifice at the center of that back plate. A zip-tie was attached on the inside the box to protect the strain gages from damage during the placement process of the CTR before testing commenced. Both the inside and outside gaps between the wires and the composite plate were filled with a flexible duct seal to prevent further water intrusion shown in Figure 49.

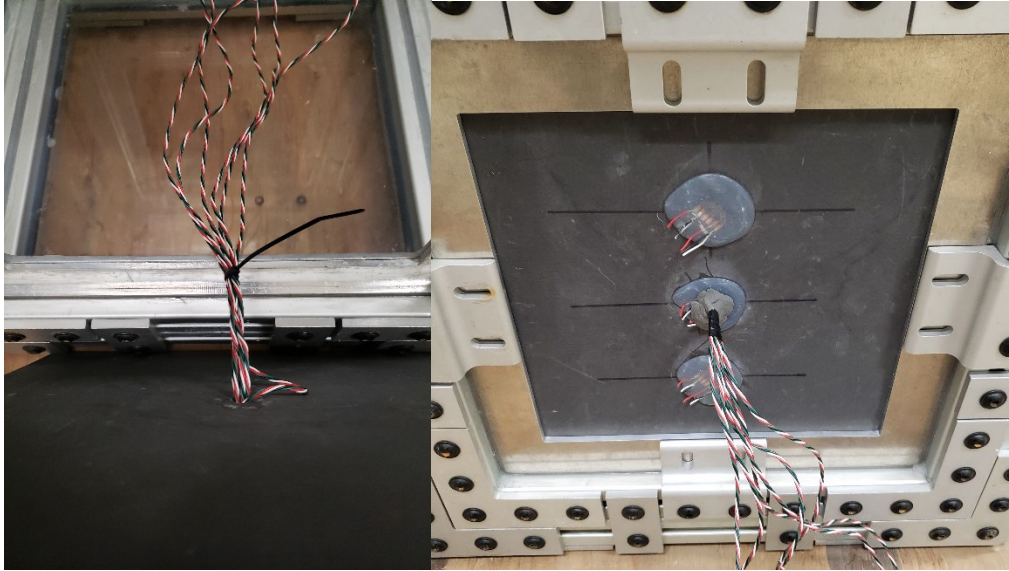


Figure 49. Wire routing for AB CFRP testing set-up

For every test run in Phases B and C, underwater rated lights were used to illuminate the test rig which ensured minimal leaks occurred prior to testing. An acceptable amount of water in the bottom of the box was determined to be less than 6.25 cm (2.5 in). This was where the edge of the composite plate began when fixed to the box of the CTR.

D. DOUBLE SQUARE PLATE WATER BACK

The composite test rig was designed to allow for a composite plate to be on both the front and back of the rig. It was unlikely any noticeable structural response would be detected in a fully double-sided AB condition. This was because reflected energy was expected due to the impedance mismatch of the water and air. As a result, this configuration was not investigated in this research. However, valuable insight for WB FSI interaction between two plates would be gained and would have practical implications for marine and naval applications.

THIS PAGE INTENTIONALLY LEFT BLANK

IV. RESULTS AND DISCUSSION

A. PRESSURE RESULTS

With the limitations of this research in regard to the LN2 shock loading method, it was still important to look for similarities in those results using an explosive source with unknown properties compared to the well documented properties of conventional explosives described by Costanzo [4]. Several PPVs were able to be recovered by switching from a 66.72 N (15 lb) monofilament line to a 711.72 N (160 lb) capacity, 3.18 mm thick synthetic rope. Recovered bottles allowed for the identification of patterns in failure location and failure geometry as show in Figure 50.



Figure 50. Recovered failed pressure vessels from pressure characterization testing

From the Figure 50 above along with more than 60 additional pressure vessels recovered from the bottom of the AWT, no clear failure pattern was identified. Failure could be seen in the feet, body, and neck of the pressure vessel, with no dominating failure

location observed. When failure occurred along the length PPV, this did not necessarily manifest at the manufactured seam existing in the PPV. Because the failure location, and PPV orientation was not consistently replicated, this random nature of failure in the PPVs affirms some of the previously stated weaknesses of this loading method. Without a consistent failure location, and charge orientation, it is reasonable to expect the pressure data collected would show asymmetry in shock propagation. Some general observations are now made regarding the pressure profiles for each of the three layouts utilized.

1. Linear Layout

A photograph of the linear layout used in this research is shown in Figure 51 where $R1 = 0.46$ m, $R2 = 0.3$ m, and $R3 = 0.15$ m. All sensors and the charge were submerged to the same half-depth of the AWT. A pressure profile time history utilizing a linear layout for the pressure sensors is shown, in Figure 52, with a total of four test runs being conducted. Maximum pressure values can easily be seen on the plot, where pressure sensor 3 was closest to the charge source and sensor 1 was furthest from the charge source. Similar shape was seen in each of the successive sensor pressure response over time, but with reduced magnitude and delayed rise and decay. Sensors 3, 2, 1 as expected had descending orders of maximum pressures recorded as the incident shock front arrived and diminished at each successive sensor.

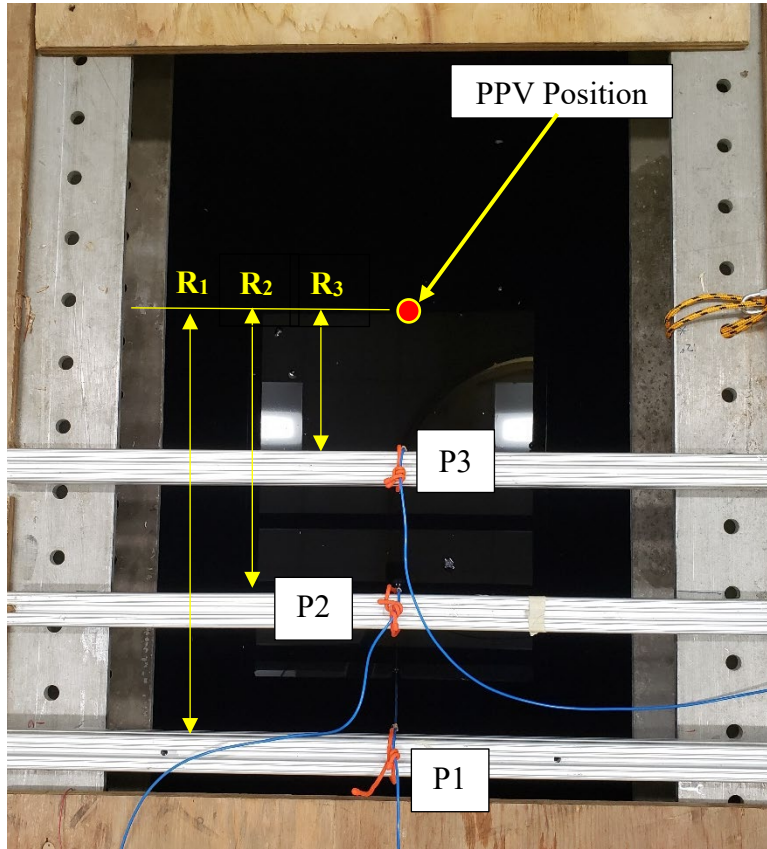


Figure 51. Linear pressure sensor layout. $R_1 = 0.46$ m, $R_2 = 0.3$ m, and $R_3 = 0.15$ m

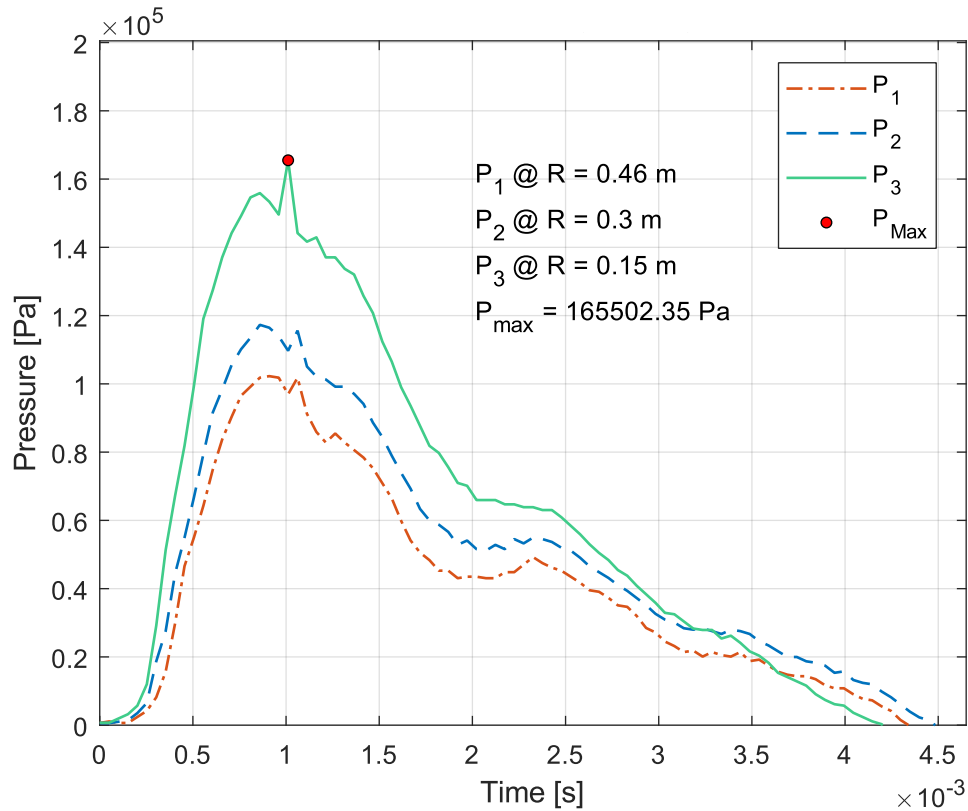


Figure 52. Pressure profile characterization, linear, R = 0.46 m, Run 1

In general, it is known that the shock front will travel radially away from the charge source. This means the exact radial distance from the charge was calculated for every single test run conducted to better understand the shock wave pressure front behavior over time and distance. Maximum pressures were pulled from pressure time history plots from the DAQ, resulting in 66 distinct maximum pressure data points. These results were plotted as a function of stand-off distance to better see the behavior and characteristics of the shock front using the LN2 loading method. Mean and standard deviation were calculated for the maximum pressure results at each stand-off distance, and these statistical trends were overlaid onto the pressure distribution plot seen in Figure 53 in yellow and red respectively.

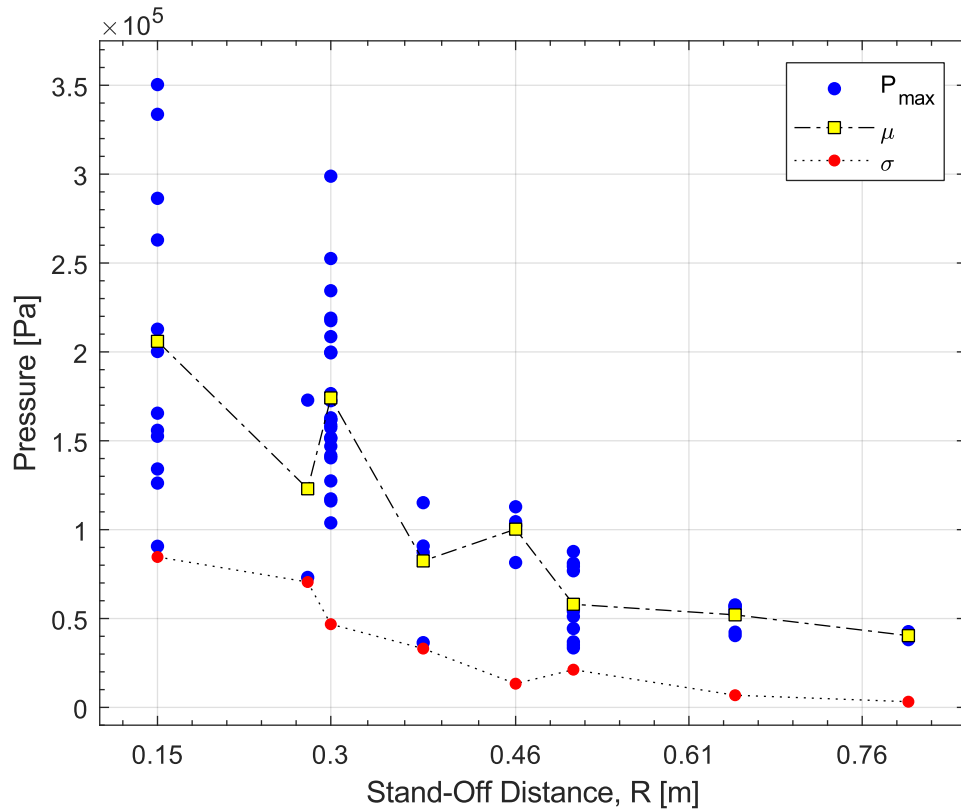


Figure 53. Maximum pressure distribution statistics

It can be seen in Figure 53, that the mean value for the maximum pressure at a given stand-off distance increased the closer the charge was to the target (composite test plate). Similarly, the standard deviation increased the closer the charge was to the target. This suggested the maximum pressures recorded, varied more widely as stand-off distance was decreased. Conversely, the further the charge was to the target and the sensor, the more symmetric and uniform the maximum pressure results became. This was the first data driven confirmation that directionality was present by the LN2 loading source. Generally, if directionality was minimal, i.e., the shock front propagated spherically, the spread of the data should not be influenced by the stand-off distance, R . An additional reason this spread of data may exist, was the difficulty to have precision in the volume of LN2 provided to the PPV prior to failure of the PPV and the shock loading propagated on the composite plate. A gram scale would help to better quantify how the change of the mass of LN2 used test to test, affected the loading across the composite plate. Standard deviation in Figure

53, might be influenced by this variation in LN2 mass, and not solely on the orientation of the PPV suspended in the water of AWT, and the location of failure in the PPV. Nevertheless, an exponential fit was conducted to see if an exponentially decaying behavior of this loading method was accurate to assume in comparison to conventional explosive shock pressure time history plots. The exponential fit plot is shown in Figure 54.

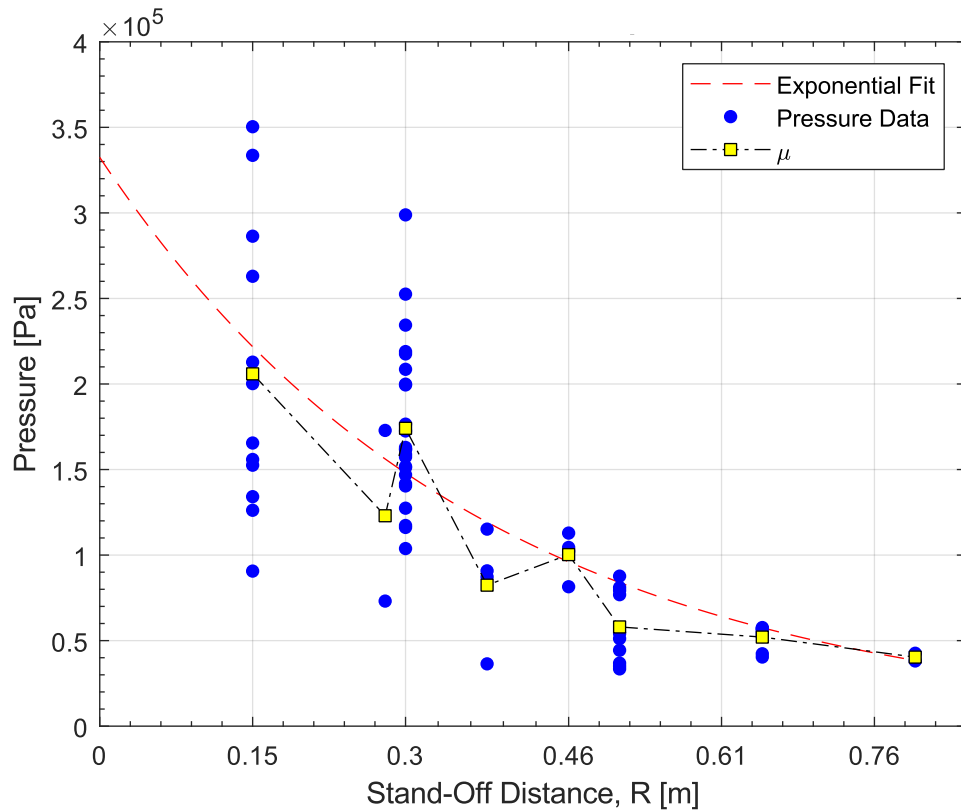


Figure 54. Exponential fit for maximum pressure profile

The oscillating nature of the mean maximum pressures affirmed an exponential plot fit was an accurate assumption for the characteristics of the LN2 shock pressure time history. By extrapolating the exponential fit curve backwards to a $R = 0$ m stand-off, an estimate of the maximum mean pressure at the charge source was determined to be 332.46 kPa (48.22 psi). A summary of the maximum pressure results for the radial propagation characteristics of the shock front using LN2 is provided in Table 3.

Table 3. Maximum pressure results summary as function of R

Stand-off, R (m)	Data Points, N	μ		σ		Pressure Ratio
0.15	12	205934.69	Pa	84626.08	kPa	0.62
		29.87	psi	12.27	psi	
0.28	2	122980.87	Pa	70533.65	kPa	0.37
		17.84	psi	10.23	psi	
0.3	24	174095.87	Pa	46791.27	kPa	0.52
		25.25	psi	6.79	psi	
0.38	4	82402.11	Pa	33075.28	kPa	0.25
		11.95	psi	4.80	psi	
0.46	4	100268.52	Pa	13324.12	kPa	0.30
		14.54	psi	1.93	psi	
0.51	10	57999.43	Pa	21204.87	kPa	0.17
		8.41	psi	3.08	psi	
0.65	8	52056.96	Pa	6836.75	kPa	0.16
		7.55	psi	0.99	psi	
0.8	2	40355.03	Pa	3191.66	kPa	0.12
		5.85	psi	0.46	psi	

Bins for the data results in Table 3 were created for each stand-off distance tested shown in Column 2. Column 2 of Table 3 shows the number of data points collected for that bin. The last column in Table 3 shows the pressure ratio of the maximum mean pressure at each stand-off distance away from the composite plate to the maximum mean pressure at R = 0 m, extrapolated from Figure 54. Smaller bin sizes in column 2 of Table 3, were a result of the radial component of the stand-off distance being slightly larger than the nominal perpendicular stand-off distance measured for each linear and standard layout for testing. For ease of experimental set-up, stand-off distance was measured as the perpendicular distance between the charge and the composite plate fixed to the box of the CTR. Since pressures sensors 1 and 2 were set in parallel as shown in Figure 45 (a), the precise distance from charge to pressure sensor, was larger radially than the nominal distance established between the charge and the composite plate. To better understand the potential influence of directionality in the loading and response of the structure, an analysis of the triangular layout was performed.

2. Triangular Layout

A photograph of the triangular layout used in this research is shown in Figure 55. All sensors were placed 0.3 m (12in) from the charge source and remained equidistant from one another forming an equilateral triangle about the charge source seen in Figure 55.

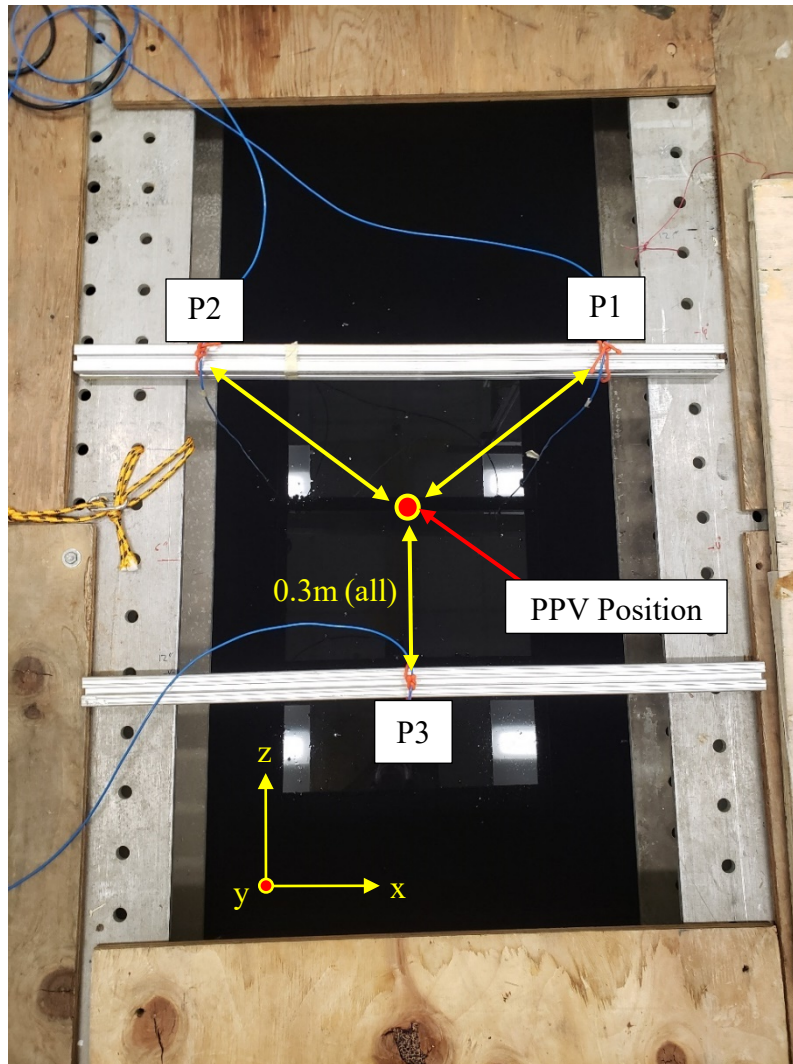


Figure 55. Triangular pressure sensor layout and PPV positioning, $R = 0.3$ m

The pressure time profile for the first triangular run conducted of five total runs is provided in Figure 56. For four of the five triangular layout test runs, pressure sensor 2, P2, exhibited higher pressures than sensors 1 and 3. Other than previous mentioned sources

of the directionality of the loading source, one additional contributor was investigated. Differences in sensitivity sensor to sensor were identified through the manufacturer's calibration sheets provided. However, sensitivity of sensors 2 and 3 are close to one another at 742.2 mV/MPa and 747.2 mV/MPa respectively, meaning if symmetric loading was occurring across all three pressure sensors, we would expect each run to look closer the results of Run 5 in magenta in Figure 57. Instead, the trend of our results were more triangular in nature, instead of having a slope closer to zero across all three sensors which would indicate symmetry of loading. If the bottle physically tended to be slightly closer to sensor 2 for most test-runs, it was sensible that the maximum pressures recorded at 1 and 3 were lower. Maximum pressures data points for sensors 1 and 2 in Figure 57 appear to be equidistantly spaced. Sensor 2 magnitudes were higher than sensor 1 overall. Maximum pressures recorded in this triangular layout for sensor 3, showed more precise results across all runs in Figure 57, with less spread between each neighboring data point than that observed in sensors 1 and 2.

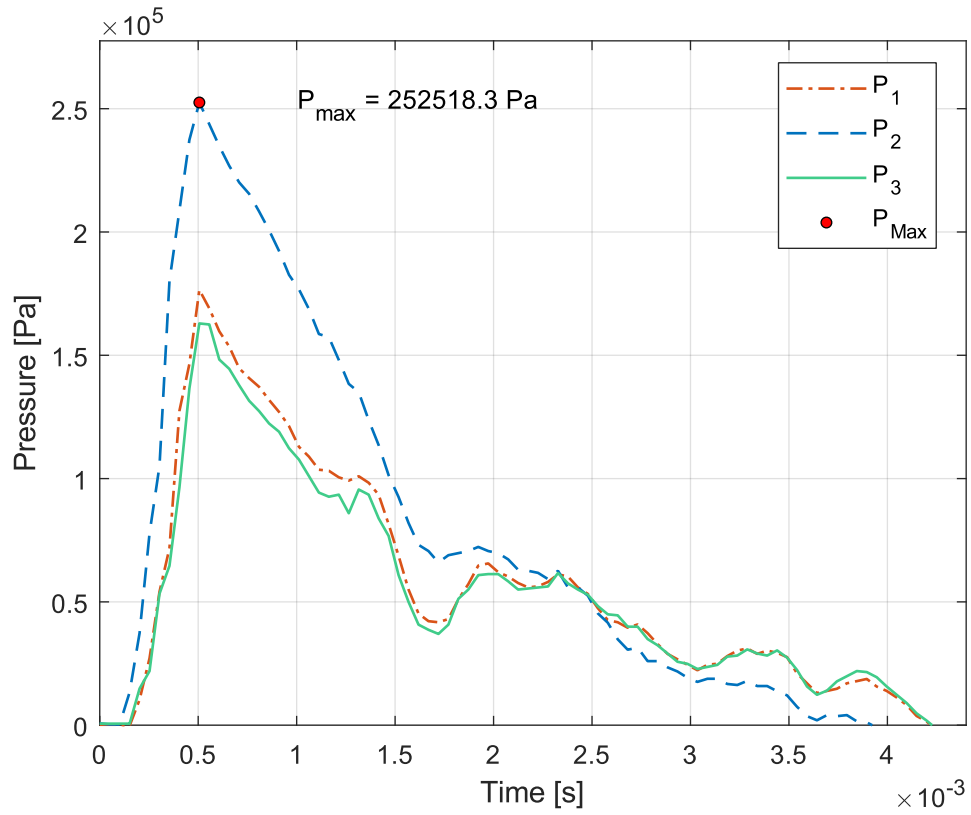


Figure 56. Pressure characterization, triangular results, R = 0.3 m, Run 1

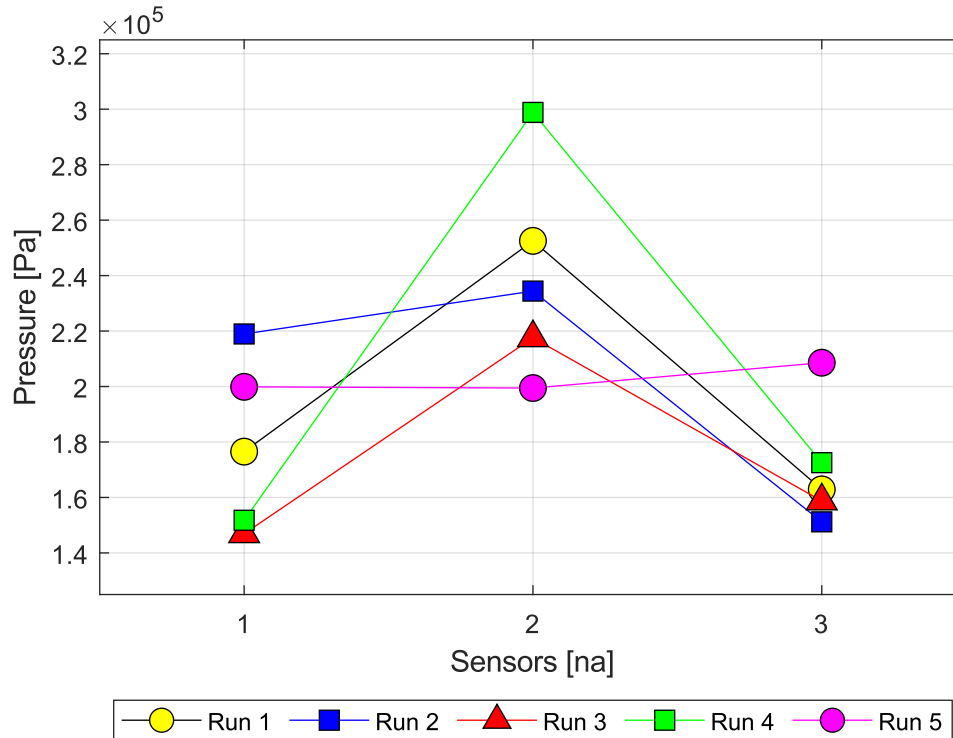


Figure 57. Directionality analysis, triangular results summary, R = 0.3 m

3. Standard Layout

The standard pressure sensor layout used for every strain DAQ run is shown in Figure 58. Pressure sensors 1 and 2 stayed in the same location for all DAQ in this research. Pressure sensor 3, changed stand-off distances from the charge, never being closer than 0.15 m from the charge source. Pressure profiles and plate loadings are only included for the failure test run for each respective plate, and the preceding pressure profile and plate loading plot results are included in Appendix D.

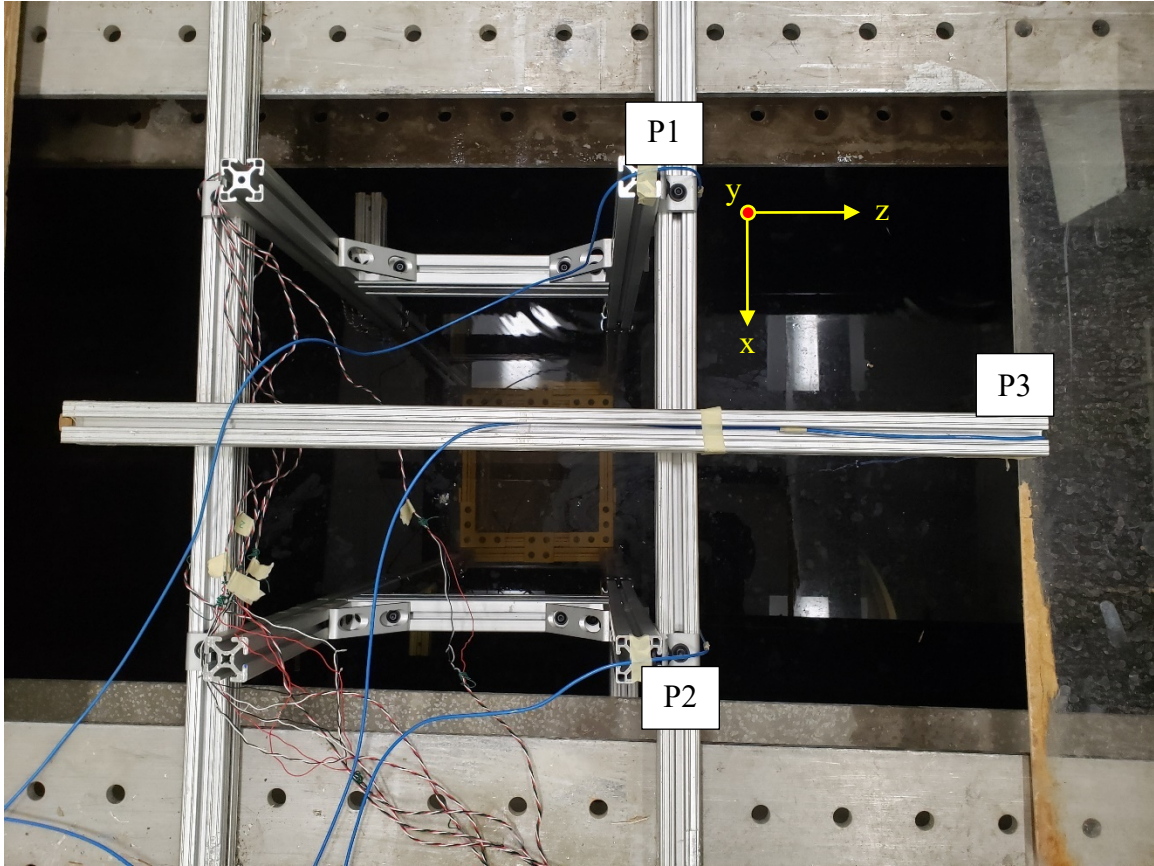


Figure 58. Standard pressure sensor layout for strain DAQ

B. STRAIN RESULTS

As summarized in Table 2, four different fiber orientations were evaluated in this research for their strain response to different shock loadings at varying stand-off distances in a marine environment. A four-layer plate, Sample 8, was first used to establish a system baseline and ensured proper functionality of all portions of the DAQ prior to collecting strain data for in-depth analysis. Wires on Sample 8 were damaged during the lowering process for one test run, leaving bare wire exposed to the water environment. This damage resulted in Sample 8 being removed from the test matrix in Table 2. Additionally, the four-layer Sample 5 was not tested due to the time constraints of this research.

Each plate orientation had two separate samples tested with contrasting backing conditions of AB and WB at varying stand-off distances until failure. Strain data was collected across three nodes in the order shown in the Figure 59. In Figure 59, Pressure

gage 1, P1, corresponds to the loading applied near Strain gage 1, S1. Likewise, Pressure gage 3, P3 corresponds to the pressure loading applied at Strain gage 3. By taking the average of these loading values recorded at Strain gage 1 and Strain gage 3, the loading at Strain gage 2 was determined.

Each plate was tested at an initial stand-off distance, and if failure did not occur the charge source was moved closer to the CTR in increments of 0.15 m (6 in). Submersible lights with sufficient illumination were used to assess the integrity of plates prior to continuing a test run at a closer stand-off distance for both the AB and WB testing. Damage to the sample plates was immediately obvious for the AB plates due to the rapid outflow of bubbles that vented continuously from the box of the CTR to the surface of the water in the AWT. Plexiglass windows on four faces of the box provided excellent visual verification of a maintained AB condition and helped to identify damage to the plate without having to completely remove the CTR from the AWT. An insignificant amount of water, less than 2.54 cm (1 in), was estimated to accumulate through the small gaps between the wires and the orifice in the back plate of the box during AB testing. For all AB testing, water level was positively verified to be well below the edge of the composite plate. This ensured proper backing condition was maintained for the duration of the testing for each AB plate. For consistency across all testing, the weak direction of every composite plate tested was consistently aligned with the y-axis when fixed to the box of the CTR as seen in Figure 59.

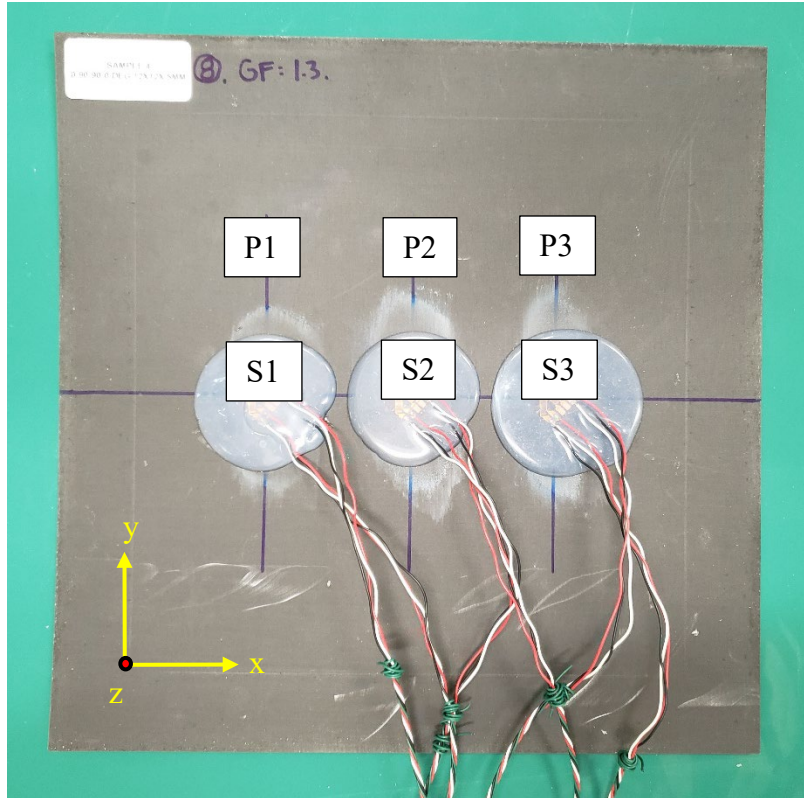


Figure 59. Strain gage numbering sequence, and pressure correlation

After the composite plate failed, regardless of fiber orientation, a visual inspection of the test plates was conducted, pictures were taken of the failure regions and, and failure characterization was completed. Once failure characterization was completed, the data collected for strain and pressure was analyzed through MATLAB[®] code to plot strain response for tension and compression as a function of time for all x and y nodes to be plotted and analyzed. Only the failure strain response time histories are included in this chapter of the thesis. All preceding strain response time history plots are included in Appendix C.

1. Uni-directional Composite (0°)

Two unidirectional composite plates were tested in AB and WB. Both plates failed at the same initial stand-off distance of 0.46m (18in). Failure along the x-axis could be seen clearly in AB Sample 1 plate tested unto failure in Figure 60. Failure location was along

the bottom clamped boundary of composite plate as well as just below the center of the plate shown in yellow boxes in Figure 60.

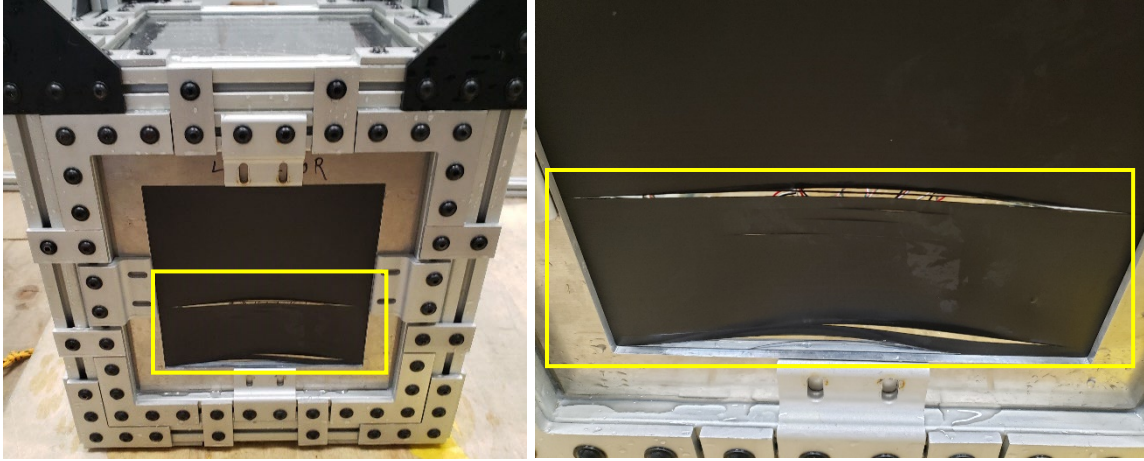


Figure 60. Failure of AB Sample 1, unidirectional carbon composite plate, $R = 0.46$ m

Once Sample 1 was removed from the box, looking at the plate from the back, it was observed in Figure 61, that an additional failure region exists at the top boundary for the plate. The plate was broken completely into four separate pieces with fiber separation as seen in Figure 61.

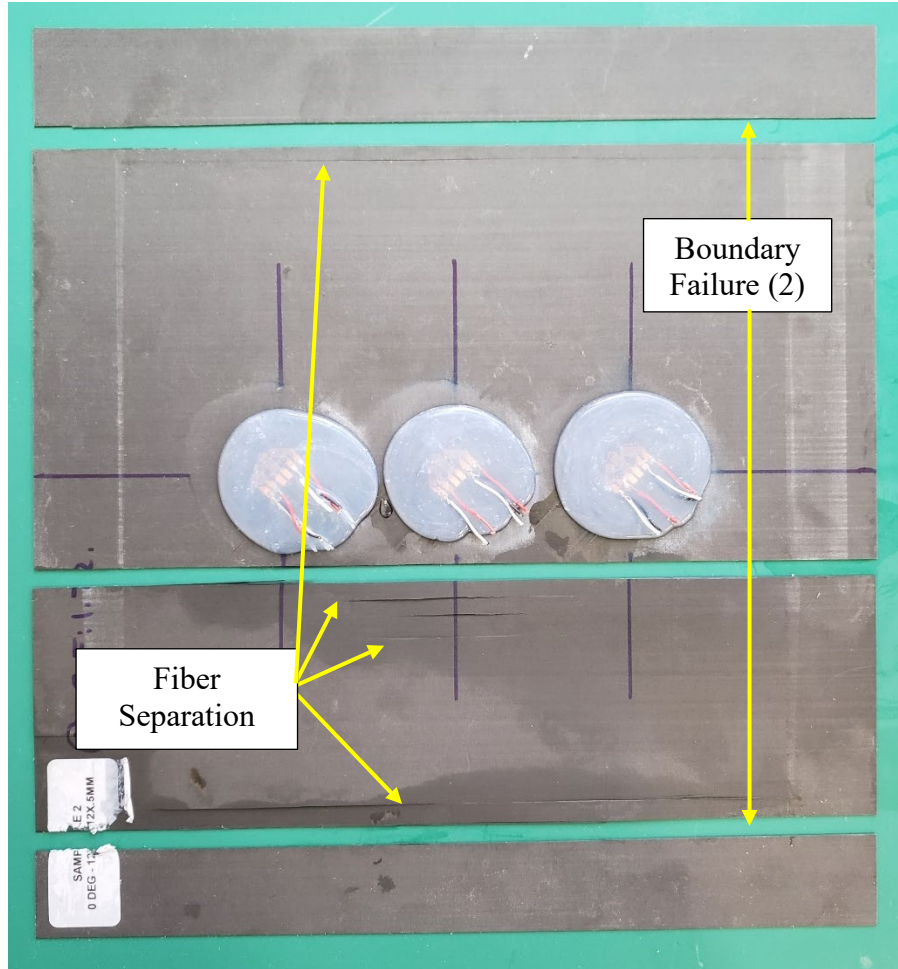


Figure 61. Back side of AB Sample 1, failure characterization, $R = 0.46$ m

Sample 2 was tested in a WB condition and the initial failure imagery can be seen in Figure 62. Inward concavity of the failed WB plate was seen in the right portion of Figure 62. Several failure lines in the x-direction were clearly seen as well. More fiber separation in the plate overall was observed in WB Sample 2 than AB Sample 1.

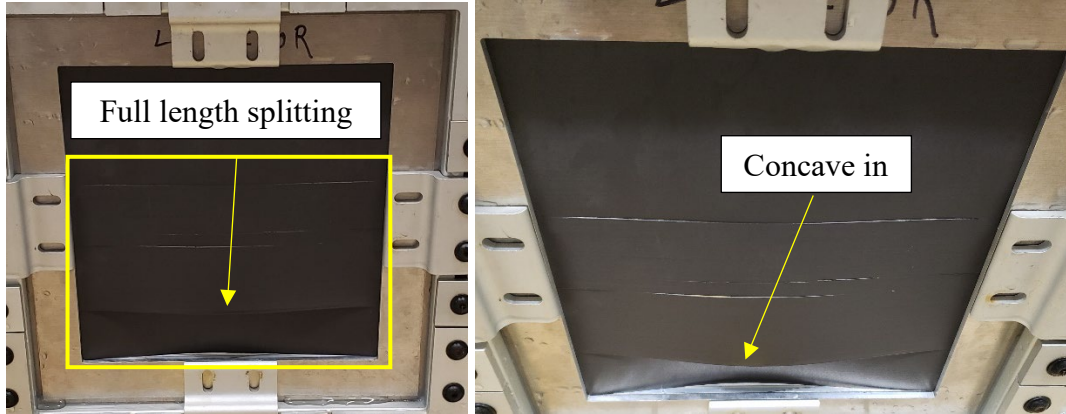


Figure 62. Failure of WB Sample 2, unidirectional carbon composite plate, $R = 0.46$ m

WB Sample 2 was broken into three distinct sections compared to four sections in the AB case. However, prior to removing WB Sample 2 from the CTR, five full length fiber splits were observed in Figure 62, compared to three in Figure 60 of AB Sample 1. Boundary failure for WB Sample 2 only occurred in the bottom boundary at the window compared to the top and bottom boundary failure of AB Sample 1.

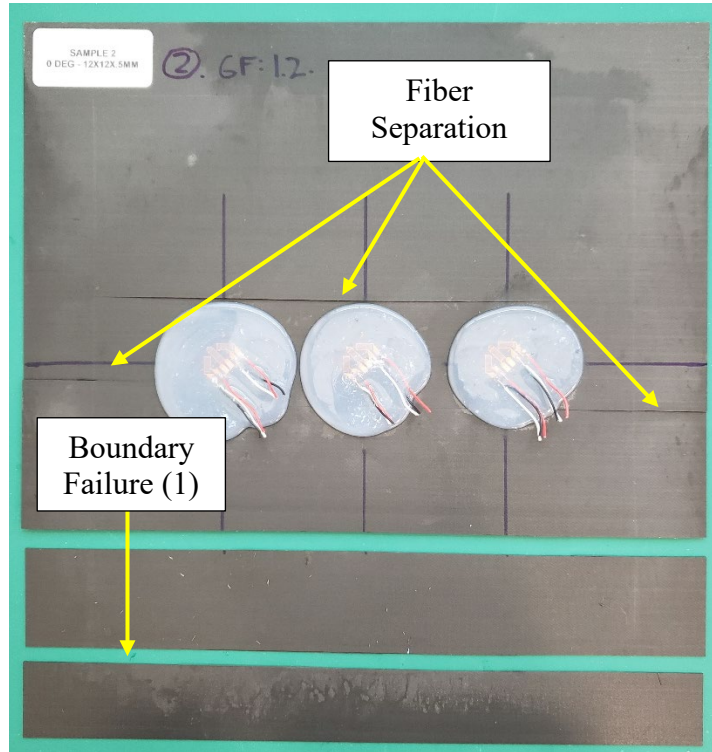


Figure 63. Back side of WB Sample 2, failure characterization, $R = 0.46$ m

Pressure profiles and plate loading for the failure run of AB Sample 1 and WB Sample 2 is provided in Figure 64. Average loading across the plate at failure was recorded as 34.28 kPa.

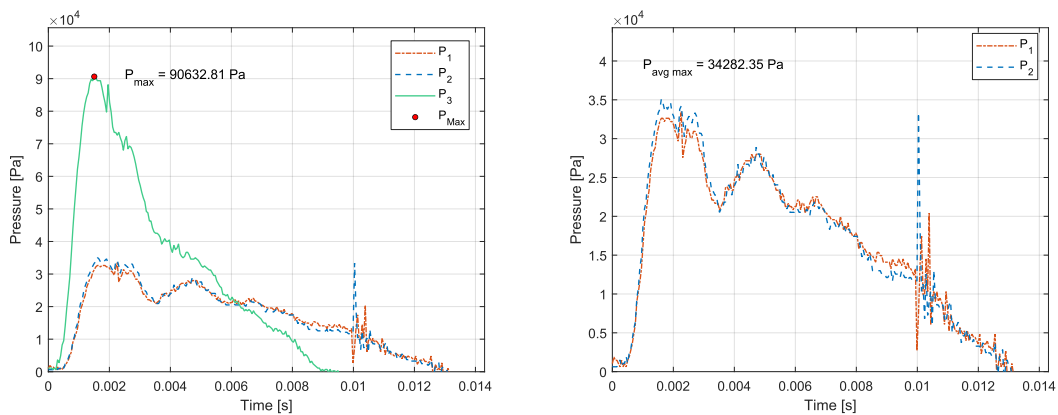


Figure 64. Overall pressure profile (left), plate failure loading (right), AB Sample 1, $R = 0.46$ m

The shorter and more rounded pressure profile of the plate loading in Figure 65 was accurate for a lower energy shock front experienced by the structure further from the LN2 charge center. P3 pressure time history showed near instantaneous rise and decay on the order of milliseconds, as it was positioned closest to the charge. The spikes shown in the plate loading plots for the AB Sample 1 may be indicative of a reflected pressure wave due to the impedance mismatch of the water and air. A reloading of the sensors occurred as the reflected incident wave moved away from the plate. This behavior was not expected in the plate loading plotted results of WB Sample 2.

Pressure profiles and plate loading for the failure run of WB Sample 2 is provided in Figure 65. Average loading across the plate at failure was recorded as 47.77 kPa.

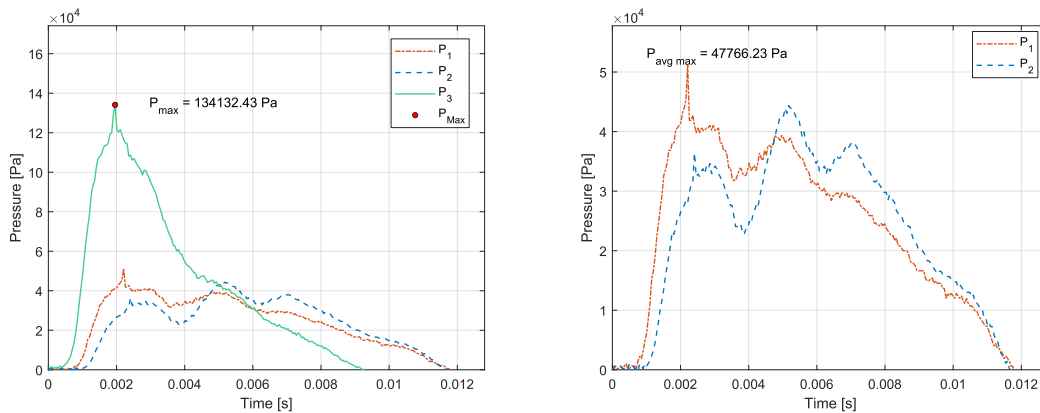


Figure 65. Overall pressure profile (left), plate failure loading (right), WB Sample 2, R = 0.46 m

Plate loading experienced at failure by WB Sample 2 was 13.48 kPa (1.96 psi) greater than the failure loading experienced by AB Sample 1. This loading pressure difference was negligible, and so the difference in response and failure of both plates could be compared accurately. For the time history plate loading of WB Sample 2, there was no spike in pressure as expected since the pressure wave is free to propagate through the composite plate and into the unrestricted flow boundary of the back of the box. Similarity in loading magnitudes at the plate, provided more precise comparison of strain response in the strain time history plots to follow.

Unidirectional strain response results for AB Sample 1 and WB Sample 2 were discovered to be inaccurately exaggerated due to incorrect V_{EX} and R_L values inputted to the NI suite prior to data collection. Consequently, the magnitude of strain response in their time history plots could not be accurately compared to one another or to other fiber orientation plate results. However, overall observations of the strain time history plots could be made between the AB and WB samples that are unrelated to magnitude of the response. This was especially true since the actual loading applied to both composites plates was nearly identical. These inconsistencies were corrected, and strain magnitudes measured for all future composite plate samples tested, accurately reflected their strain response. Strain response as a function of time is shown in Figures 66 and 67. To better analyze and compare the strain responses for both unidirectional plates, strains for x and y directions of all three nodes was divided by the absolute value of the maximum strain recorded over the time window observed. These nondimensional results are shown in Figures 68 and 69.

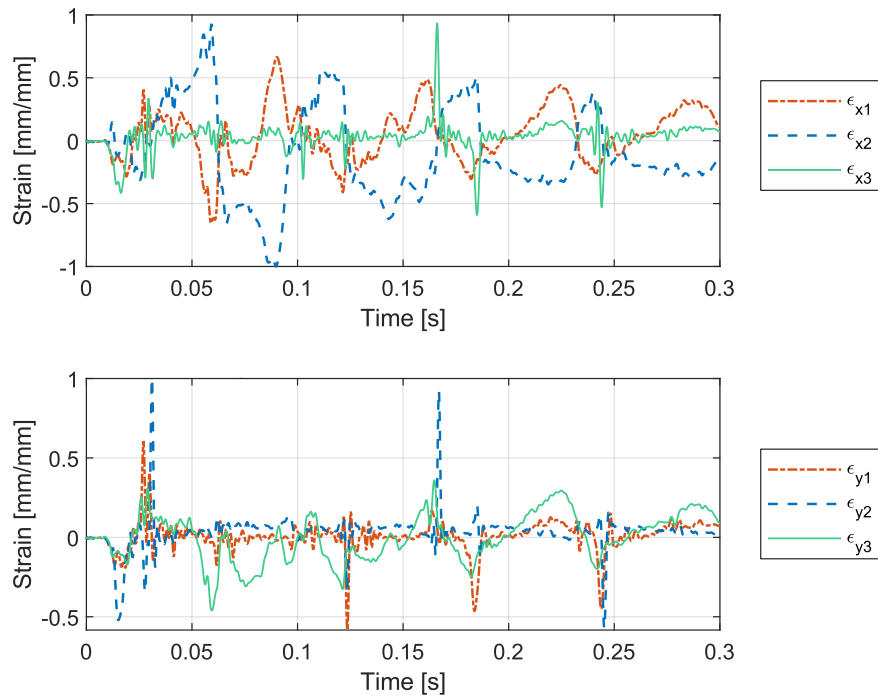


Figure 66. Strain response, AB Sample 1 (0°), $R = 0.46$ m, failure run

For the x-direction strains for AB Sample 1 in Figure 66, all nodes were out of phase of one another, and nodes 1 and 2 were roughly 180° out of phase of each another. Strain response of nodes 1 and 2 in the x-direction showed a gentler sinusoidal oscillation, whereas node 3 in the x-direction was marked by periods of 0 strain followed by alternating spikes of tensile and compressive strain. In the y-direction periods of large tensile and compressive strains was seen in nodes 1 and 2 followed by 0 strain. Node 3 in the y-direction exhibited more gently oscillating strain response, like that seen in nodes 1 and 2 in the x-direction, but strain in node 3 changed at a much higher frequency. Arrival of maximum strain in the x and y-directions for the AB Sample 1 plate were approximately $t = 0.08$ and 0.025 seconds respectively.

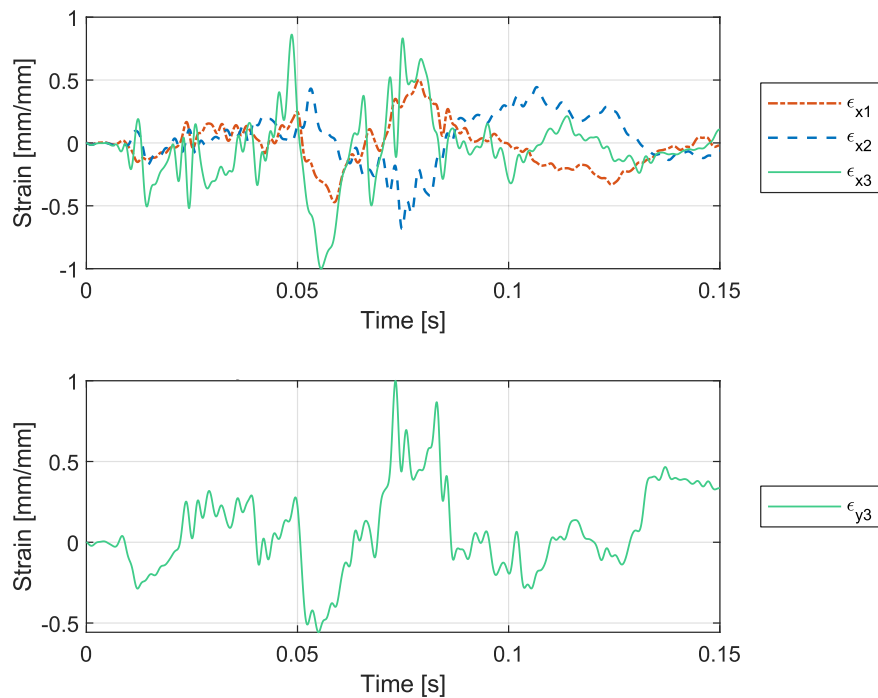


Figure 67. Strain response, WB Sample 2 (0°), R = 0.46 m, failure run

Strain response for WB Sample 2, showed no phase pattern for the x or y-direction nodes. All nodes for both x and y-direction strains displayed a gentler sinusoidal oscillation, similar to the x-direction nodes 1 and 2 of AB Sample 1. Arrival of maximum

strain in the x and y-directions for the WB Sample 2 plate were approximately 0.06 and 0.075 seconds respectively.

Nodes 1 and 2 for y-direction strain for WB Sample 2 in Figure 67 were not available for analysis. One reason the data for these nodes was not usable was that the CTR physically moved at the moment the shock front arrived at the box. The movement of the CTR caused two of the wires leads at the alligator clip connections to touch, thereby shorting the circuit for these nodes. A single rail was added on top of the strain gage leads from the composite plate to reduce the movement of alligator clips when the shock front hit the CTR. However, this experimental set-up adjustment was not perfect in preventing all future shorting the strain node circuits. Additionally, in future strain response time plots, it is believed at higher failure loadings that debonding of the strain gages to the test specimen occurred resulting in a similar step function response of those affected nodes. In either case, any strain response time history plot with nodes missing, was attributed to one of these factors.

2. Three-layer Composite (0-90-0°)

Two three-layer composite plates were tested in AB and WB condition. Failure for the three-layer plates, WB Sample 3 and AB Sample 4, occurred at stand-off distances of 0.46 m and 0.76 m respectively. Sample 3 testing started at 0.61 m (24 in) and failed after the first stand-off distance decrease of 0.15 m (6 in) at a final failure stand-off distance of 0.46 m (18 in). The known stand-off distances for failure of both unidirectional plates, informed a further initial stand-off distance 0.76 m (30 in) for AB Sample 4. This choice was made to provide more data points for strain response prior to plate failure. Nevertheless, the AB Sample 4 failed at this initial stand-off of 0.76 m. This meant the unidirectional plate stand-off distances should have started further than 0.76 m if both three-layer plates failed at the same or greater stand-offs than the AB and WB unidirectional plates. Additionally, Table 2 shows the thicknesses of the three-layer plates was less than that of all the other carbon fiber plates tested. This indicated a missing layer of material in the three-layer plates which further reduced its ability to resist bending stress.

Nevertheless, failure was observed at a stand-off of at least 0.46 m and 0.76 m respectively for the WB and AB three-layer plates.

Plate failure characteristics are shown in Figure 68. Localized and concentrated failure was seen in the yellow circle in the bottom image of Figure 68 near the boundary but not on the boundary. Unusually, WB Sample 3 was the only composite plate to have a concaved-out shape in the bottom 3rd of the plate after failure indicated in Figure 68 by the yellow box. If the gas bubble from the charge expanded far enough within close proximity to the test plate, the pressure at the front of the plate could have been reduced below hydrostatic pressure. This may have allowed the water back fluid medium against the back of the test plate to push it further out of plane away from the box to its final failure position seen in Figure 68.

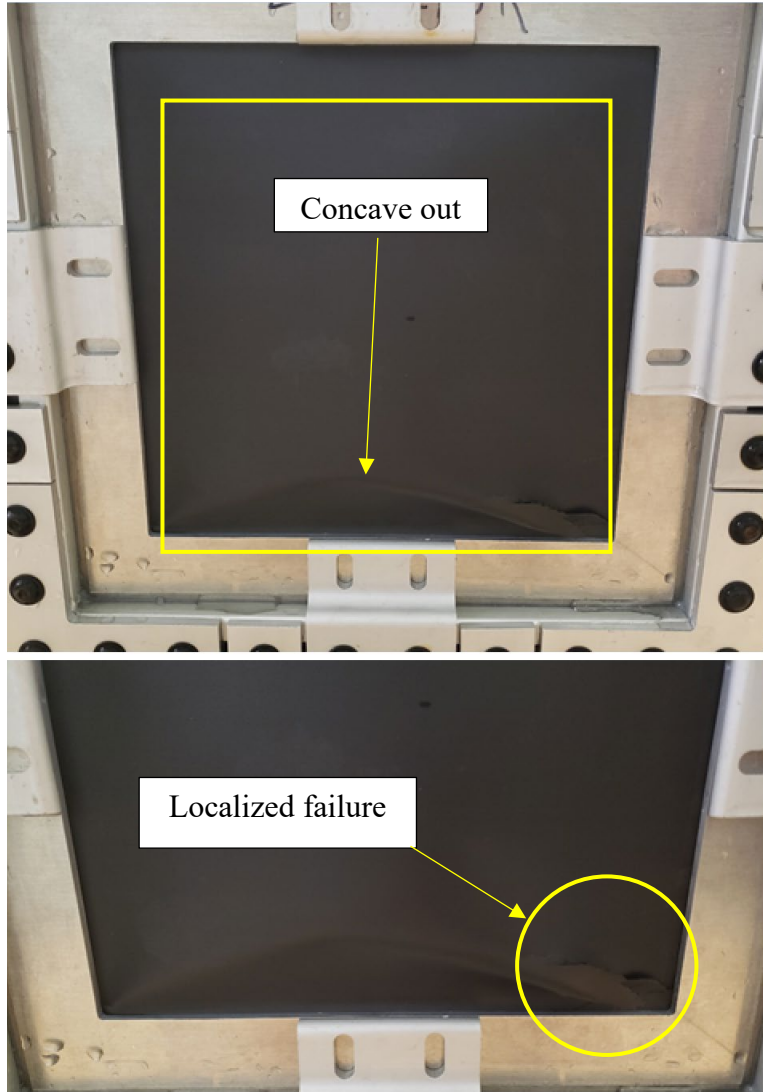


Figure 68. Front failure characteristics of WB Sample 3, $R = 0.46$ m

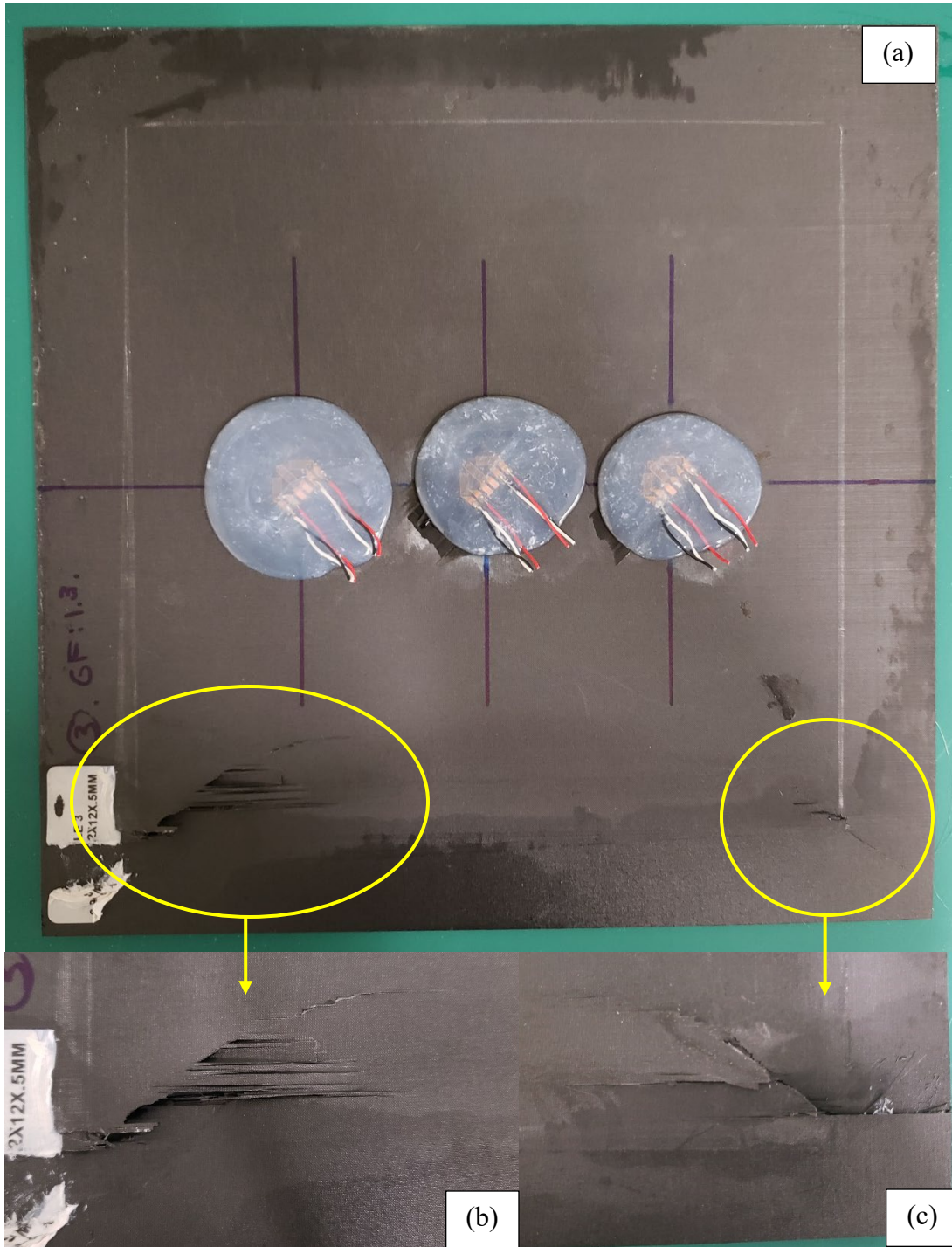


Figure 69. WB Sample 3, failure characterization, $R = 0.46$ m: (a) back side, (b) zoomed local failure back side, (c) local failure at corner on front of plate

Delamination was observed in the corner of WB Sample 3 on the back of the composite plate, as well as a diagonally propagating fiber crack in the zoomed in Figure 69 (b). Additionally, Figure 69 (c) showed more delamination and additional severe fiber fracture in a diagonal line at the front left corner of WB Sample 3. Horizontal failure at the clamped boundary in this corner could also be seen where complete fiber separation is occurred. Bottom left and right of the plate are the only two regions of macro material failure observed in WB Sample 3.

A back view of the AB Sample 4 is shown in Figure 70 with the composite plate still attached to the box of the CTR. At failure, the composite plate was left in a concave-in position as seen by the curve in the top and frayed edge of AB Sample 4 in Figure 70. Yellow outlined regions indicated plate failure regions. Failure in AB Sample 4 was more distributed across the top of the plate boundary than the localized failure observed at the bottom of the WB Sample 3 seen in Figure 69.

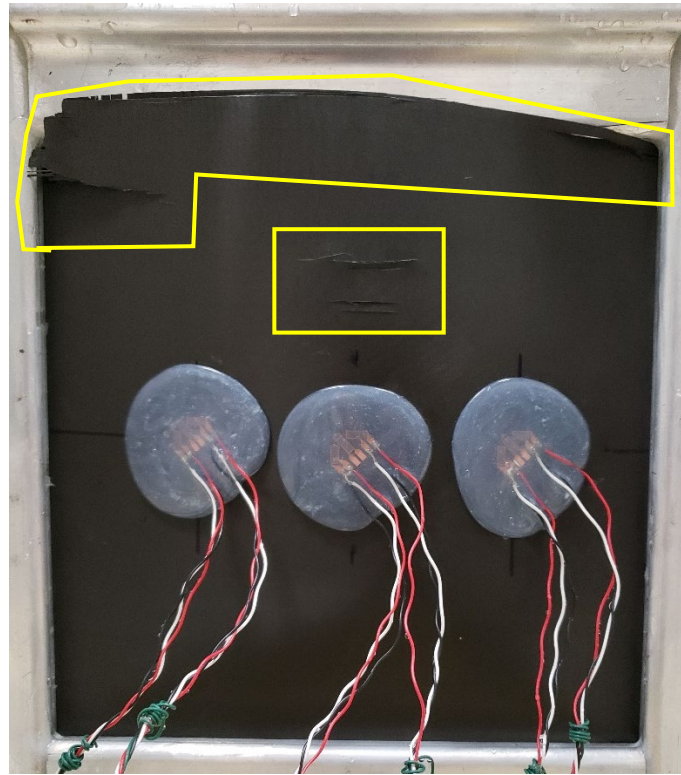


Figure 70. Back failure characteristics of AB Sample 4, $R = 0.76$ m

Complete separation of AB Sample 4 was observed in Figure 71 at the top clamped boundary. Further fiber cracking and delamination could be seen in the top right corner propagating from the boundary into the main body of the plate. A small area of fiber separation was seen in the small yellow square just above the strain gage placement in Figure 71.

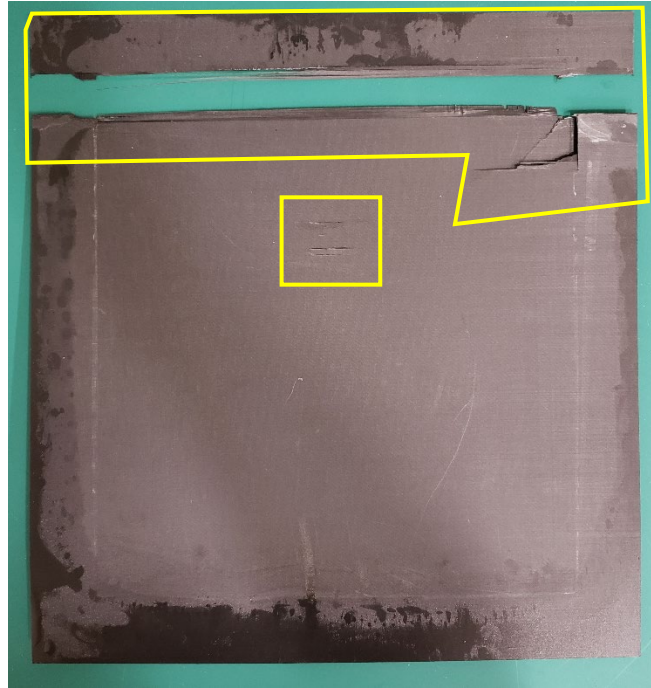


Figure 71. Front failure characteristics of AB Sample 4, $R = 0.76$ m

Pressure time profiles and plate loading pressures for the failure run of WB Sample 3 and AB Sample 4 is provided in Figure 72 and 73. Average loading across the plates at failure was recorded as 82.27 kPa and 40.36 kPa respectively for WB Sample 3 and AB Sample 4. Therefore, the failure loading required for WB compared to that of AB was just over two-times the loading magnitude across the composite plate. Since the loading experienced by AB Sample 4 was sufficient to induce failure, it is likely the AB plate would have failed at a further stand-off distance.

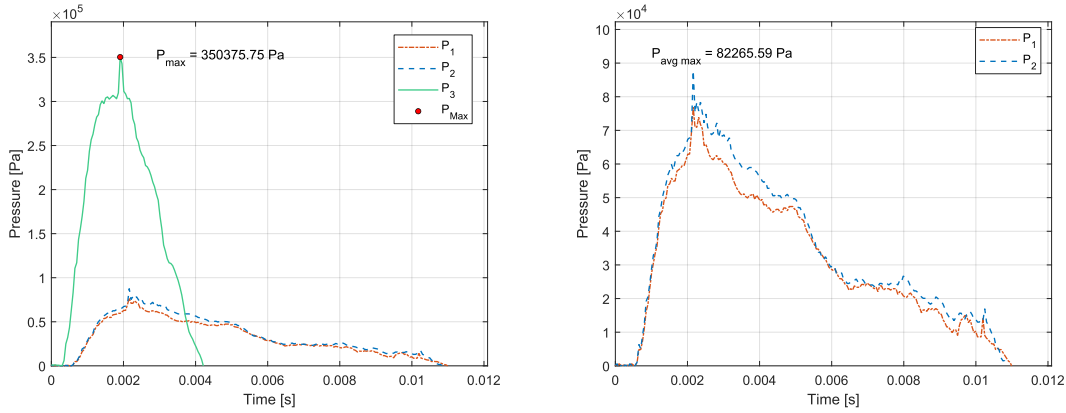


Figure 72. Overall pressure profile (left), plate failure loading (right), WB Sample 3, R = 0.46 m

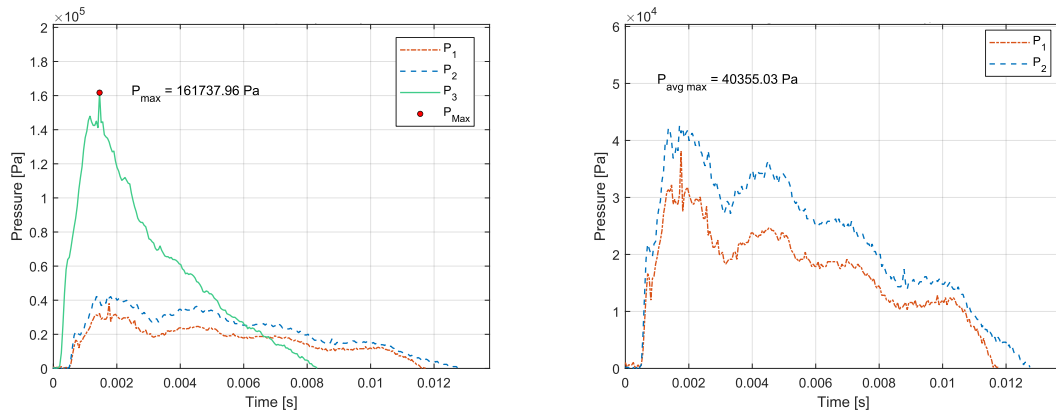


Figure 73. Overall pressure profile (left), plate failure loading (right), AB Sample 4, R = 0.76 m

Strain time histories for both three-layer plates at their failure runs are shown in Figures 74 and 75. For WB Sample 3, the x-direction strains had a slow oscillating sinusoidal behavior, whereas the y-strains showed periods of 0 strain followed by large strain increases in the tensile and compressive directions. Neither principal directions for strain in this sample showed strain response of the nodes changing in-phase or in some recognizable pattern. The strain spike in the x-direction for node 2 around $t = 0.12$ seconds, was likely related to the large concave out shape observed in Figure 68. Arrival of maximum strain in the x and y-directions for the WB Sample 3 plate were approximately 0.12 and 0.075 seconds respectively.

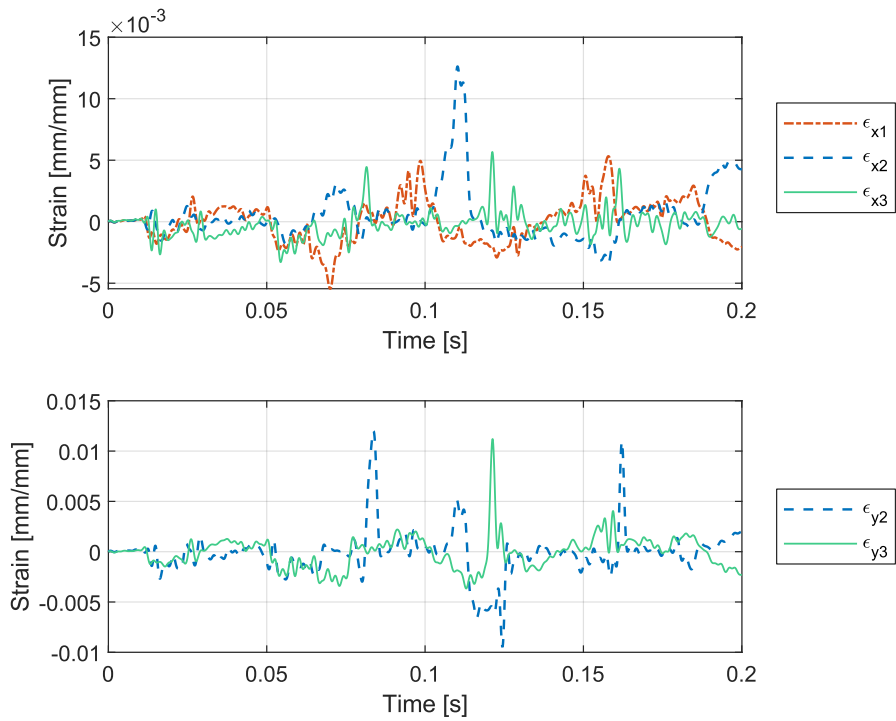


Figure 74. Strain response, WB Sample 3 (0-90-0°), R = 0.46 m, failure run

AB Sample 4 strain time response plots in Figure 75 show a similar 180° out-of-phase response for the nodes 1 and 2 in the x-direction that was observed in the unidirectional AB Sample 1. The x-direction strain response had a lower frequency behavior, and the y-direction strain response had a higher frequency behavior. Arrival of maximum strain in the x and y-directions for the AB Sample 4 plate were approximately 0.12 and 0.16 seconds for each principal direction respectively.

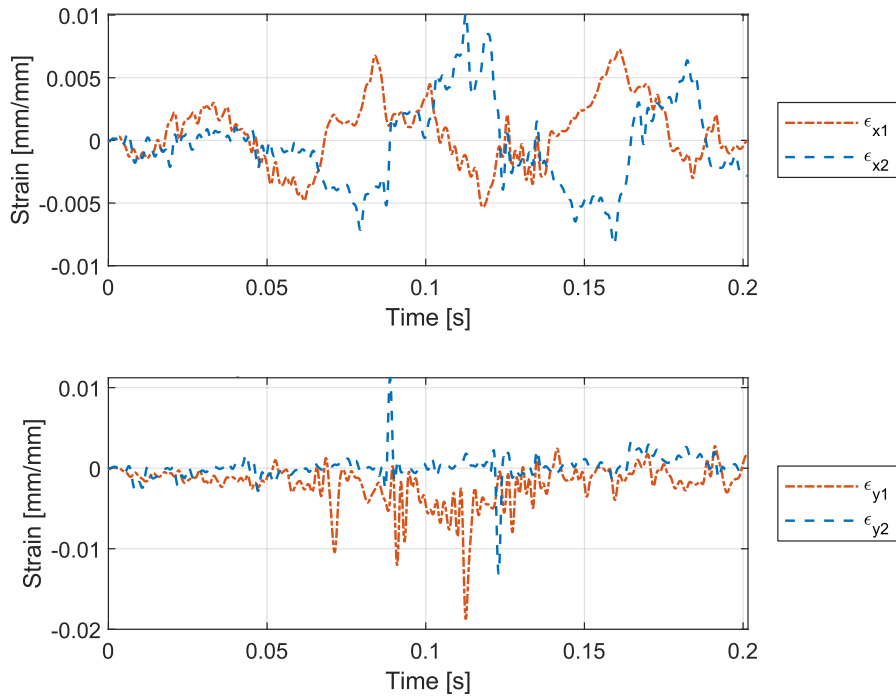


Figure 75. Strain response, AB Sample 4 (0-90-0°), R = 0.76 m, failure run

From each strain response time history plot, the maximum tensile and compressive strains were compiled for the x and y directions and then divided by the maximum pressure measured at each strain node. This was to remove the effect of the magnitude difference between the loadings during each test run, allowing evaluation of strain response per unit pressure. These maximum strain results divided by maximum nodal pressure were plotted for contrasting backing conditions for the three-layer plates tested. These results are seen in Figure 76 and 77, while the raw maximum strain results as a function of stand-off distance are included in Appendix C.

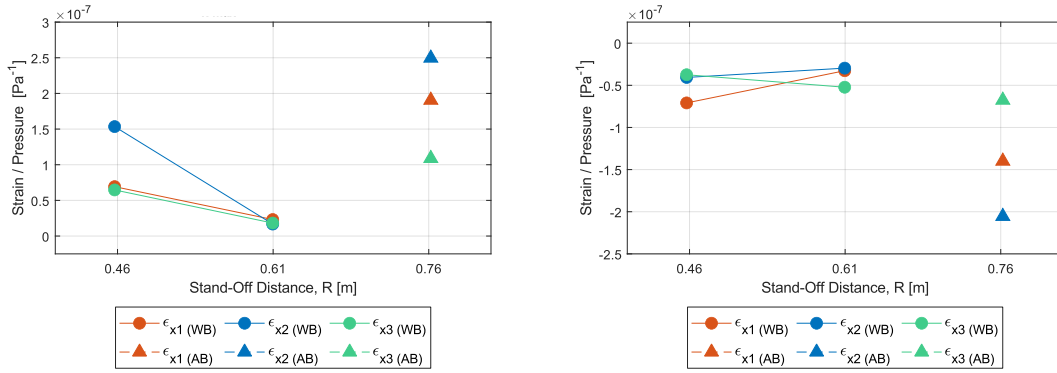


Figure 76. Normalized WB and AB max x-strain result comparison until failure (0-90-0): (left) tension, (right) compression

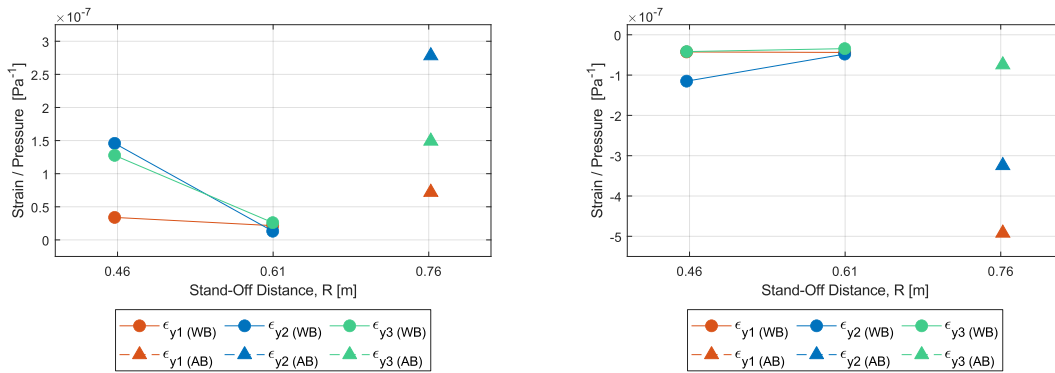


Figure 77. Normalized WB and AB max y-strain result comparison until failure (0-90-0): (left) tension, (right) compression

WB results are represented by circles, and AB results are represented by triangles. There were two important observations of these plots made. First, largest maximum strain occurred in the AB condition compared to the WB. Second, the data points for the AB maximum strains tended to be more spread apart, while the data points for the WB maximum strains tended to be more on top of one another for each stand-off distance. Further research is required to be able to explain how this might correlate to the localized and global/uniform failure visually observed in the WB and AB three-layer plates tested. More test runs would also be needed to better examine the trends of the maximum strain

for these plates at several stand-off distance further away from the composite plate until failure.

3. Four-layer Composite (0-90-90-0°)

Two four-layer composite plates were tested in the AB and WB condition. Failure for the four-layer plates, WB Sample 6 and AB Sample 7, occurred at stand-off distances of 0.15 m and 0.3 m respectively. Sample 6 testing started at 0.61 m (24 in) and failed after the third stand-off distance decrease of 0.15 m (6 in) at a final failure stand-off distance of 0.15 m (6 in). Sample 6 was also tested twice at the furthest stand-off distance of 0.61 m for DAQ setting verification. This additional run and time in the water for WB Sample 6 was assumed to be negligible in its effect on the final failure conditions of the test plate.

Plate failure characteristics for WB Sample 6 are shown in Figure 78. WB Sample 6 was concave-in at failure. Failure was localized again in the bottom right front corner of this composite plate similar to that observed in WB Sample 3. Severe delamination was seen in Figure 78, as well as some fiber fracturing away from the boundary and along the boundary. Diagonal fiber cracking can be seen in Figure 79 (b).

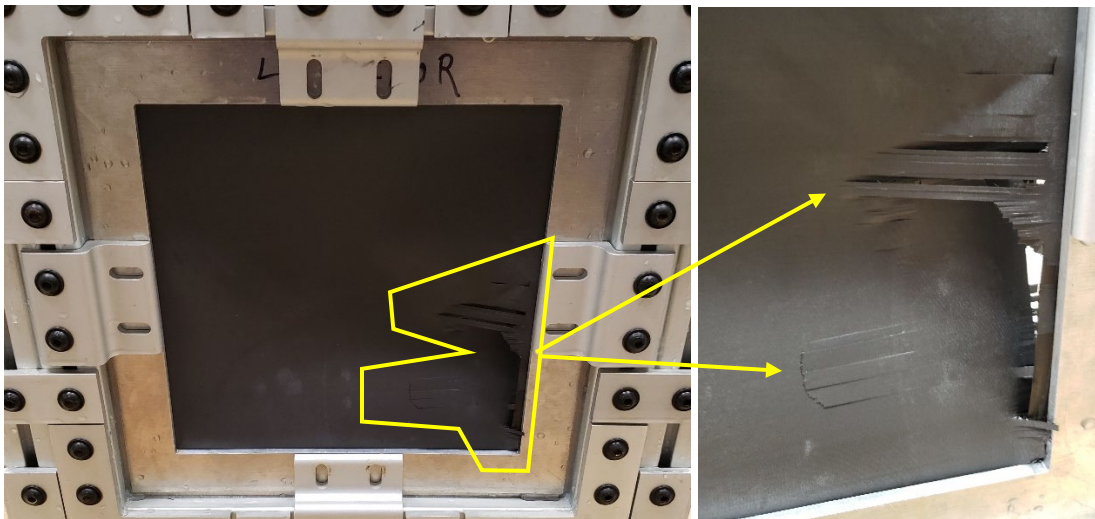


Figure 78. Failure of WB Sample 6, four-layer carbon composite plate, R = 0.15 m

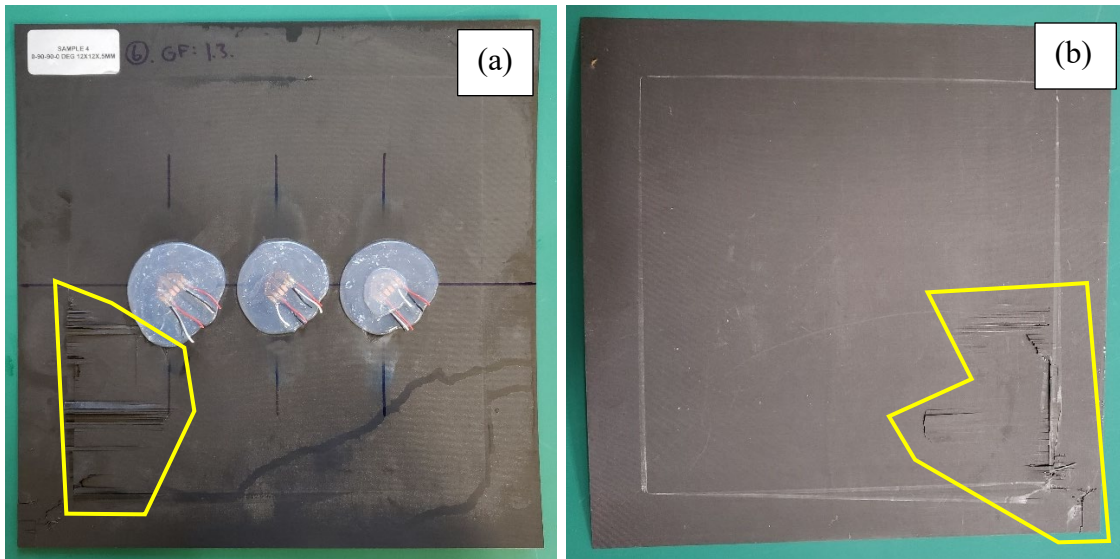


Figure 79. (a) Back side, (b) front side, of WB Sample 6, failure characterization, $R = 0.15$ m

Plate failure characteristics for AB Sample 7 are shown in Figures 80 and 81. Failure existed around three of the four sides of the plate at the clamped boundary. Severe delamination could be seen in Figure 80 circled in yellow. Severe fiber fracture around $\frac{3}{4}$ of the boundary was observed. Failure regions in Figure 81 were annotated in yellow and encompass more than $\frac{2}{3}$ of the area of the composite plate. This was the largest and most global failure observed in all of the plates tested. The global failure identified in AB Sample 7 was similar to that found in AB Sample 4 results.

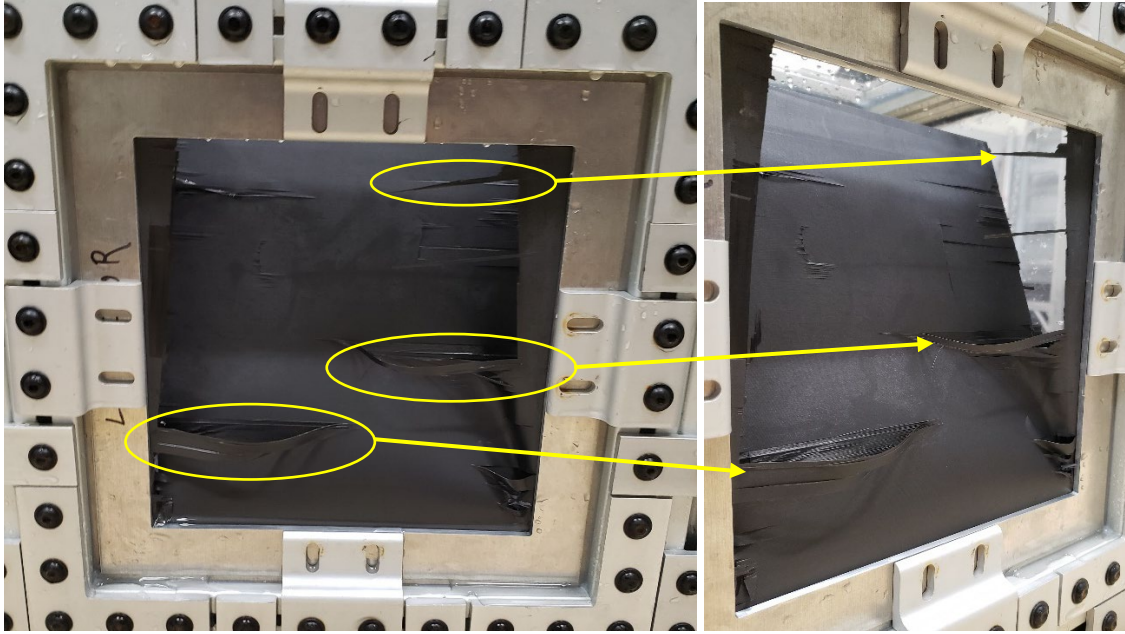


Figure 80. Failure of AB Sample 7, test run 4, $R = 0.3$ m

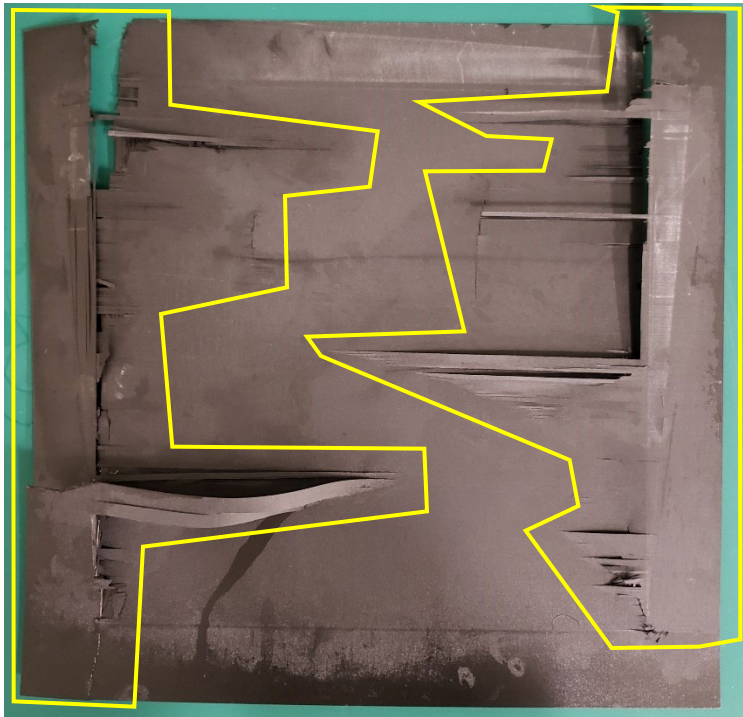


Figure 81. Failure characterization, AB Sample 7, $R = 0.3$ m

Pressure profiles for Samples 6 and 7 at failure can be seen in the figures 82 and 83. All other pressure plots are included in Appendix D. Sample 6 was tested with 5 runs until failure all at the WB condition. Sample 7 was tested with 3 runs until failure, all at the AB condition. Pressure loading for WB Sample 6 at failure ($R = 0.15\text{m}$), was approximately twice that of the failure loading on AB Sample 7 ($R = 0.3\text{ m}$).

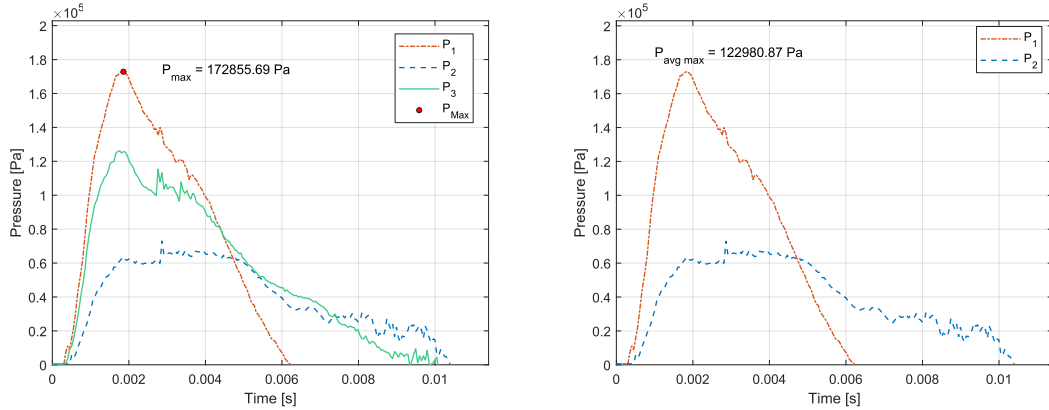


Figure 82. Overall pressure profile (left), plate failure loading (right), WB Sample 6, $R = 0.15\text{ m}$

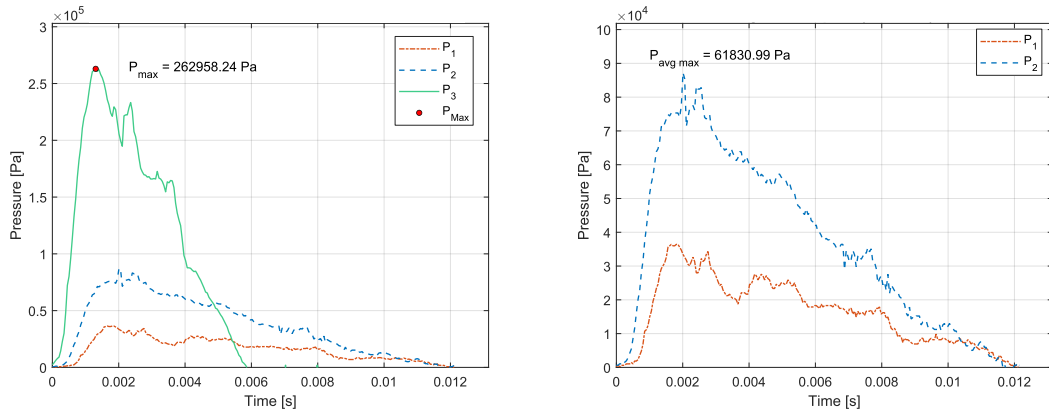


Figure 83. Overall pressure profile (left), plate failure loading (right), AB Sample 7, $R = 0.3\text{ m}$

A summary of the nodal pressures measured at each pressure gage location is given in Figure 84. As the charge moved closer to the composite plate, the standard deviation of the maximum pressures recorded increased due to the inherent directionality of the LN2

loading method. This aligned with our findings in the linear layout portion of the pressure results section. The difference between both mean loadings for WB and AB at $R = 0.3$ m, was 41.14 kPa (5.97 psi). Since the maximum mean loading of WB Sample 6 exceeded that of AB Sample 7 at the same stand-off distance, the failure threshold for WB Sample 6 was less than 0.3 m and greater than or equal to 0.15 m.

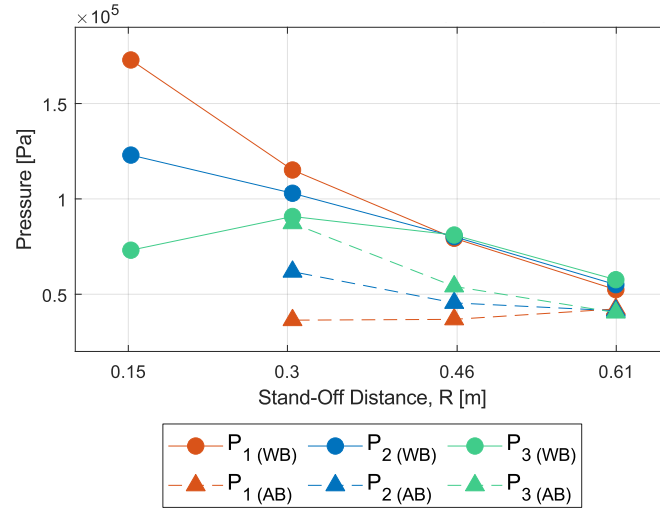


Figure 84. Maximum nodal pressures for WB Sample 6 and AB Sample 7

Strain time histories for both four-layer plates at their failure runs are shown in Figures 85 and 86. WB Sample 6 strain response in Figure 85 showed the x-direction nodes out-of-phase with one another. For the y-direction strain response, nodes 1 and 2 were in phase while node 3 was nearly 0 strain for the duration of the test run. Sharp increases in both tensile and compressive strain occurred like that seen in WB Sample 3 strain response. Time to reach maximum strain in the x and y direction for WB Sample 6 occurred at approximately $t = 0.08$ and 0.14 seconds respectively.

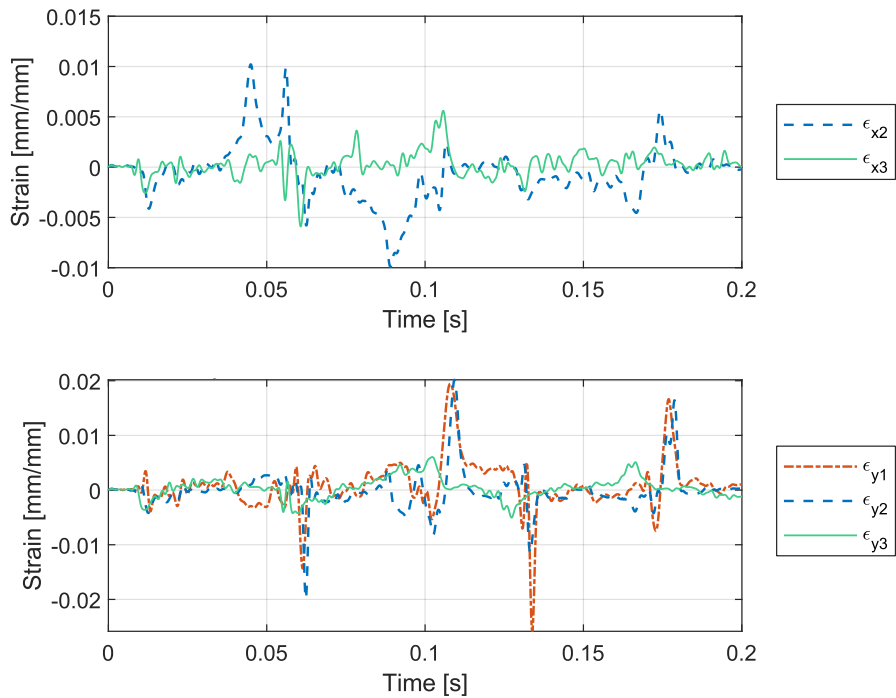


Figure 85. Strain response, WB Sample 6 (0-90-90-0°), R = 0.15 m, failure run

AB Sample 7 strain response in Figure 86 showed none of the principal nodes in-phase with one another. Gradual oscillation of the strain response for all x-nodes and node 1 in the y-direction was similar to that observed in AB Samples 1 and 4. Sharp increases in both tensile and compressive strain occurred like that seen in WB Sample 3 strain response. Time to reach maximum strain in the x and y direction for AB Sample 6 occurred at approximately $t = 0.06$ and 0.12 seconds respectively.

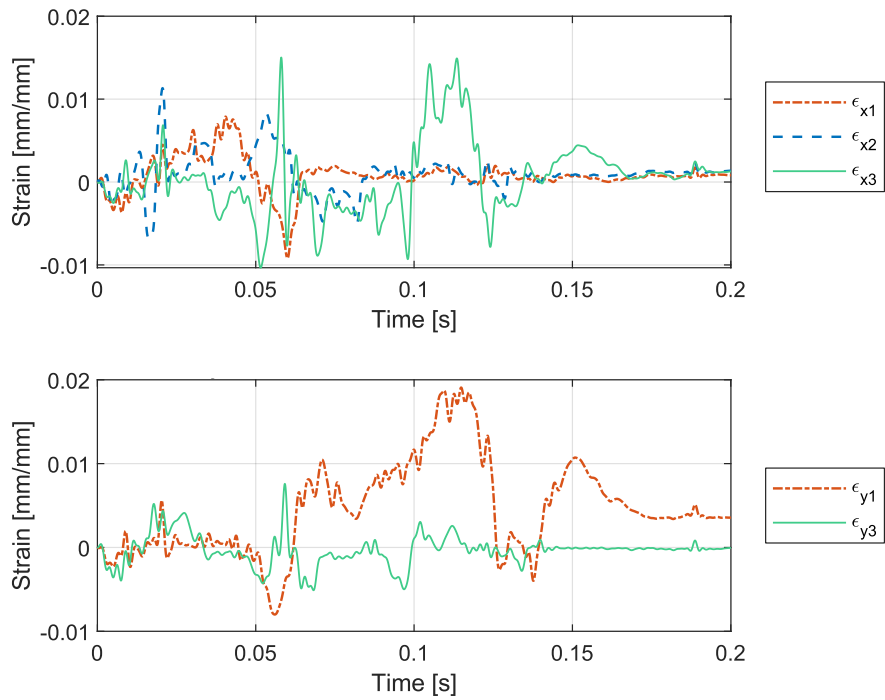


Figure 86. Strain response, AB Sample 7 (0-90-90-0°), R = 0.3 m, failure run

Identical to the three-layer strain analysis, the maximum tensile and compressive strains for the four-layer test runs were compiled for the x and y directions and then divided by the maximum pressure measured at each strain node. These results are seen in Figure 87 and 88, while the raw maximum strain results as a function of stand-off distance are included in Appendix C.

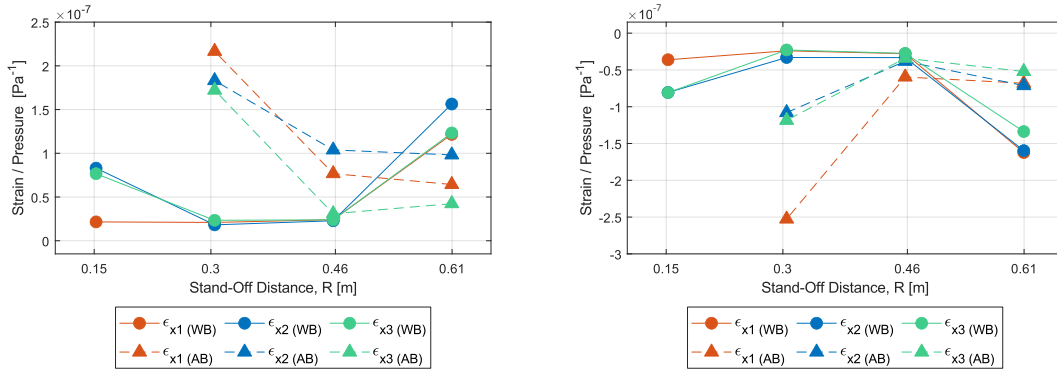


Figure 87. Normalized WB and AB max x-strain result comparison until failure (0-90-90-0): (left) tension, (right) compression

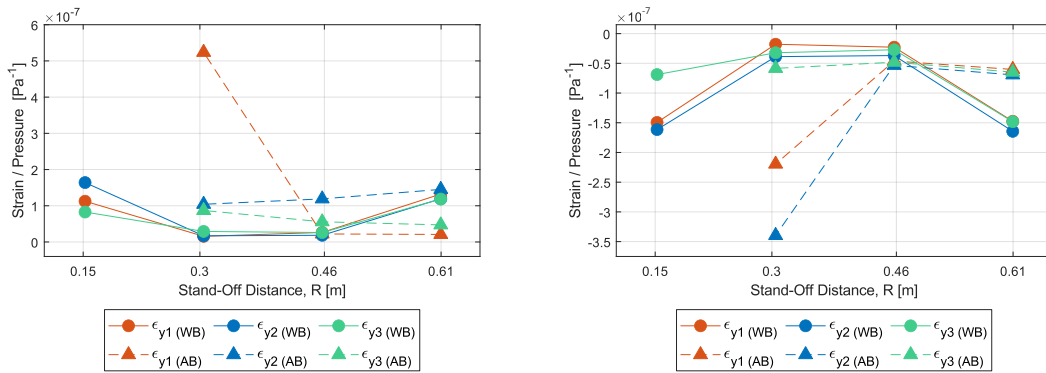


Figure 88. Normalized WB and AB max y-strain result comparison until failure (0-90-90-0): (left) tension, (right) compression

Similar to the findings comparing the three-layer plates, the AB four-layer plate exhibited larger maximum strains than the 0–90–90–0 WB plate. Further, the spread of the AB data points at each stand-off distance remained a consistent difference from the WB data points being near one another. Some of this was likely due to FSI, where the plate was less free to move in the WB case than the AB case. With no resisting force in the AB case, the plate was free to move, and if the loading was not symmetric across the composite plate each node was less restricted from moving in a more non-uniform fashion than that of the WB. The effect of FSI would also create a damping effect to the applied loading against the composite plate in the WB testing cases. This meant the strain response of the structure

would be lessened because of the coupling of the fluid with the structure due to FSI. Finally, the WB data points seemed to display a parabolic trend with strain as a function of stand-off distance. For the WB case, the maximum strains had a concave up inflection point between 0.3 and 0.46 m. AB showed a similar characteristic if the testing has been started at a much further away stand-off distance. Both x and y maximum strains appeared to intersect near a stand-off distance of 0.46 m, where their values were identical for opposite backing conditions. Further significance of this intersection point should be investigated. Additional testing will be necessary to understand if this is a repeatable physical phenomenon of the composite material or simply a statistical outlier because of our small data sample size for this research. During the signal processing portion of this research, it was observed that the frequency of the strain response increased dramatically at greater than or equal $R = 0.61$ m. This means it will likely require the use of a better signal processing filter beyond the Butterworth filter currently in use to accurately capture the complex response and loading dynamics of composite structures in a marine environment while removing noise from the final data being evaluated. A summary of the final test matrix results for every test run is provided in Table 4.

Table 4. Carbon fiber composite plate test matrix results

Sample	Orientation (°)	Thickness (mm)	Stand-Off Distance, R (m)						Key
			0.15	0.3	0.46	0.6	0.76	1	
1	0	0.52			AB				Failed
2	0	0.55			WB				Survived
3	0-90-0	0.38			WB	WB			No Data Available
4	0-90-0	0.38						AB	Untested
5	0-90-90-0	0.53							Untested
6	0-90-90-0	0.53	WB	WB	WB	WB			Survived
7	0-90-90-0	0.55		AB	AB	AB			Failed
8	0-90-90-0	0.55					WB		No Data Available

V. CONCLUSIONS

In this research a CTR was successfully fabricated and utilized to house a carbon fiber composite flat plate for testing in an underwater marine environment. The CTR design also effectively provided the ability to test composite plates with varying fiber orientation and different backing conditions, either AB or WB. Pressure characterization of the LN2 shock loading method was accomplished. This included verifying directionality existed in the LN2 loading source as well as demonstrating the pressures generated from the shock front reasonably fitted an exponentially decaying curve over time. DAQ parameters for strain gages were accurately determined and applied to two of the three pairs of composite plates tested. Three pairs of composite plates with three different fiber orientations were tested using the LN2 loading method with a PPV to provide shock loading against these composite plates. Single square plate WB and single square plate AB were accomplished in the test matrix for this thesis. Maximum strain in nearly all cases of testing was larger for AB plates. Composite plates in this research that were WB, survived at nearly twice the distance of the matching AB plates. Parabolic trends in the WB data over stand-off distance was observed. However, more test-runs need to be conducted to verify if this accurately represents what is physically occurring between the structure and fluid. An intersection point of maximum strain was observed at a stand-off distance of 0.46 m for both AB and WB four-layer composite plates. AB data points in the maximum strain plots vs. stand-off had a higher standard deviation than the WB data points. Local failure was observed in two out of the three WB composite plates tested, whereas, global failure was observed in two out of three AB composite plates tested. More research effort is required to provide an accurate explanation of why local and global failure is occurring in contrasting backing conditions. Finally, the CASPUR system was successfully designed, built, and operationally tested.

THIS PAGE INTENTIONALLY LEFT BLANK

VI. FUTURE WORK

Pressure characterization of the new CASPUR system will be important to ensure the characteristics of the shock front are steep. Additionally, investigation of the bubble mechanics of the new system is required to understand all loading mechanisms produced by CASPUR on a structure of interest. Furthermore, examining how changing the volume of the shock pipe assembly affects the produced shock front as well as bubble geometry and propagation underwater would be beneficial.

Testing plates of same fiber orientation and thickness first in series, with one plate affixed to the front and back of the CTR box. Secondly, a sequence of testing of different ply orientations could be conducted to examine if there is a correlation between optimum thickness or ply-orientation on reducing strain response or damage and failure in the plates. If larger loading capacities are realized by CASPUR, sandwich composite plates of several WB and AB backing layers would be valuable to investigate. Coming up with an innovative way to change the boundary condition of the CTR to force the composite plate to fail at the center like that of a tensile test, vise the plate regularly failing at the stress concentrated boundary. Working to develop modifications to the current CTR to provide boundary conditions that force the failure towards the center of the sample and away from the typical high-stress concentration areas as highlighted in [2-3].

Fabricating and testing composite cylinders as well as concentric composite cylinders would be a valuable direction to continue in with this research in both AB and WB backing conditions. Moving from macro analysis of material response and failure to completing micro analysis into the overall assessment and performance of a material would be invaluable. Strain gage placement on the front and back of the plates to examine how the strain response is different in both backing condition set-ups at the opposite surface side. Finally, since only eight channels are available on the Wheatstone bridge used in this research, using only the x-strain nodes on a strain gage would allow a matrix of strain gages to be employed over more of the surface of the plate. This could provide further insight into why local and global failure was observed in the WB and AB sample respectively.

THIS PAGE INTENTIONALLY LEFT BLANK

APPENDIX A. WHEATSTONE BRIDGE

Appendix A provides specific guidance for the equipment used in this research for strain data collection. Some troubleshooting guidance is provided at the end of this appendix to reduce repeated mistakes when using this lab equipment. For a more in-depth explanation of how the Wheatstone bridge works please see Reference 23.

***** DO NOT energize power supply, unless all strain gage lead wires are already connected to alligator clips to avoid shock/injury as described in Appendix B. DO NOT touch bare wires, alligator clips, or any hot portion of the strain circuit while this power supply is on.*****

- 1) Power Supply. The power supply shown in Figure 89, when energized, provides the excitation voltage, V_{EX} , required for the Wheatstone bridge. 10 V is the value used in this research, but it can be any value appropriate for the specific application.

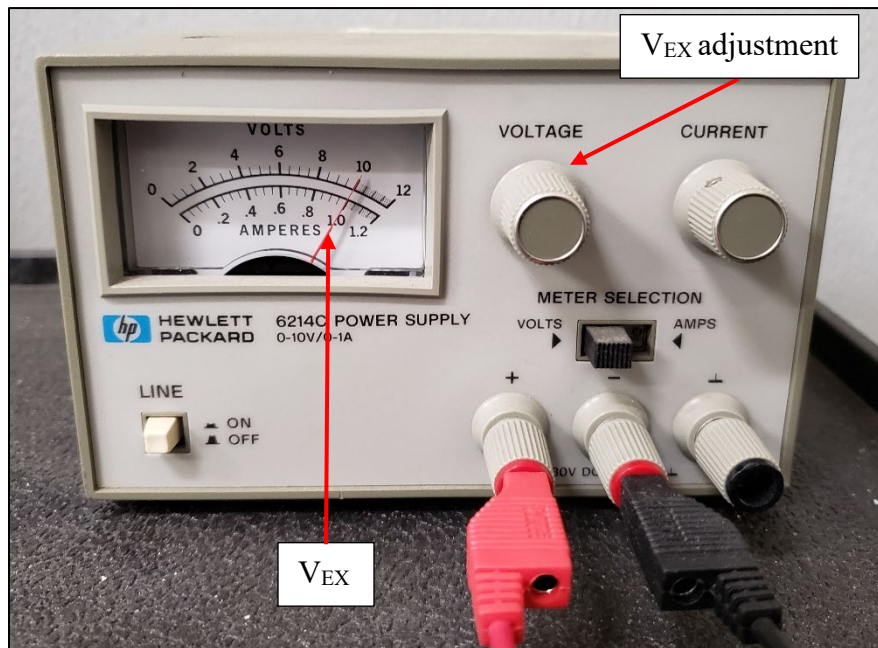


Figure 89. Power supply, at 10V V_{EX} setting

- 2) The Voltage output selected via the voltage knob on the HP power source shown in the Figure 89 is how the VEX value is chosen for the strain data collected. Optimization of the VEX value is describe in Reference 25. This VEX value is inputted to NI Signal Express, as specified in Appendix B.
- 3) Bridge Connection. Ensure the banana plugs are properly connected in the manner shown in the Figure 89 and Figure 90 to the power supply and the Wheatstone bridge: red to positive, black to negative.



Figure 90. Correct banana plug connections from power supply to Wheatstone bridge

- 4) Quarter Bridge. There are 8 nodes on the input and output sides of the Wheatstone bridge in Figure 91, labeled 0 through 7.

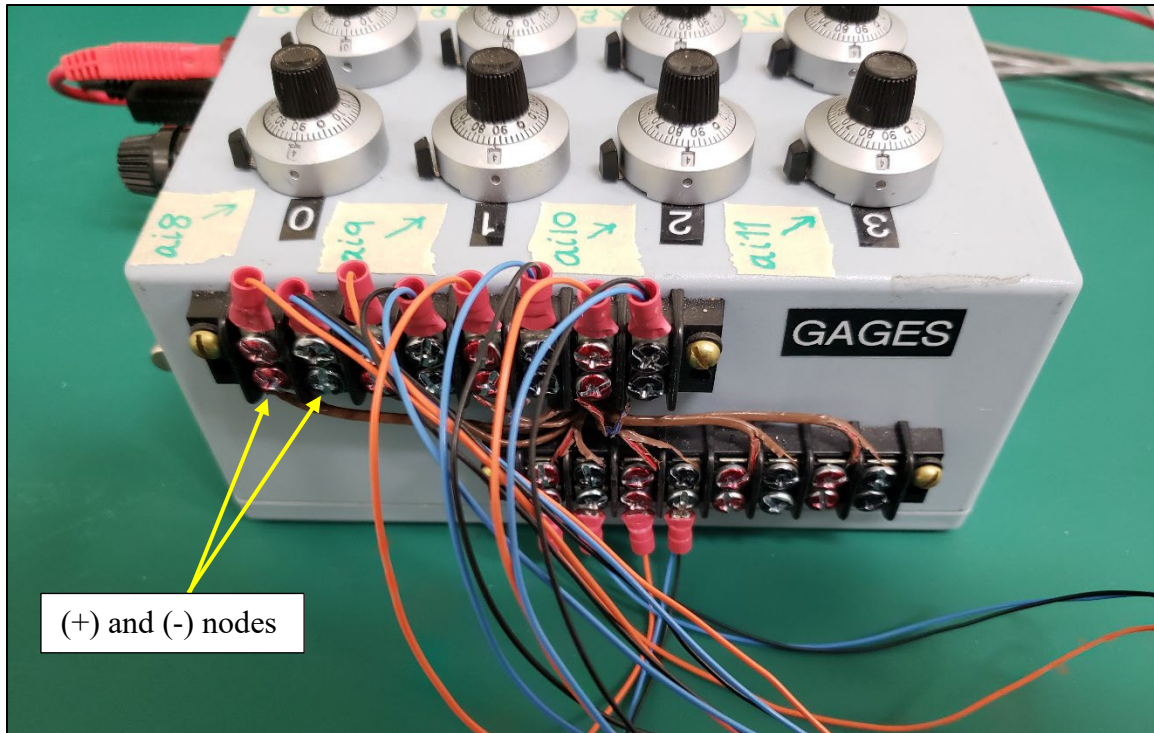


Figure 91. Wheatstone bridge input nodes

- 5) The input nodes are shown in Figure 91 for the Wheatstone bridge. These nodes pass the voltages measured across the strain gages on the composite plate being tested to the output side of the Wheatstone bridge. The output nodes of the bridge move the voltage data over the gray insulated wires, to the SCB-68a already shown in Figure 21. On the input side of the bridge, one wire cable consisting of a black and blue and red/orange wire connects to one node. On the right side of the bridge one wire cable connects to two nodes (red/black first and green & white second). Each node has a corresponding positive (left) and negative (right) component. Red must be connected to the positive side for all the nodes on the left and side of the bridge. Alternating red and green should be connected to all the positive nodes on the right side of the bridge as indicated previously.
- 6) Connectivity Issues. If there is any concern of proper circuit connectivity, this is most easily confirmed if **NO** change in signal is observed after completing the steps laid out

in Appendix B. A DMM in the work bench or one from Dr. Park can be used to check for continuity, to ensure no connection point has become damaged.

a) Ensure the power supply is turned **OFF**.

i) DMM Operation

ii) Turn the knob of the multimeter as shown in Figure 92. If continuity exists (i.e., the circuit is not broken) an audible sound will emit from the multimeter.



Figure 92. Continuity check function selected on DMM

iii) This is only true for the negative components of the circuits found inside the Wheatstone bridge. Placing a lead of the DMM on the input side of the bridge and the negative portion of the node, do the same with second lead of the multimeter on the corresponding output side node. If no beep emits, there is an issue with one of the many connections that exist between the input and output side on the internal parts of the bridge. A straightforward but tedious process requires, to open the bridge (small screws on the bottom allow for access into the internal parts of the bridge once removed) and test continuity for the negative components in sequence starting from the first external input to the next exposed point internal to the circuit. Two things were found during the most recent continuity check of the bridge.

7) Past Issues

- a) First. One of the leads going from the input nodes to the first green connection point on the yellow board, labeled “GAGES,” had deteriorated where it was connected to the board. After re-stripping that wire and inserting it back into the green connection point, continuity was established. This internal portion of the bridge is shown in Figure 93.

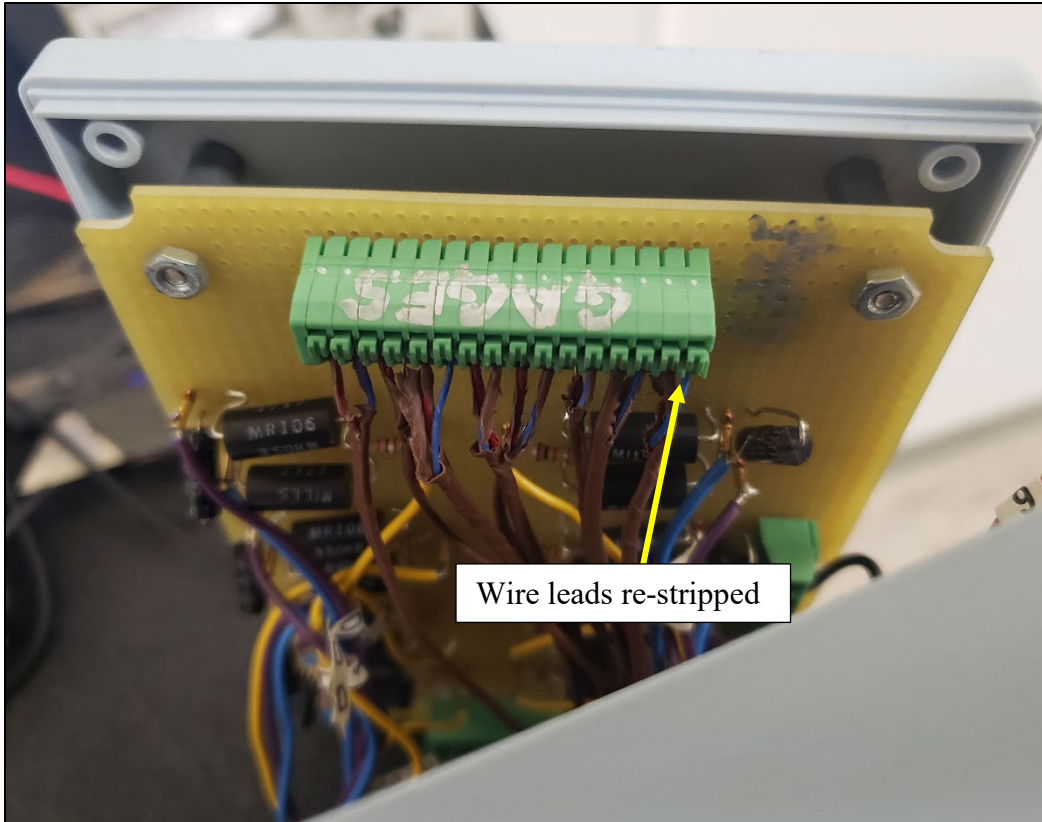


Figure 93. Internal node location for bridge needing repair

- b) Second. One of the blue wires on the underside of the yellow board had broken free from its previous solder point similar to that shown in Figure 94. Once re-soldered, continuity was re-established.

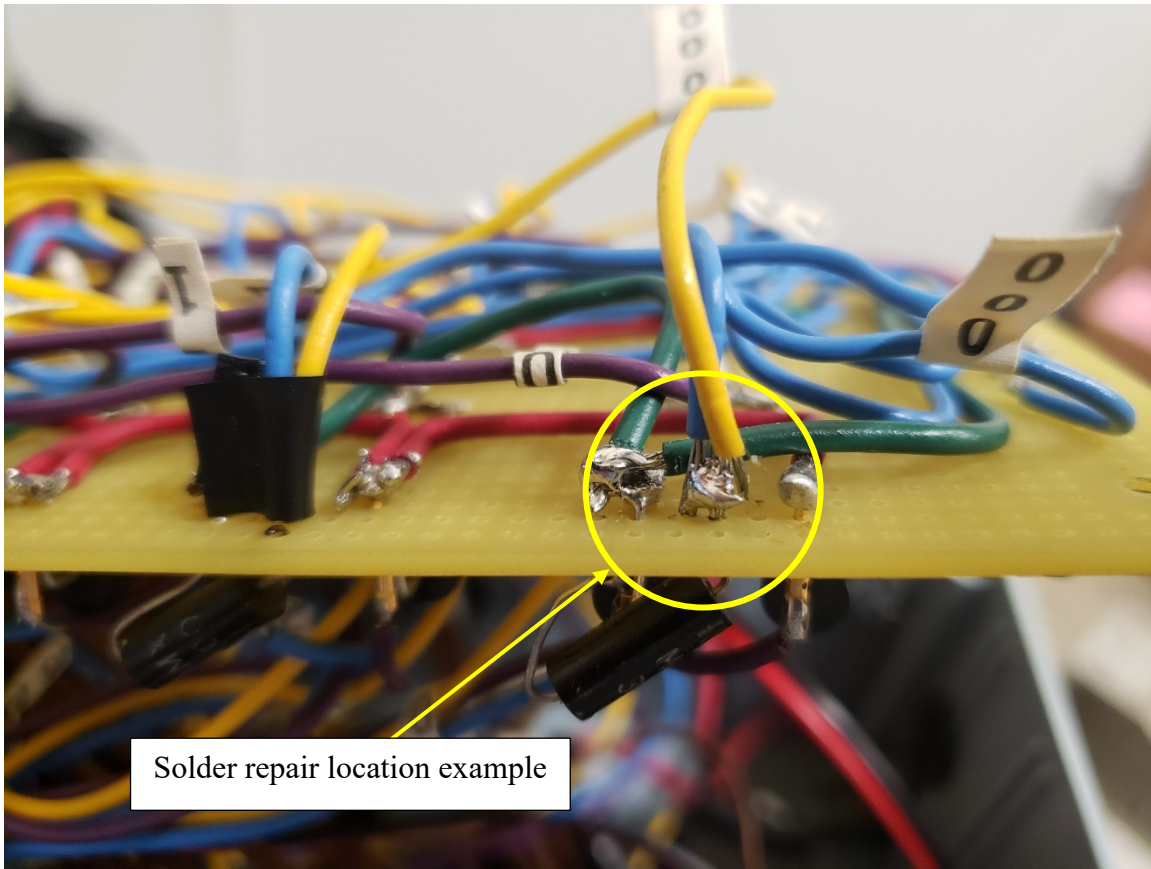


Figure 94. Wheatstone bridge internal board, blue wire repair site example

- 8) Resistance Check. After verifying continuity from the input across to the output, it is worth changing the multimeter to the resistance setting to check for reasonable resistances across each of the resistors on the yellow board as shown in Figure 95.

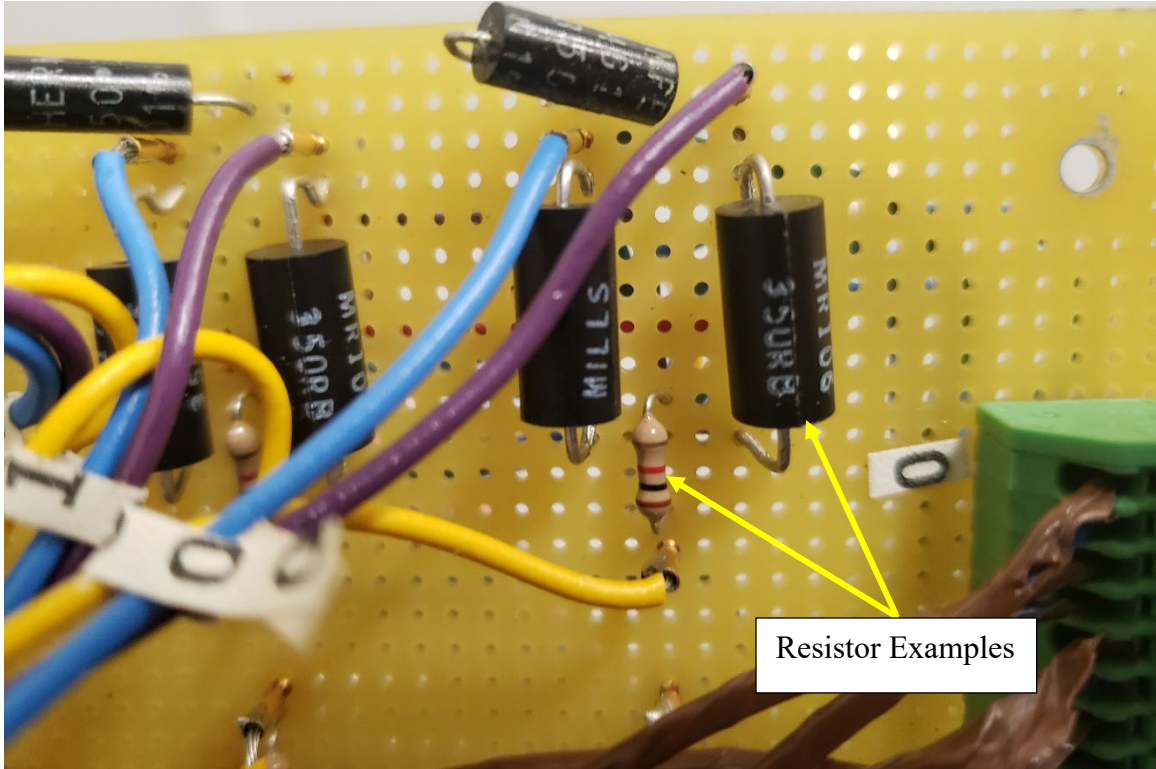


Figure 95. Wheatstone bridge, internal view, top board, resistors

- a) Although it highly unlikely that this is the failure point of the Wheatstone bridge, this is worth checking because of the effort required to disassemble and reassemble the bridge. All like resistors should be within $\pm 5 \Omega$ from each other. If they are significantly different from each other, one of them may need to be replaced.

APPENDIX B. CASPUR OPERATING, TESTING, AND DAQ GUIDE

Appendix B provides specific step-by-step guidance on how to safely operate CASPUR. Instruction is provided for how to operate the live data feeds through NI Max to verify initial sensor functionality as well as DAQ through the Signal Express application.

- 1) Ensure CASPUR is **OFF**: Valves for this procedure will be referred to as delineated in the following Figure 96. Compressed Gas Valve 1 (CGV-1), Regulator Valve 2 (RV-2), Two-way valve 3 and 4 (2WV-3 and 2WV-4). Gages are labeled as high- pressure gage 1 (HPG-1), and low-pressure gage 2 (LPG-2).

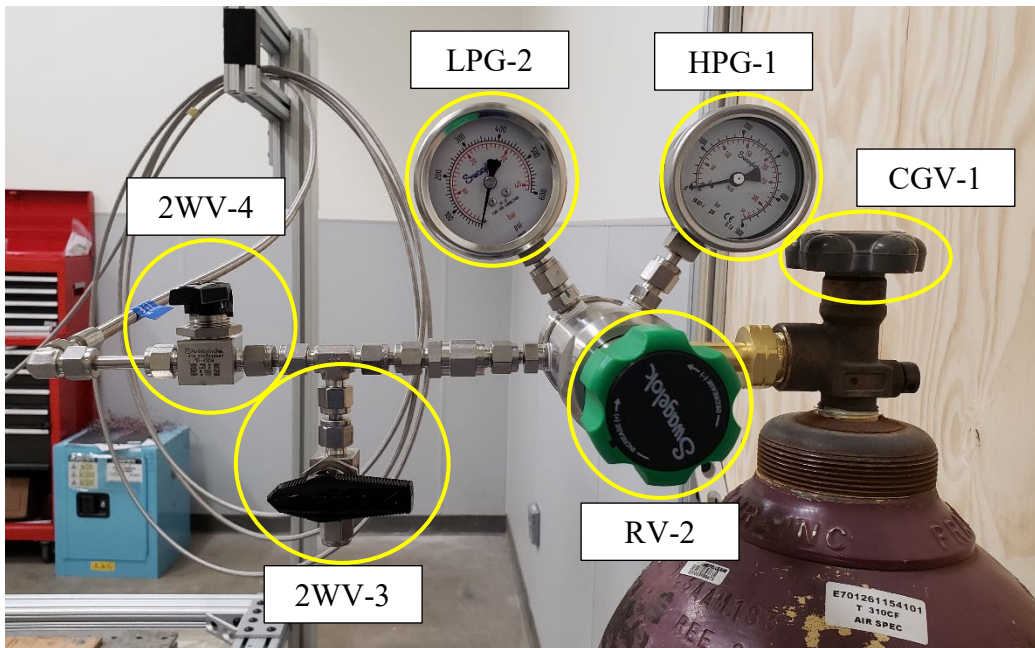


Figure 96. Valve labels for CASPUR operating procedures

- a) Confirm compressed air tank saddle is tight.
- b) Verify all four valve handles of CASPUR, in Figure 96, are in the closed position (perpendicular to the flow direction for the two-way valves, and rotated in the proper closed direction indicated on the regulator and compressed gas tank valve handles).

- c) Verify HPG-1 and LPG-2 inlet and outlet gages on the regulator read 0 psi. If either gage does not read zero:
- i) Put on single hearing protection and eye protection
 - ii) Ensure CGV-1 and 2WV-4 are still closed.
 - iii) Open 2WV-3 slowly until fully open.
 - iv) Crack the RV-2 handle to open and slowly throttle the regulator to more fully open and ensure venting can be heard from 2WV-3 (the first two-way cut-off valve for the system supply).
 - v) Once HPG-1 and LPG-2 both read 0 psi, return RV-2 and 2WV-3 to closed.
- d) Inspect the 30 ft stainless steel flexible hose for any damage or wear. Cease operation immediately and notify thesis advisor if any damage to hose is identified on the external casing of the hose.
- e) Understand that if any Swagelok fittings require replacement, depending on whether the component is a tube adapter fitting or a regular tube fitting the number of turns for tightening is significantly different. Tube fittings currently require 1 and $\frac{1}{4}$ turns to tighten, while tube adapter fittings require only $\frac{1}{4}$ turns to tighten. Exceeding this guidance can damage the fitting and prevent a leak tight seal from being established between fittings. Tube adapter fittings do not have ferrules accompany them when assembling. Tube adapter fittings allow for fitting-to-fitting connections. Ensure the tube or tube adapter male end is fully seated against the internal part of the female connection fitting prior to tightening, to provide sufficient material for the compression process to have enough material to bite on. Excellent online guides exist, just ensure you are watching videos that are explicitly the fitting size and fitting type you are using. Connecting as many conjoining Swagelok components as possible through the use of a vise will help to avoid bending and damaging any of the tube adapter male ends unintentionally. Caution must be taken when using a vise for the assembly process in that the vise should not be overly tight where the actual internal shape of the fitting body becomes

damaged and squashed due to excessive force applied to the vise. Ensure softer vise jaws are used to protect the fitting body from being damaged during the assembly process.

- 2) Ensure Wheatstone bridge power supply is **OFF**.
- 3) NI DAQ initialization. Power on the NI system by pressing the power button shown in Figure 97:

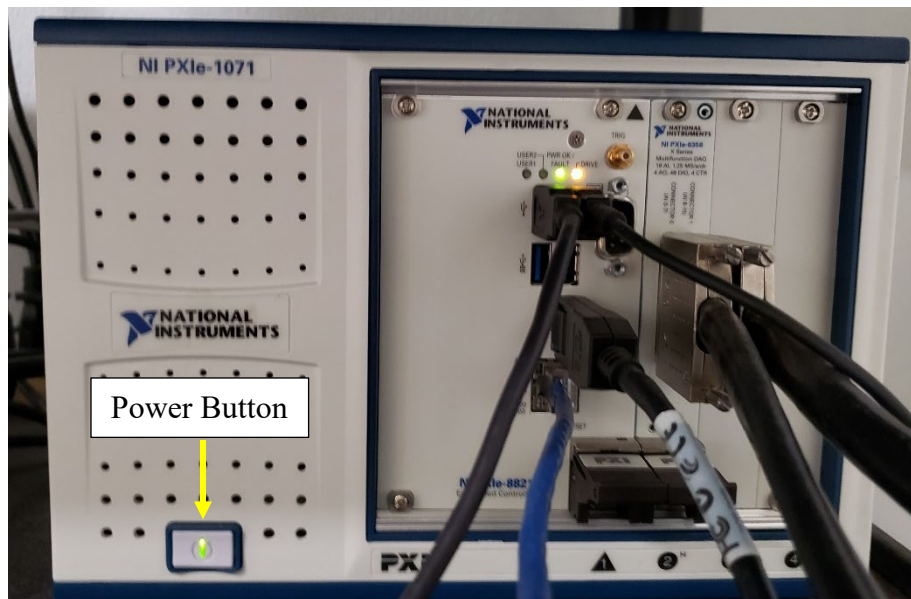
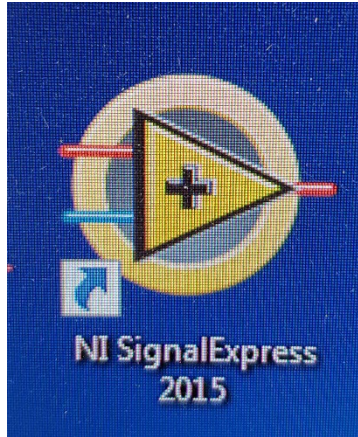


Figure 97. NI Suite, power button shown for system start-up

- a) Open Signal Express (icon shown from desktop), or open a project directly if one is already in use:



b) Open NI Max (icon shown from desktop):



- i) Select, “Devices and Interfaces” on the left
 - ii) Select, “NI PXIe-1071”
 - iii) Select, “Self-Test” in the top right. You should receive a message that says “The self-test completed successfully.” This means NI can successfully communicate to each of the devices connected in the overall NI suite for this lab set-up. Repeat this process for selecting NI PXIe-6358.”
 - iv) Once “Self-test” is successful for the 6358, click on “Test-Panels” in the upper right screen.
- 4) Connect all the ICP[®]s (underwater blast sensors) to the PCB signal conditioner as shown in Figure 98. ICP[®] sensors will always be connected to “ICP[®]” port in the back

of the signal conditioner, and the BNC cables will always be connected to the “output” port on the back of the signal conditioner.



Figure 98. Proper BNC and ICP® sensor connection to signal conditioner for Channel 1

- a) Additionally, if the ICP® sensors are properly connected to the signal conditioner, as shown in Figure 99, no LED light indicator should be illuminated for the respective channel being used as shown in the Figure 76. If the cable of the sensor is damage for example, the “short” light indicator seen in the Figure 99 may light in red. Red lights seen Figure 99 show that channels 2–4 are available to use if additional ICP® sensors need to be connected.

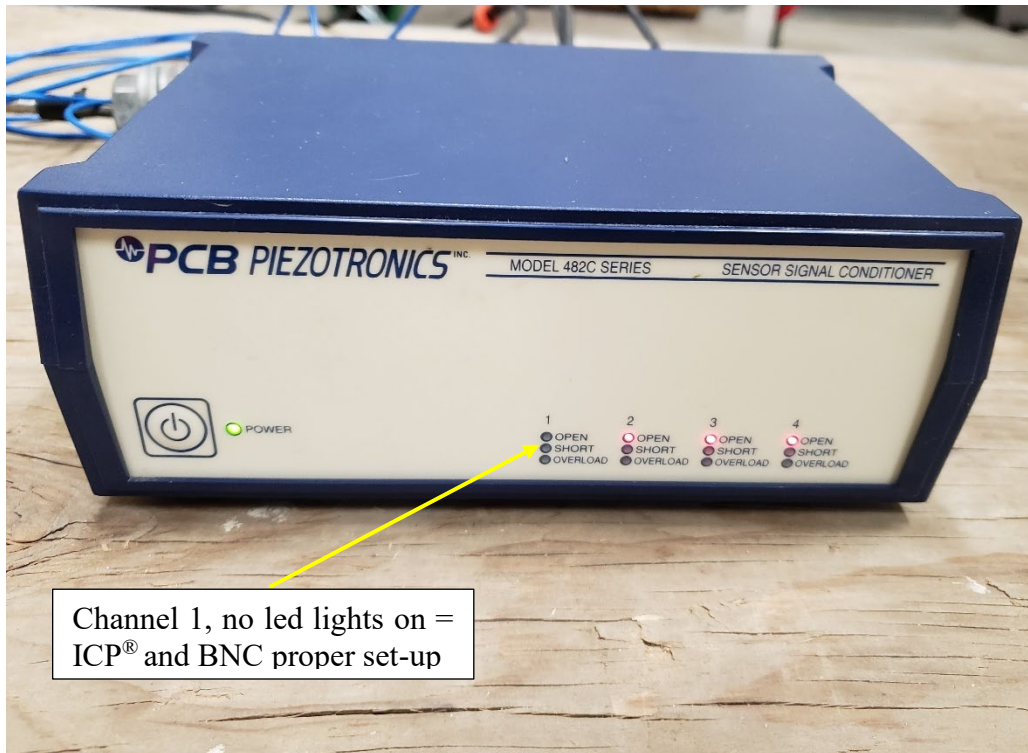


Figure 99. Signal conditioner light indicators

- b) To prevent confusion after collecting data, best practice is to always have the same pressure sensor correlated to the same BNC cable as shown in Figure 98. Meaning, the outlet side of the BNC cable labeled “A” would be paired with the ICP[®] pressure sensor labeled 1. Further, the inlet side of the BNC cable should be connected to the same AI channel number on the BNC-2110 as its outlet channel number is on the signal conditioner. Ensure that you know which serial number correlates to the number you assigned for your ICP[®] sensors because each sensor has a different sensitivity on its respective calibration sheet meaning the mV to MPa conversion will be different depending on which sensor you are analyzing data from in MATLAB[®].
- c) Because the ICP[®] sensors are sensitive and delicate instrumentation, they should always be disconnected and stored away from the testing area once testing is completed for the day to ensure no one steps and or accidentally damage the sensor. Therefore, it is recommended to keep the ICP[®]s well clear of the AWT deck area

until both the CTR and the shock carriage is fully in the water to prevent inadvertent damage to the sensors.

- d) Allow approximately 1 minute for the sensors to normalize after connection, per the PCB Operating manual [26].
- e) Using the “Test Panel” function in NI Max, select the appropriate channel for the respective ICP[®] sensor. Channels ai0 to ai7 on the BNC-2110 can be used for pressure data collection, and the same correlating channels in NI-Max selected for pressure sensor validation test. Certain channel combinations between the BNC-2110 and the PCB Signal Conditioner box will produce more noise seen in the signal processing. Channels 1, 3, and 4 on the signal conditioner and the corresponding ai1, ai3, and ai4 on the NI BNC-2110 have been optimum for noise reduction for this research. Gently squeeze the boot of the sensor to ensure you see a dynamic response in the live response shown in the continuous time plot of NI Max seen in Figure 100. Since the sensor measures dynamic pressure, the live plot will drop back to zero shortly after that slight impulse.

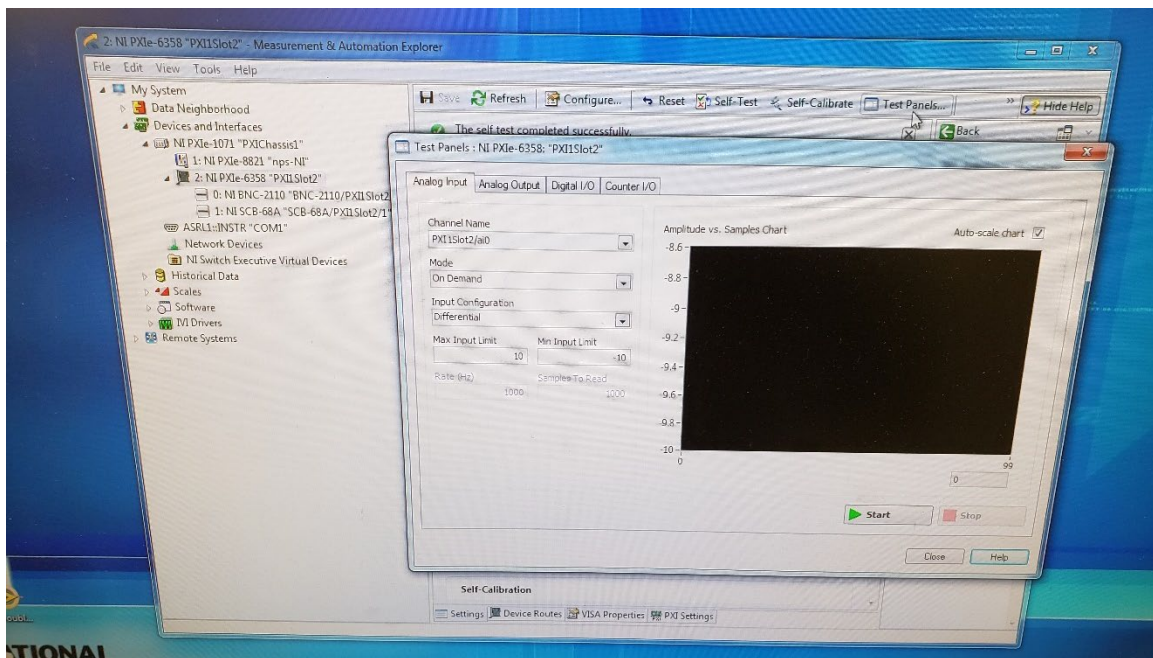


Figure 100. NI Max, Test Panels interface

- f) **DO NOT** squeeze on top of the tourmaline crystal in the sensor, otherwise this could permanently damage the ICP[®] sensor. If no signal response is seen in the live plot of NI Max shown in Figure 100, it is recommended to not proceed further with the system set-up process until the functionality of the ICP[®]s is restored.
- 5) Rupture Disk Installation. Follow the detailed guidelines provided by the manufacturer on the inspection of the disk, holder, raised face of the flange, as well as the tightening patterns, 25 % torque increase, with a minimum of four sequences, following the torque requirements for both the 5/16 inch hex bit bolts for the holder, as well as the torque requirements for the 15/16 inch hex nuts on the studs for the flange tightening. Ensure all components are free of defects, scratches, debris, and rust.
- a) Green Garlock gaskets provided by manufacture are best suited for this system application shown in Figure 101. It is unknown how many times the gasket can be re-used to guarantee a leak tight seal.



Figure 101. Gasket used for flange to holder sealing for CASPUR

- b) CASPUR leak check. There must be no leaks present from two critical performance areas: between the rupture disk holder and the flanges as well between the rupture disk and the holder itself. If leaks are present in these two critical areas the rupture

disk will not perform as designed and could rupture below or above the design rupture pressure. This means if leaking is found in either critical area in the following steps, the carriage must be retrieved and CASPUR troubleshooted after safely de-pressurized.

- i) Ensure all personnel in WA122-A are wearing safety glasses and double hearing protection prior to starting leak check.
- ii) Once shock carriage is submerged to mechanical stops, begin fill process by 10 psi increments with a maximum final pressure of 100 psi in the following way.
- iii) Ensure all valves are closed and HPG-1 and LPG-2 gages read 0 psi.
- iv) Open compressed air tank valve slightly until tank pressure registers on HPG-1 of the regulator. Record the starting pressure of the compressed gas tank.
- v) Open RV-2 until 10 psi registers between it and 2WV-4.
- vi) Open 2WV-4 slowly but all the way to open, and then increase opening of RV-2 until LPG-2 shows a pressure of 10 psi downstream of the second stage regulator. At 10 psi increments up to 100 psi, verify that no leaks are present from the two critical areas mentioned above. If leaking exists at one of the two critical locations mentioned above, the leak check is considered UNSAT. Small bubbles from the threaded two-inch fittings after the tube to NPT fitting is acceptable, if no rapid and significant loss of pressure displays at LPG-2.
- vii) If the leak check is UNSAT, to depressurize the system close CGV-1, and 2WV-4, in that order. Crack open, 2WV-3 to vent air between the tank and 2WV-4. Open 2WV-4 to relieve the remaining pressure in the line between the rupture disk and the check valve just after the regulator. Ensure HPG-1 and LPG-2 read 0 psi. Close RV-2, 2WV-3, and 2WV-4 in that order. At this point CASPUR is safely depressurized and off, and the shock carriage can be retrieved from the AWT where the leak issues can be resolved.
- viii) If the leak check passes, the carriage will remain fully submerged, and the system depressurized following the previous steps above. This is done to and

ensure a safe working environment until the test set-up process is complete, and to preserve the compressed air supply in the tanks.

- c) If a different length pipe is required to be installed into the shock pipe assembly, a flange mounting block has been made, as shown in the following Figures 102 and 103, in concert with two c-clamps, and two vises. Using two pipe wrenches, while being careful to protect the flange body and flange face from getting scratched or damaged, all two-inch fittings can be tightened sufficiently after properly taping the threaded fittings with PTFE tape.

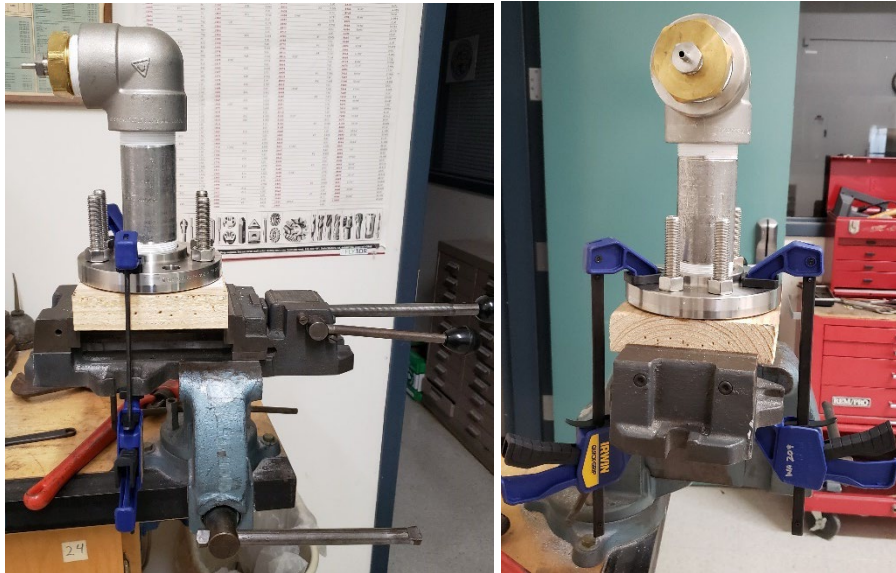


Figure 102. Flange block set-up for shock pipe length adjustment

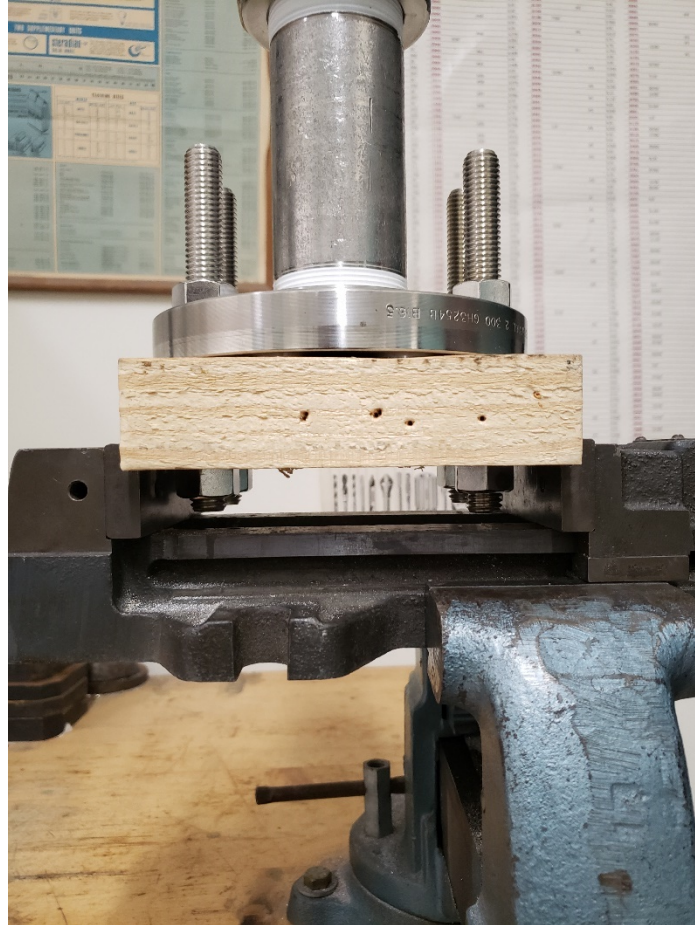


Figure 103. Flange block side view for 2-inch NPT threaded fitting tightening procedure

- 6) CTR set-up. Before installing the composite test sample into the CTR, record the GF and resistance values for the strain gages used on your test sample (350 Ω have been used in this research, but will be specified by the manufacturer on the packaging that the strain gages came in. The GF can vary between packages, so ensure you know the correct GF for every strain gage on your test sample. These GF and resistance values will be entered into Signal Express in a later step of this guide.
 - a) Wearing nitrile gloves is recommended when installing and removing the composite plates to protect skin from small carbon fibers. Gloves will also protect hands from duct seal installation for wire sealing through back of the box of the CTR (only used for AB testing only).

- b) Ensure all wires are labeled consistently and verify their proper sequence that you have pre-determined. This ensures you know which strain wire of the composite plate will connect to its corresponding wire of the Wheatstone bridge. Once the CTR is in the water, it is not possible to verify the wire number correlation of the strain nodes.
- c) Insert composite plate to front of CTR box with strain gages and wires facing inside of the box. Attach outside aluminum window over test plate using s-shaped retainer clips as shown in Figure 11 of Chapter II of this thesis. Ensure retainer clips are tightened only as much is required to prevent water intrusion around the boundary without over stressing the boundary of the plate.
- d) WB testing. Attach strain gage wire leads to orange tie-offs on cross-rails to protect the exposed ends from water exposure and to protect the strain gage from damage or the composite plate from pre-strain. CTR is ready to be placed at desired stand-off distance from CASPUR, and strain wire leads attached to alligator clips. Ensure power supply for Wheatstone bridge is powered OFF before attaching strain gage wire leads to alligator clips.
- e) AB testing.
 - i) Route wires through centered hole of similar thickness composite plate at the back opening of the box shown in Figure 104.

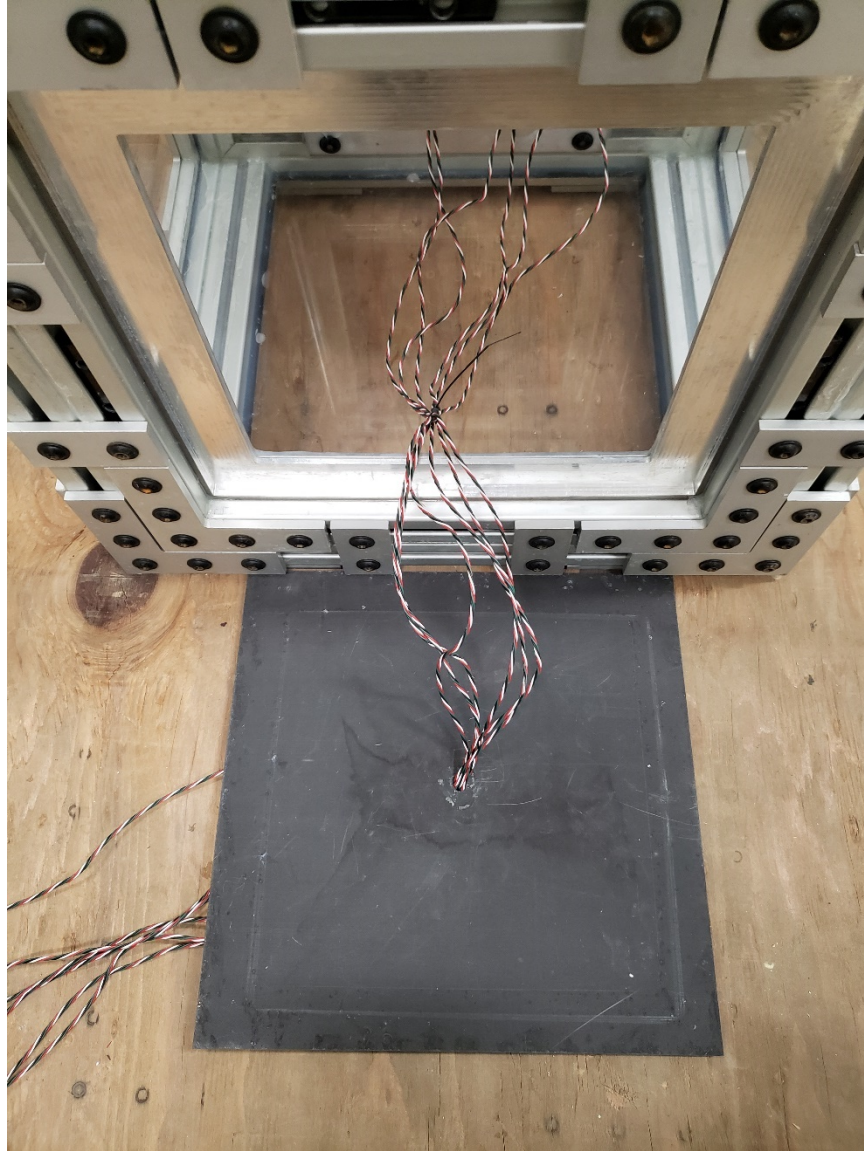


Figure 104. Wire routing for AB set-up

- ii) Secure small zip-tie around wires to protect wires from being pulled off strain gages and to prevent plate from being pre-strained shown in Figure 80. While still wearing nitrile gloves, apply duct seal around the wires with the zip-tie flush to the surface of the inside of the back composite plate.



Figure 105. Zip-tie placement to prevent strain gage damage

- iii) After securing the back composite plate to the box, apply duct seal around the wires for additional water tightness as shown in Figure 106.
- iv) When composite plate is inserted into back window of the back of the box there should be a gentle sag in the wires from the front test plate to the back plate.

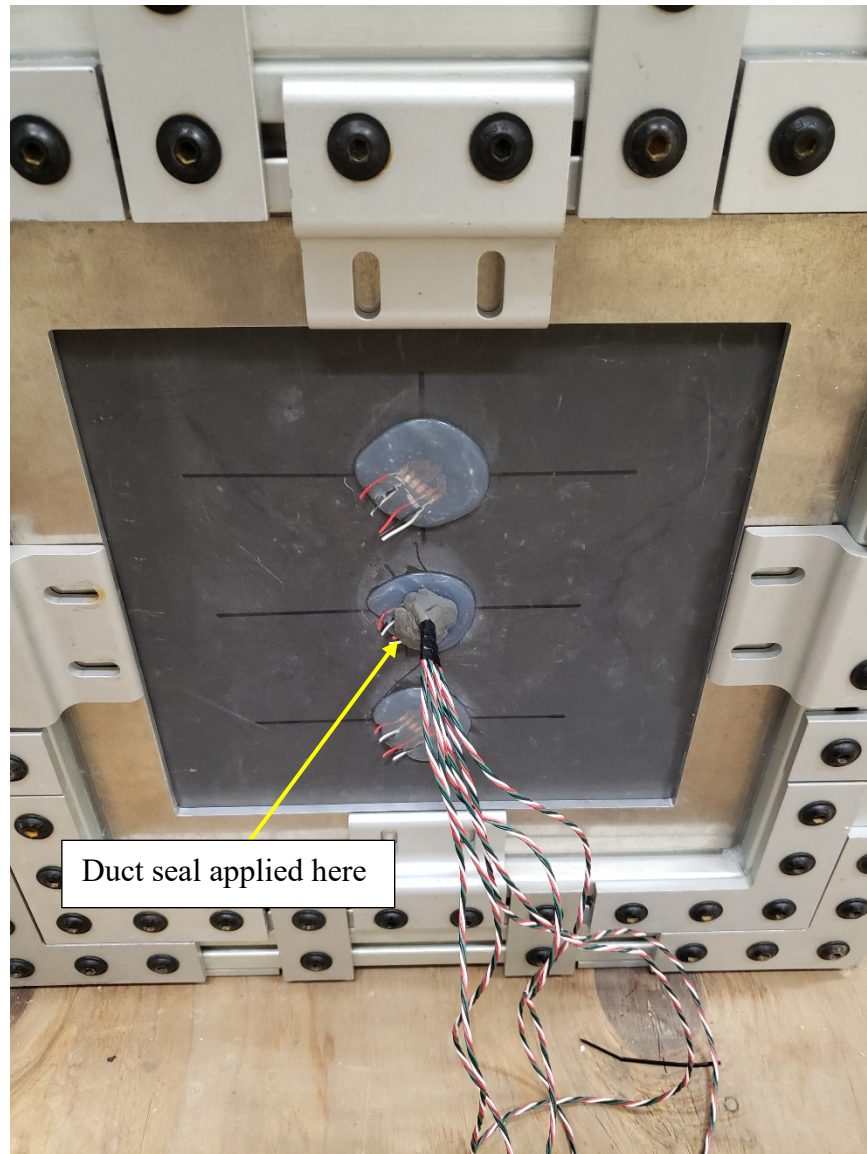


Figure 106. Back composite plate with wire routing and duct seal

- v) For AB testing, be poised to connect wires and place pressure sensors efficiently to ensure the AB condition is maintained before shock loading can be induced on the composite plate.
- 7) Data path connections.
 - a) For AB and WB testing, once CTR is on AWT deck, at desired stand-off distance, and Wheatstone bridge power supply is verified to be off, connect strain gage wire leads to alligator clips of wire leads of bridge.

- b) Verify proper wire sequencing between Wheatstone bridge wires and strain gage wires. This means the first node of the bridge should be connected to the first node of your first strain gage on your composite sample. This prevents confusion in the data analysis on which line of data corresponds to which physical location on the composite test specimen.
- c) Ensure no metallic surfaces are touching one another for each individual strain node. Every node must be securely fixed with distance between its neighboring nodes, otherwise large spikes will dominate the strain results for the shorted nodes and result in unnecessary loss of usable data.
- d) Place 8020 rail on top of insulated strain wires between the alligator clip connections and the cross-rail orange tie connections of the CTR. This will help to ensure the wires will not short over the duration of the shock test. Depending on the magnitude of the shock loading, the CTR has lifted off the deck of the I-beams spanning the AWT in past testing. This can lead to wires touching and negating data collected for affected strain nodes.
- e) Ensure no one is touching exposed metallic surfaces from the bridge to the alligator clip connections.
- f) Power **ON** power supply for bridge. Verify VEX value indicated on power supply display needle matches the desired VEX value for your test run. This VEX value indicated by needle on power supply display will be entered into Signal Express program.
- g) Strain, NI-Max.
 - i) Select the appropriate channel in NI Max, “Test-Panels.”
 - ii) Strain Gages. Will always be channels ai8 to ai15, where ai stands for “Analog Input.” The corresponding nobs are labeled and shown in Figure 18.
 - iii) Potentiometers. The black tabs on each nob allow the potentiometers to be locked once the bridge is properly balanced, i.e. 0V output.

- iv) Use the black nobs shown in the Figure 18 to balance the bridge for each ai channel associated with a strain node. Live strain values in the Test-Panel window should be on the order of μV . An incorrect reading on NI Max (something around $\pm 4\text{ V}$) when completing the zeroing out procedure for the strain gages, indicates either an incomplete connection of the nodes, or two wires of any node touching via their metallic surface.
- h) Signal Express
- i) Select the system function block, “DAQmx Acquire,” on the left side of the project screen shown in Figure 107.

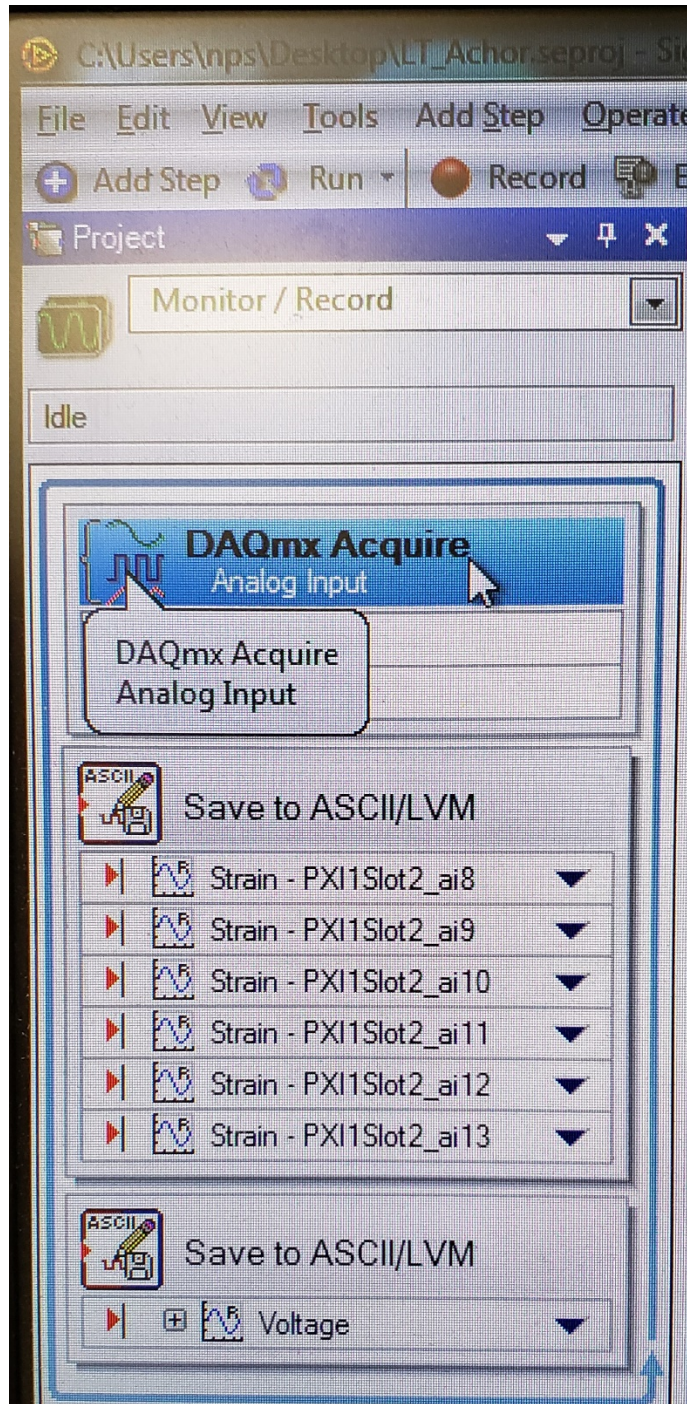


Figure 107. DAQmx Acquire NI function

- 8) Strain. The following window will come up in Figure 108 to establish DAQ settings for strain. Ensure the correct channels being used on the Wheatstone bridge are reflected here under "Channel Settings," Strain.

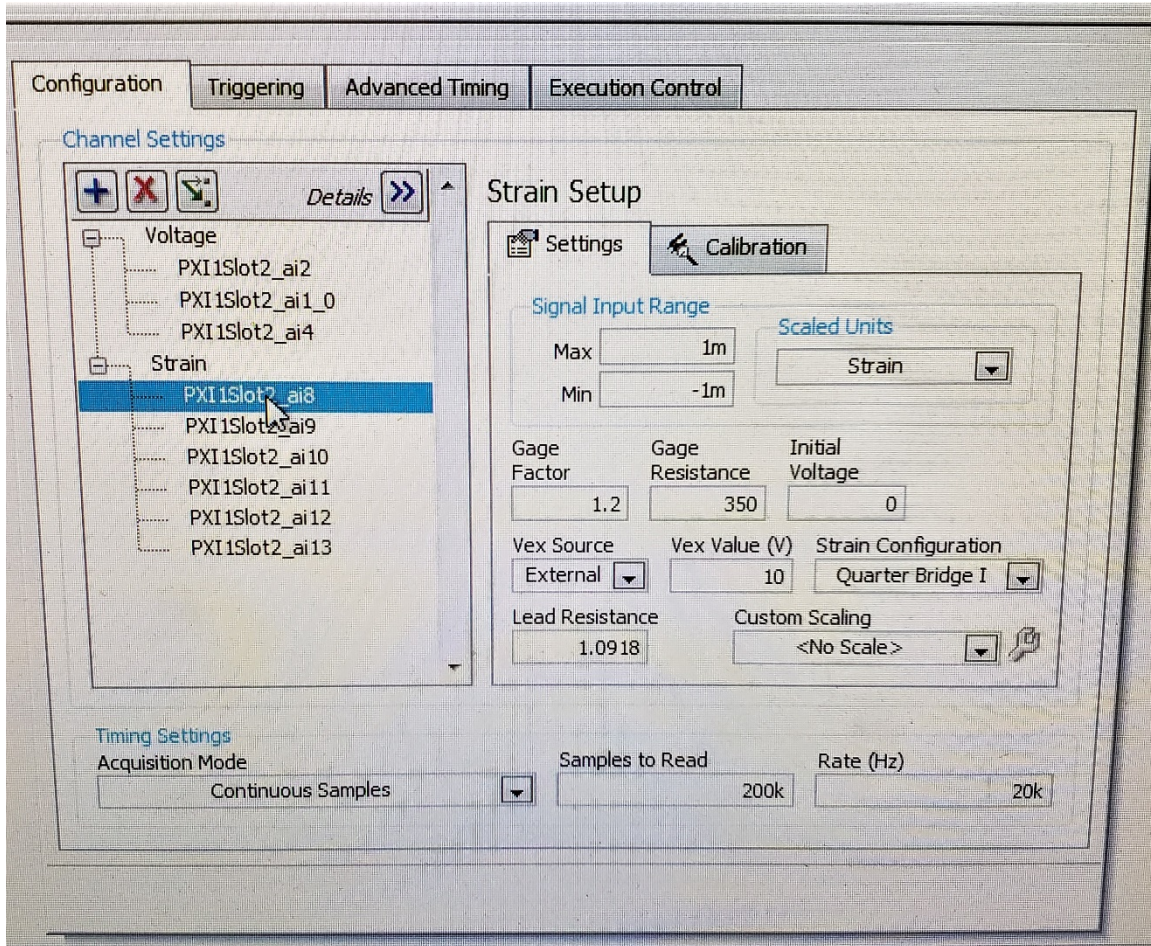


Figure 108. Configuration for strain DAQ in Signal Express

- a) Sample Rate: 200k samples (same for pressure). These are the parameters used for this research, but it can be changed.
- b) Sampling Frequency: 20 kHz (same for pressure). These are the parameters used for this research, but it can be changed.
- c) Gage factor. Input gage factor recorded for the strain gages being used for the composite plate currently being tested. These are listed on the packaging of the strain gages from the manufacturer. Best practice is to keep a digital list via excel spreadsheet of gage factors for each sample plate as well as physically recording the GF on the plate itself.

- d) Quarter Bridge. Ensure “Quarter Bridge Single I” selected for all channels under “Strain Configuration.” This will never change as long as you are using the Wheatstone bridge used in this thesis. Quarter bridge I refers to $\frac{1}{4}$ of the resistors in the circuit is being used by the strain gage. Quarter bridge II refers to the use of a dummy strain gage, which we have never utilized for our test set-up.
- e) V_{EX} . Select “External” for “VEX Source” for excitation voltage (V_{EX} or V_{EX}), which is provided by the HP power supply in Figure 89 of Appendix A.
- f) Under “VEX Value,” enter the Wheatstone bridge power supply voltage value indicated by the orange needle. These two values (orange needle on power supply and “VEX Value” in Signal Express) must always match since the accuracy of the calculated strain by Signal Express hinges on these parameters matching. Refer to Reference 25 for guidance on determining the appropriate VEX value for your application. Using 10V with 350 Ω strain gages is the current setting used to provide stable strain data collection results.
- g) Under “Initial Voltage,” input 0 V. Entering a value of 0V means that the bridge is balanced for every strain wire connected to the bridge (values in NI Max for each channel should be on the order of μ V).
- h) R_G . “Gage Resistance” for the current experimental set-up is 350 Ω , but this correlates to the physical specification by the manufacturer which is written on the packaging that comes with the strain gages.
- i) R_L . Input the calculated “Lead Resistance” value, R_L , as described in the methodology portion of this thesis. The current calculated value of 1.0918 Ω was determined by the total resistance due to the overall length of the wires from the strain gages to the Wheatstone bridge. This value will change if the wire length from the strain gages to the alligator clips changes or if the wire length from the Wheatstone bridge to the alligator clips changes. Since strain is directly calculated from the raw voltage outputs read by the NI DMM and recorded by Signal Express, as explained above, you must ensure this value is correct before collecting data. When lead wire length is generally small, these losses are negligible, but in the case

of our experimental application, the wires are 5.59 m in length to get from the strain gage connections at the composite test plate fully submerged in the AWT back up to the DAQ suite.

- j) One alternative method for strain gage data collection is to have NI collect the raw V_o values from the Wheatstone bridge. This would allow you to assign these strain parameters in a MATLAB code after the data is collected, and then calculate the corresponding strain values through Equation 3. This could help to avoid the situation of having unusable data if you forgot to properly change one of these settings in Signal Express prior to pressing record.
- 9) **Pressure.** The following window will come up shown in Figure 109 to establish DAQ settings for pressure. Ensure the correct channels that the BNC cables are connected to on the BNC-2110 are added here under “Channel Settings,” Voltage.

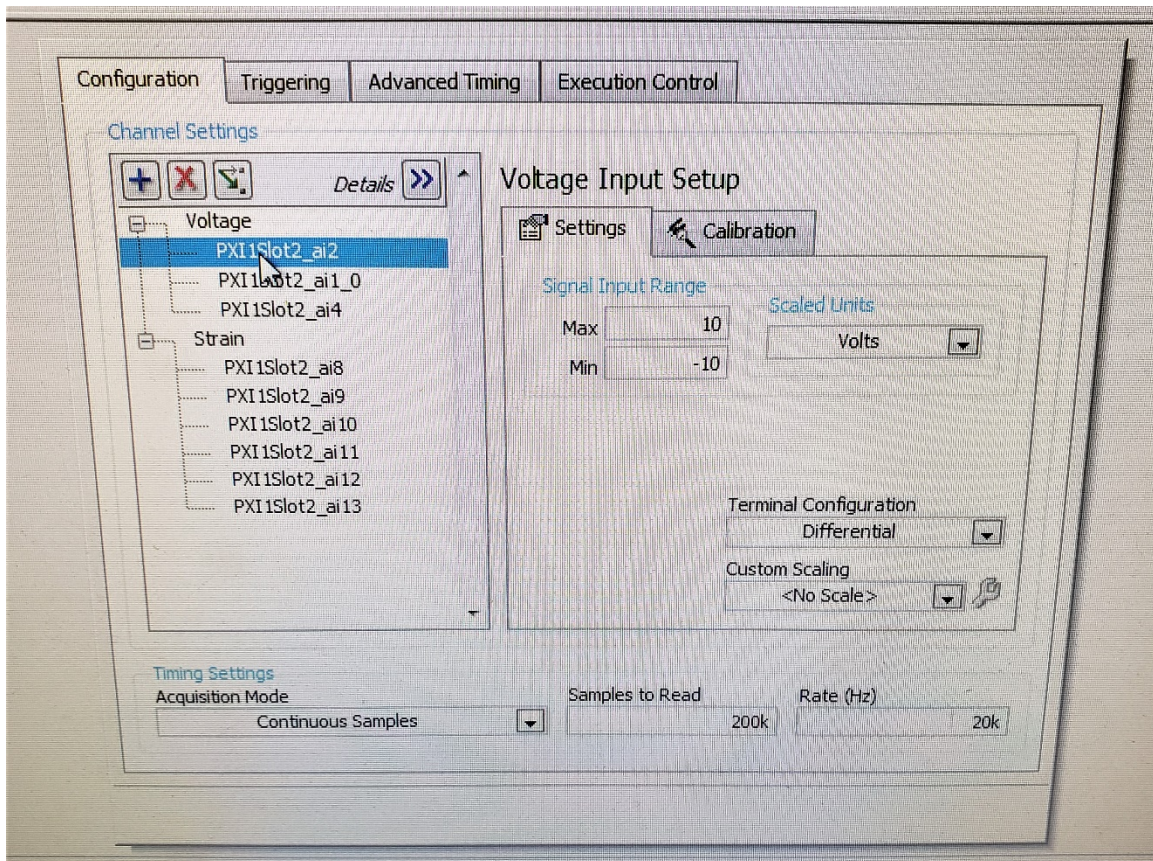


Figure 109. Configuration for pressure DAQ in Signal Express

10) **File saving, strain.** Click on the button on the left side of the screen in Signal Express as shown in Figure 110 to start the save process prior to DAQ.

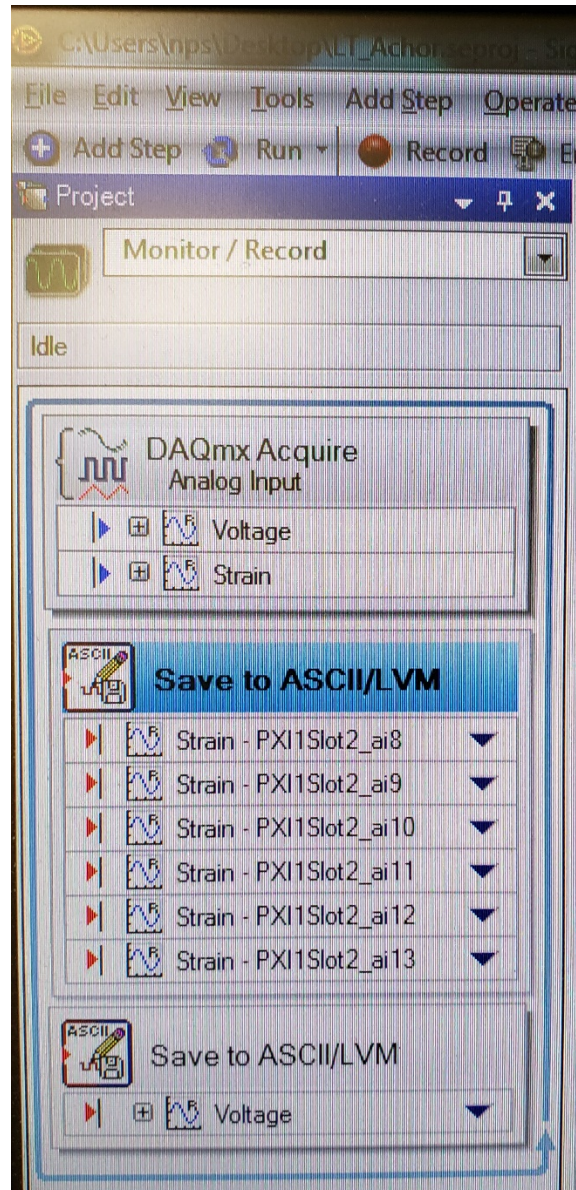


Figure 110. Save function for Signal Express

a) After clicking on the box in blue in Figure 110 for strain, the following window will show up as seen in Figure 111.

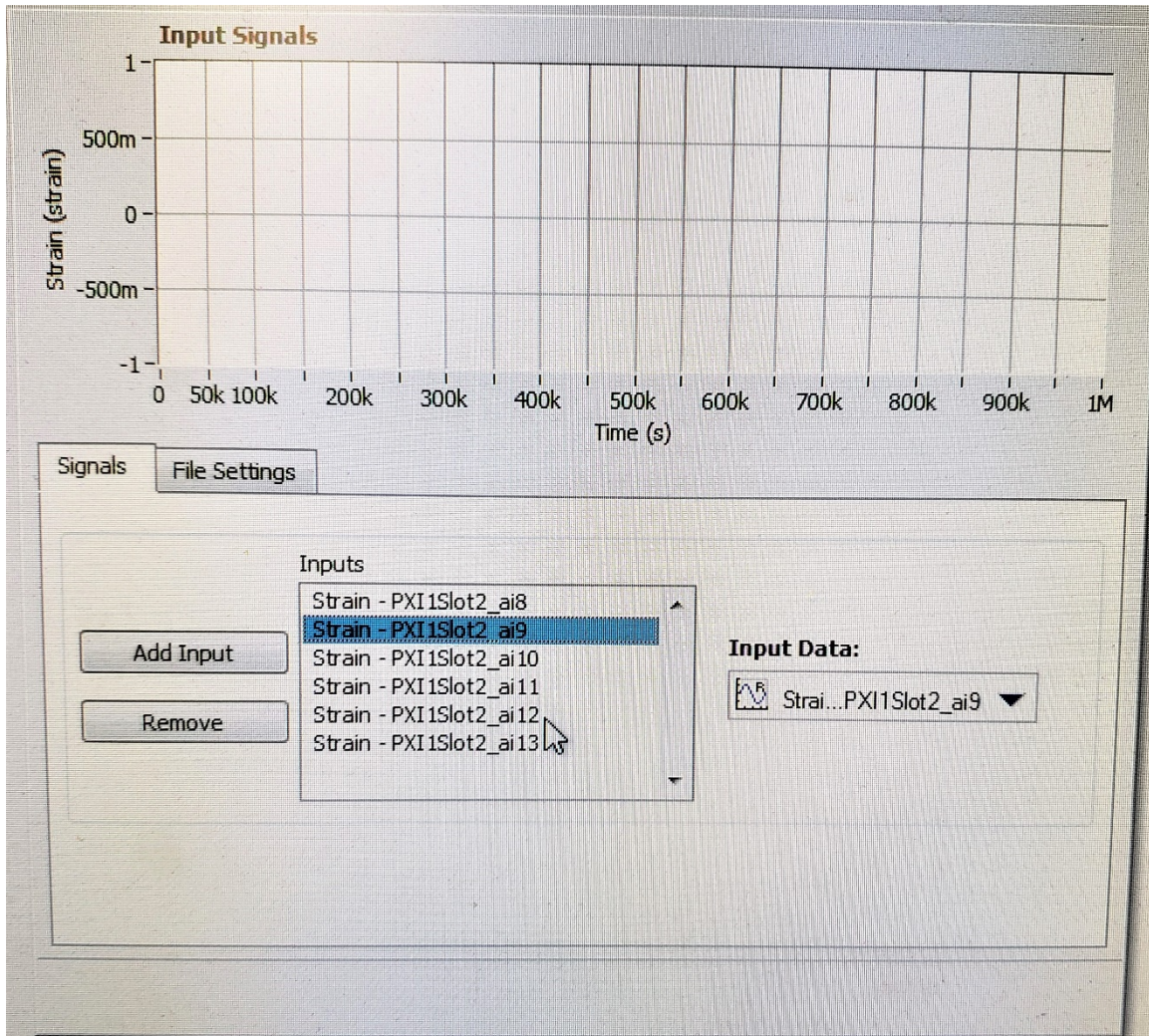


Figure 111. Signal save settings, strain, Signal Express

- i) Under “Signals,” ensure all ai signals are properly selected to match the nodes being used on the Wheatstone bridge.
- ii) Click, “File Settings” as shown in Figure 112.
- iii) Under “Export File Path,” ensure folder and subfolders are named in a way that will help remind you the test settings used for that test run and corresponding DAQ. This thesis used a simple “s.1” as the 1st assigned file name
- iv) Under, “If file already exists,” ensure “Next available file name, per iteration” is selected. Depending on the sample rate and frequency set,

- v) Under, “Export file type,” ensure “Generic ASCII (.txt)” is selected. This makes for easy data analysis through MATLAB® import and analysis code.
- vi) Under, “Delimiter,” select “Tab”
- vii) Ensure “Include Signal Names” is **NOT** selected.
- viii) Under, “X Value columns,” select, “One Column Only.”
- ix) Under, “Time Axis Preference,” select, “Absolute Time”

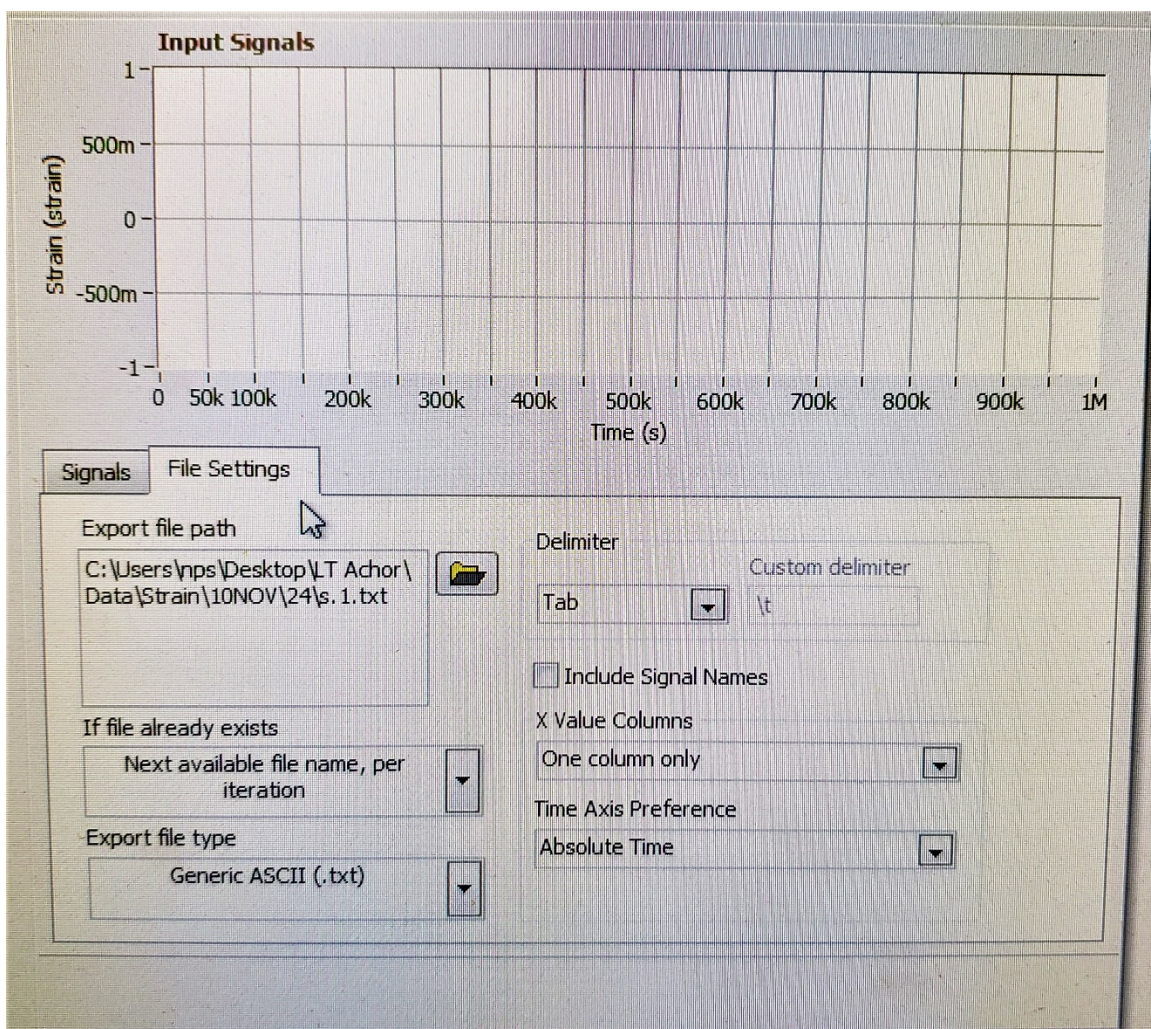


Figure 112. File save settings, strain, Signal Express

- 11) **File saving, pressure.** Follow the same general steps outlined above for pressure file saving DAQ.
- 12) Ensure that once you prepare to collect data for the next test run that you re-map the file location so that you do not overwrite the data just collected.
- 13) Ensure that the file saving and DAQ “blocks” shown in Figure 85 are all nested within the same loop as indicated in this figure by the single blue loop around all three distinct system function blocks.
- 14) When ready to record data (once CASPUR is reading 250 psi on LPG-2), press the red record button in the top left toolbar, and the following window will come up where the appropriate channels for DAQ must be selected. This is shown in Figure 113. Once the “Ok” button is pressed in Figure 113, data acquisition is now occurring.

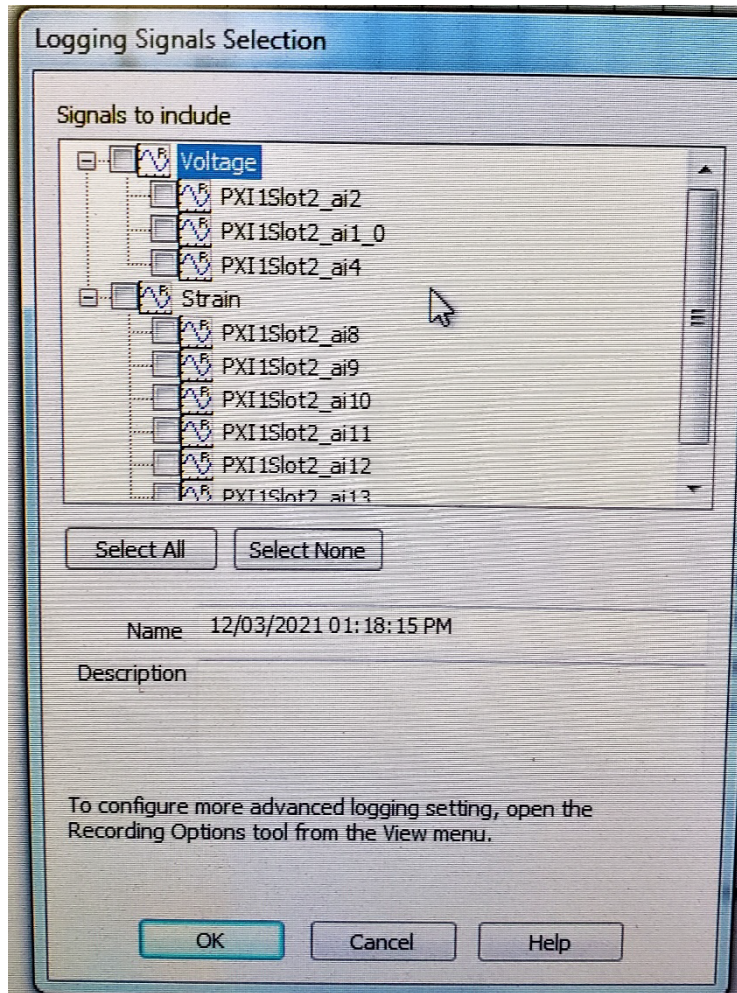


Figure 113. Signal logging selection for DAQ in Signal Express

15) CASPUR activation

- a) Ensure all personnel in WA122-A are wearing safety glasses and double hearing protection prior to pressurizing CASPUR.
- b) Begin fill process by 50 psi increments up to 250 psi, 10 psi increments from 250 psi to 280 psi, and in 5 psi increments from 280 psi until rupture disk failure in the following way:
 - i) Ensure all CASPUR valves are closed, and HPG-1 and LPG-2 gages read 0 psi.
 - ii) Open CGV-1 slightly until tank pressure registers on HPG-1 of the regulator. Record the starting pressure of the compressed gas tank in log.

- iii) Open RV-2 until 50 psi registers between it and 2WV-4.
- iv) Open 2WV-4 slowly and gradually all the way to open, and then increase opening of RV-2 until LPG-2 shows a pressure of 50 psi downstream of the second stage regulator. At 50 psi increments up to 150 psi, verify that no leaks are present from the two critical areas mentioned above. If leaking exists at one of the two critical locations mentioned in the earlier section of this Appendix B, the leak check is considered UNSAT. Small bubbles from the threaded two-inch fittings after the tube to NPT fitting is acceptable, if no rapid and significant loss of pressure displays at LPG-2.
- v) If the leak check is UNSAT, depressurize the system in the same manner previously described in this Appendix B.
- vi) If the leak check passes, follow the pressure increment changes outlined in 15.b of this Appendix B.
- vii) When the system reaches 250 psi on LPG-2, press “Okay” in the record function of Signal Express.
- viii) Close 2WV-4 upon failure of rupture disk.
- ix) Depressurize system as previously described in this Appendix B prior to retrieving carriage from AWT.
- x) Prior to retrieving the CTR, power off the Wheatstone bridge power supply shown in Figure 89.
- xi) Once data export is complete from the DAQ, ensure the NI suite is powered off through the windows “Shut Down” function. **NEVER** power off the system from the DAQ power button shown in Figure 97.

THIS PAGE INTENTIONALLY LEFT BLANK

APPENDIX C. STRAIN RESULTS

The following figures provide the total strain time history results collected for every test run conducted prior to failure of the composite plate during this research. Raw non-normalized maximum strain values collected are also plotted for every test-run through failure.

A. SAMPLE 3, THREE-LAYER COMPOSITE, WB, STRAIN

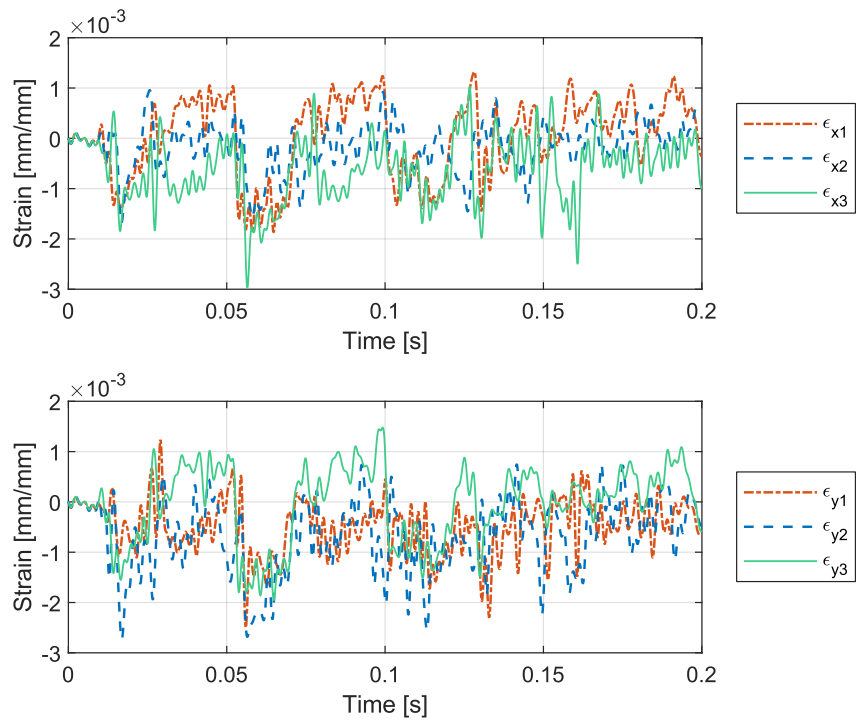


Figure 114. Strain response, WB Sample 3 (0-90-0°), R = 0.61 m, Run 1

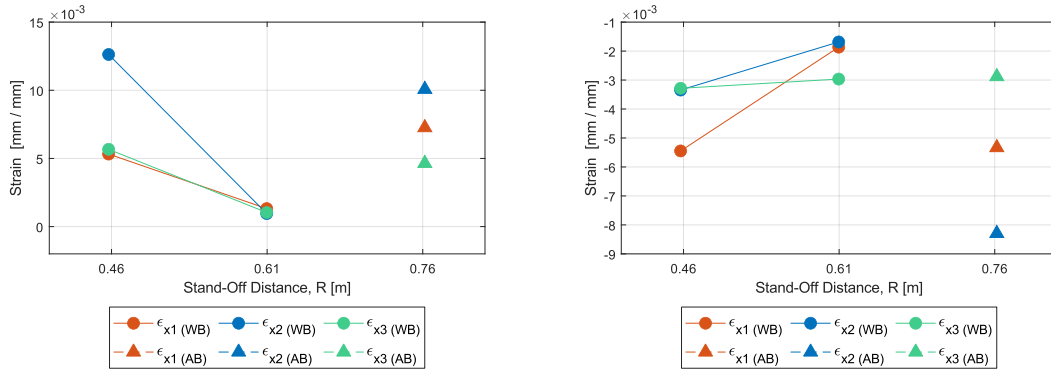


Figure 115. X-direction, maximum strain trends, AB and WB, 0-90-0: tension (left), compression (right)

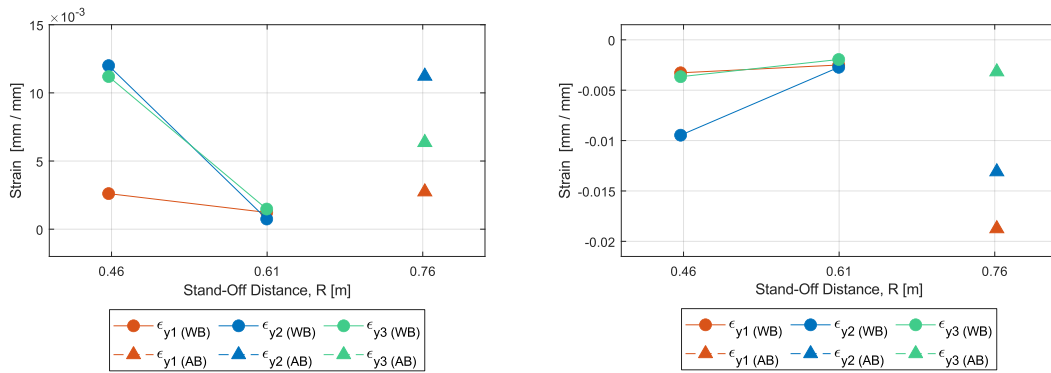


Figure 116. Y-direction, maximum strain trends, AB and WB, 0-90-0: tension (left), compression (right)

B. SAMPLE 6, FOUR-LAYER COMPOSITE, WB, STRAIN

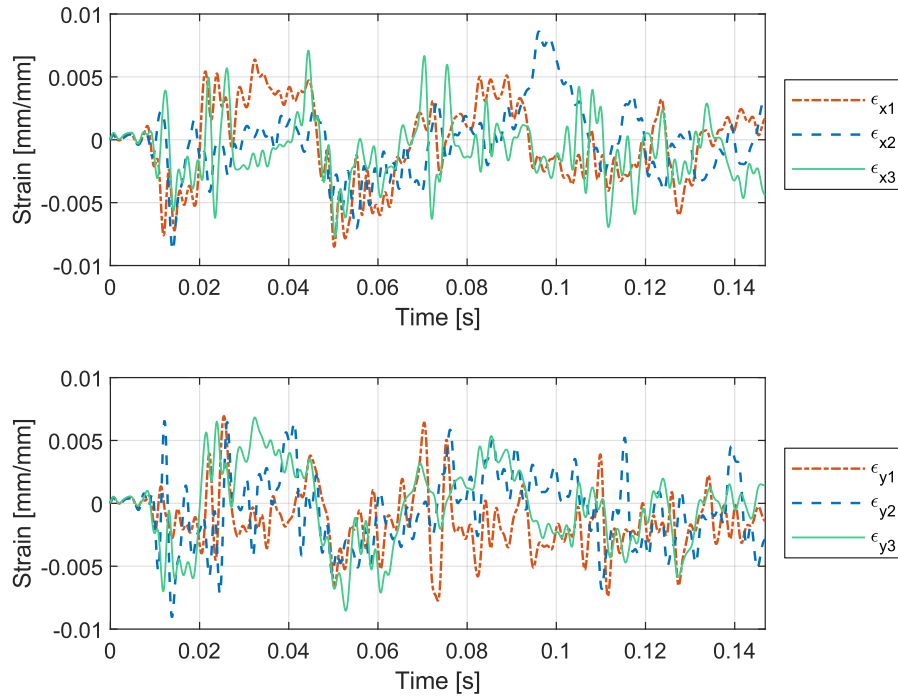


Figure 117. Strain response, WB Sample 6 (0-90-90-0°), R = 0.61 m, Run 1

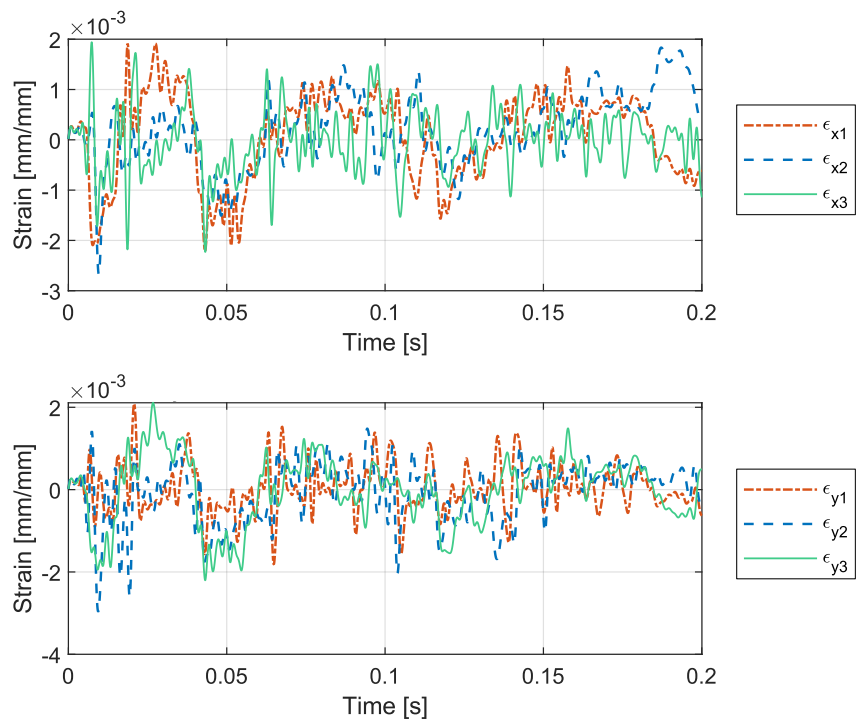


Figure 118. Strain response, WB Sample 6 (0-90-90-0°), R = 0.46 m, Run 2

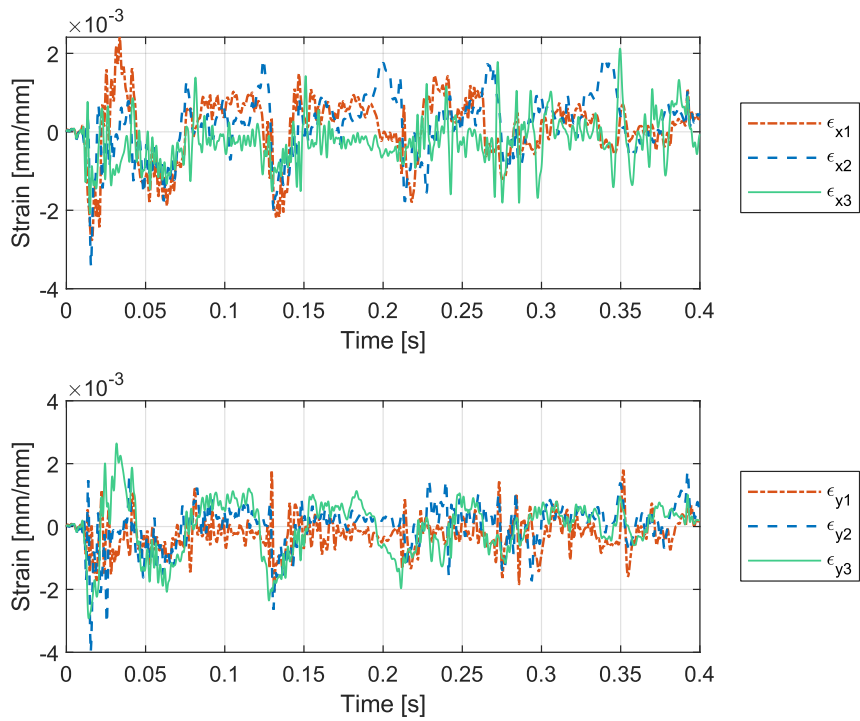


Figure 119. Strain response, WB Sample 6 (0-90-90-0°), R = 0.3 m, Run 3

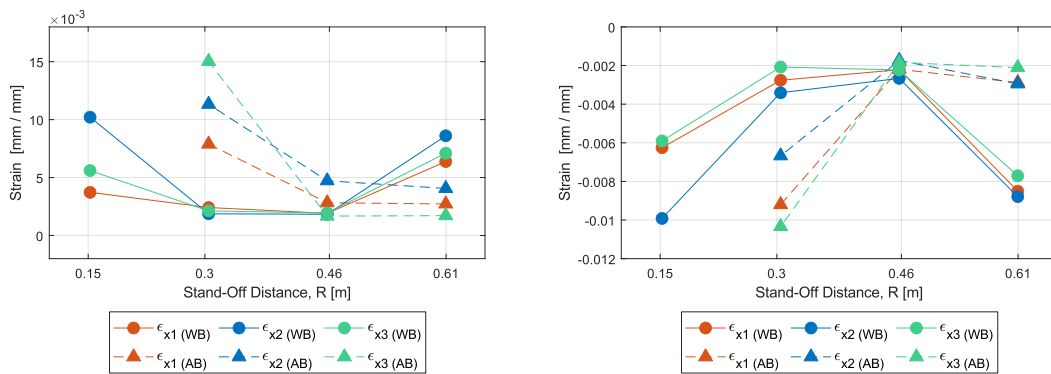


Figure 120. Raw x-direction, maximum strain trends, AB and WB, 0-90-90-0: tension (left), compression (right)

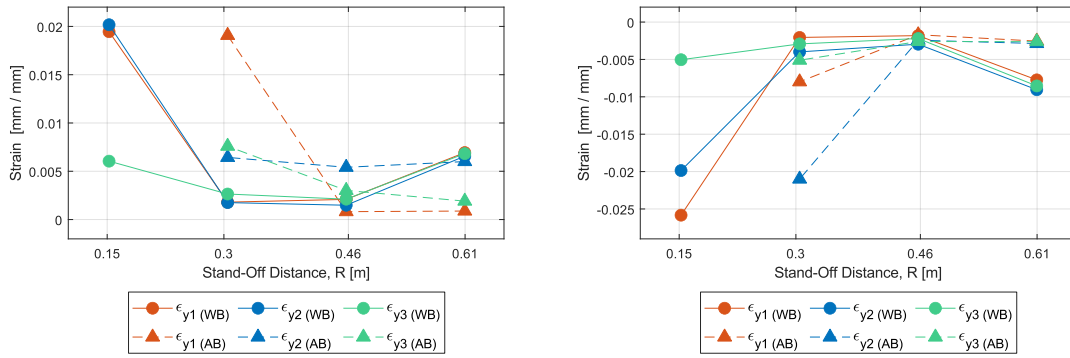


Figure 121. Raw y-direction, maximum strain trends, AB and WB, 0-90-90-0: tension (left), compression (right)

C. SAMPLE 7, FOUR-LAYER COMPOSITE, AB, STRAIN

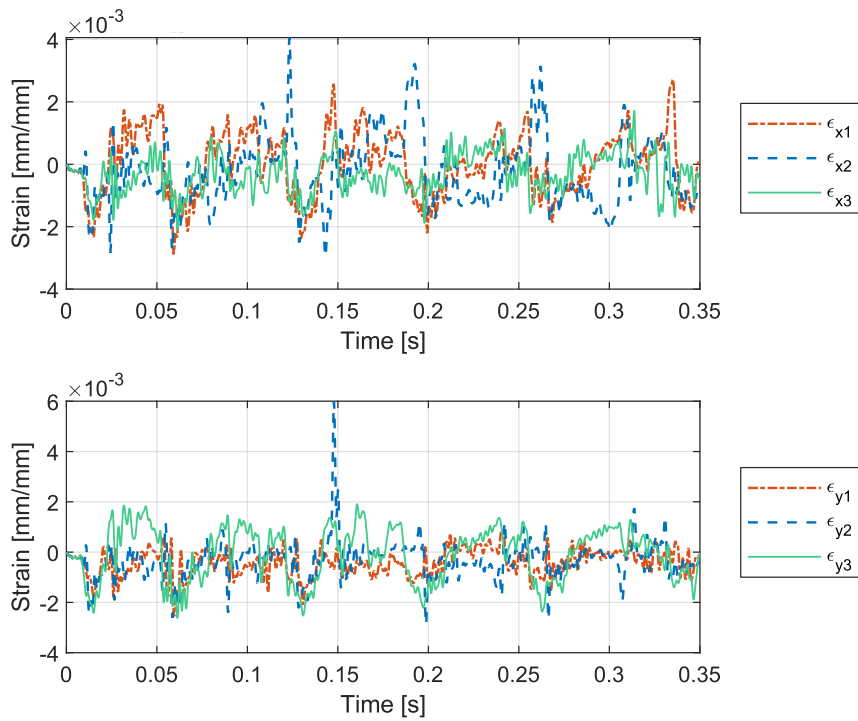


Figure 122. Strain response, AB Sample 7 (0-90-90-0°), R = 0.61 m, Run 1

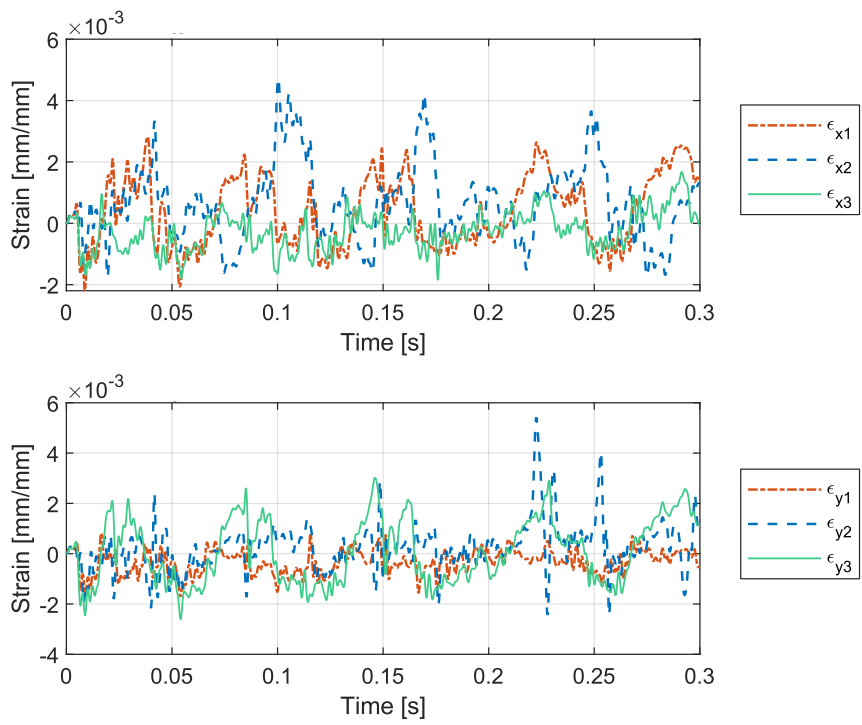


Figure 123. Strain response, AB Sample 7 (0-90-90-0°), R = 0.46 m, Run 2

THIS PAGE INTENTIONALLY LEFT BLANK

APPENDIX D. PRESSURE RESULTS

Complete pressure characterization results are provided here for every test run conducted in this research. Pressure profiles for the standard layouts are included for every test run, excluding the failure run.

A. LINEAR LAYOUT PRESSURE RESULTS

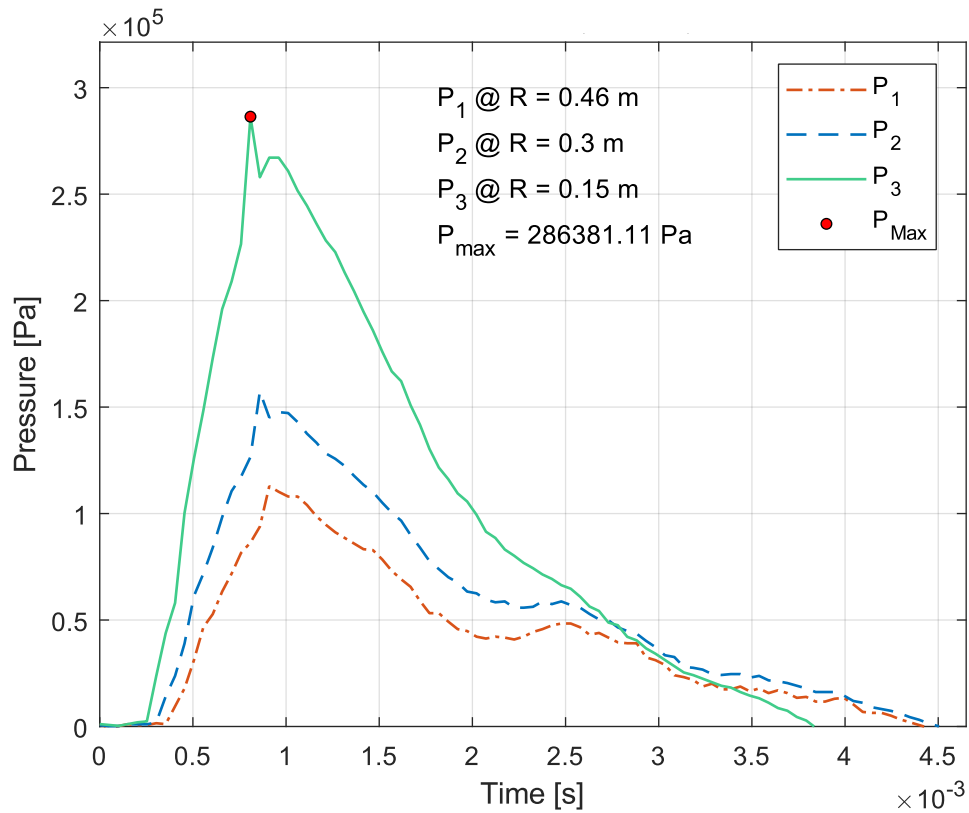


Figure 124. Pressure characterization, linear layout, $R = 0.46$ m, Run 2

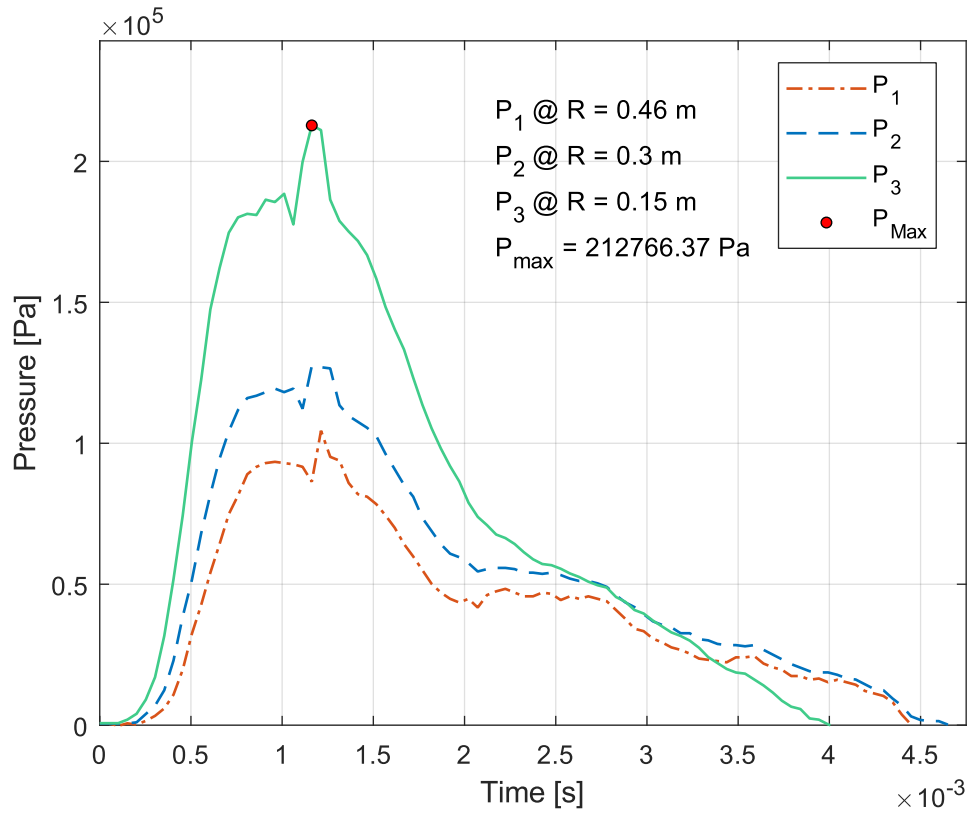


Figure 125. Pressure characterization, linear layout, R = 0.46 m, Run 3

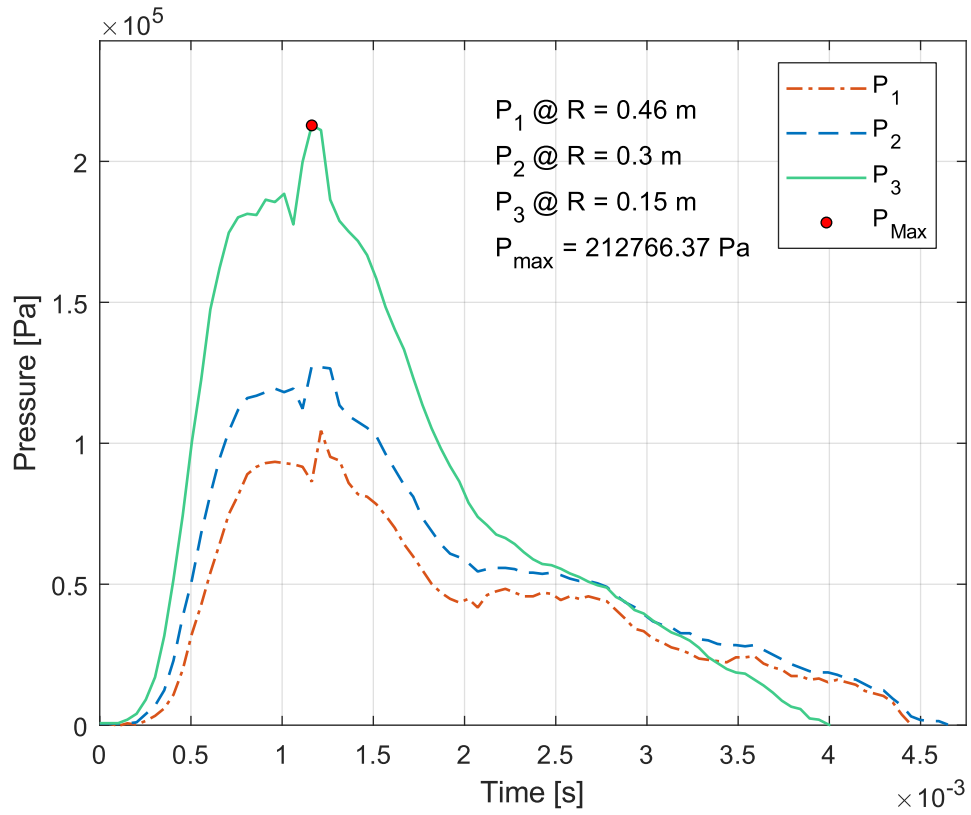


Figure 126. Pressure characterization, linear layout, R = 0.46 m, Run 4

B. TRIANGULAR LAYOUT PRESSURE RESULTS

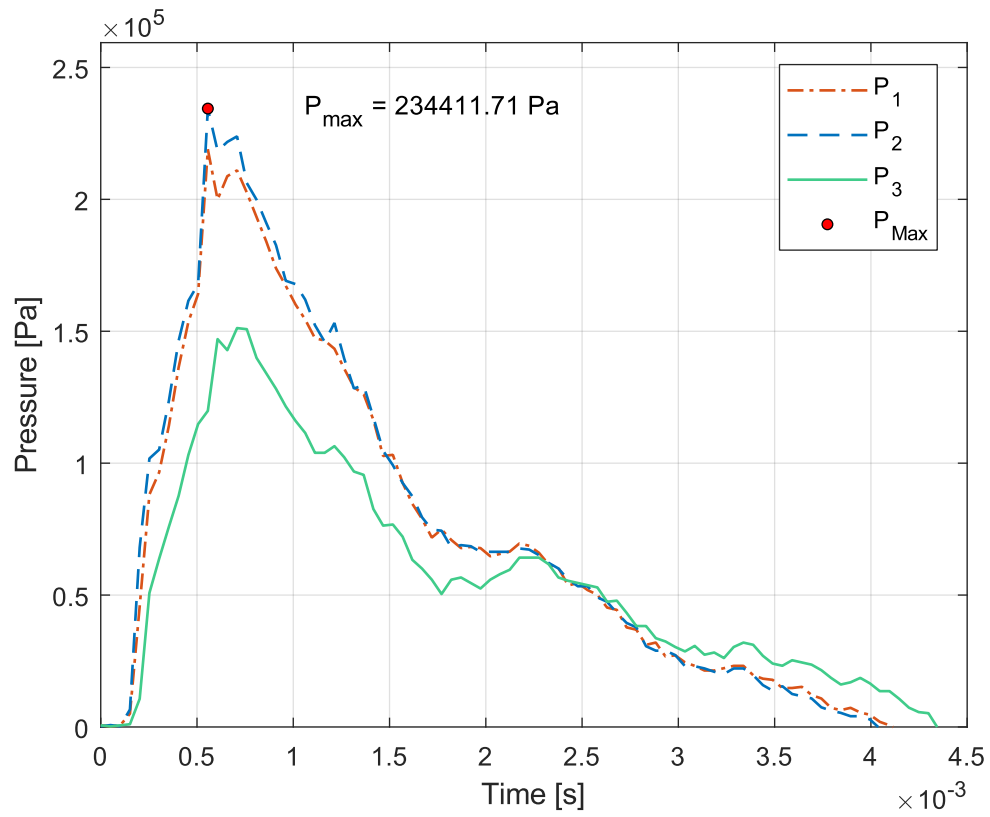


Figure 127. Pressure characterization, triangular layout, R = 0.3 m, Run 2

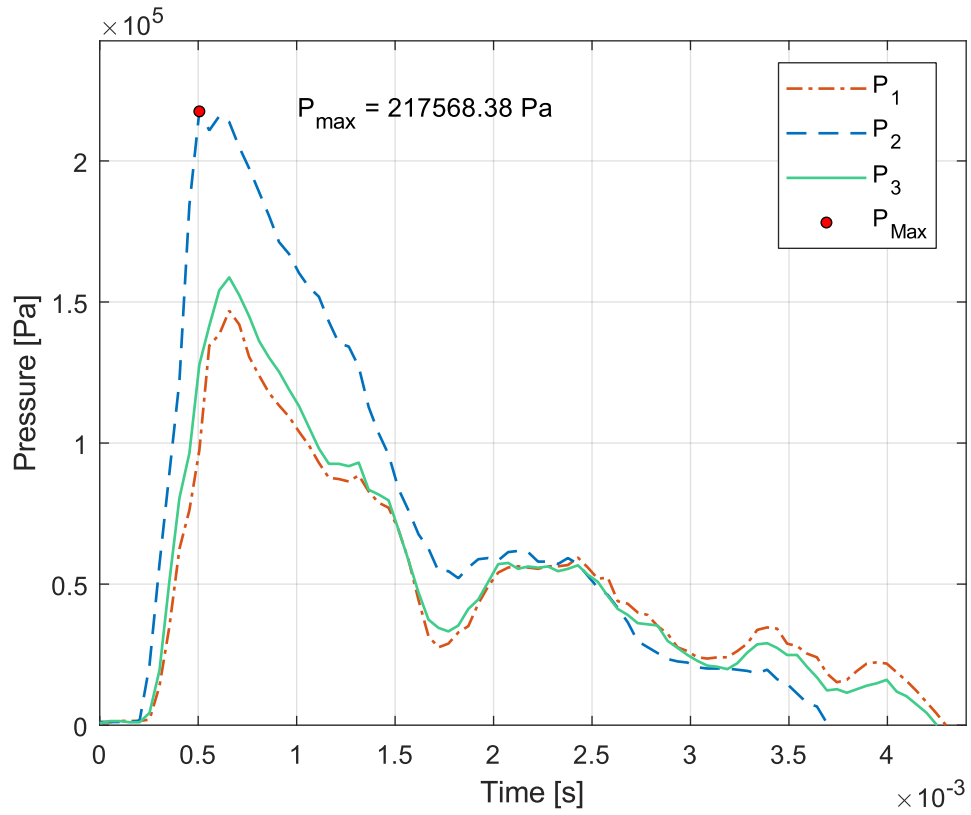


Figure 128. Pressure characterization, triangular layout, R = 0.3 m, Run 3

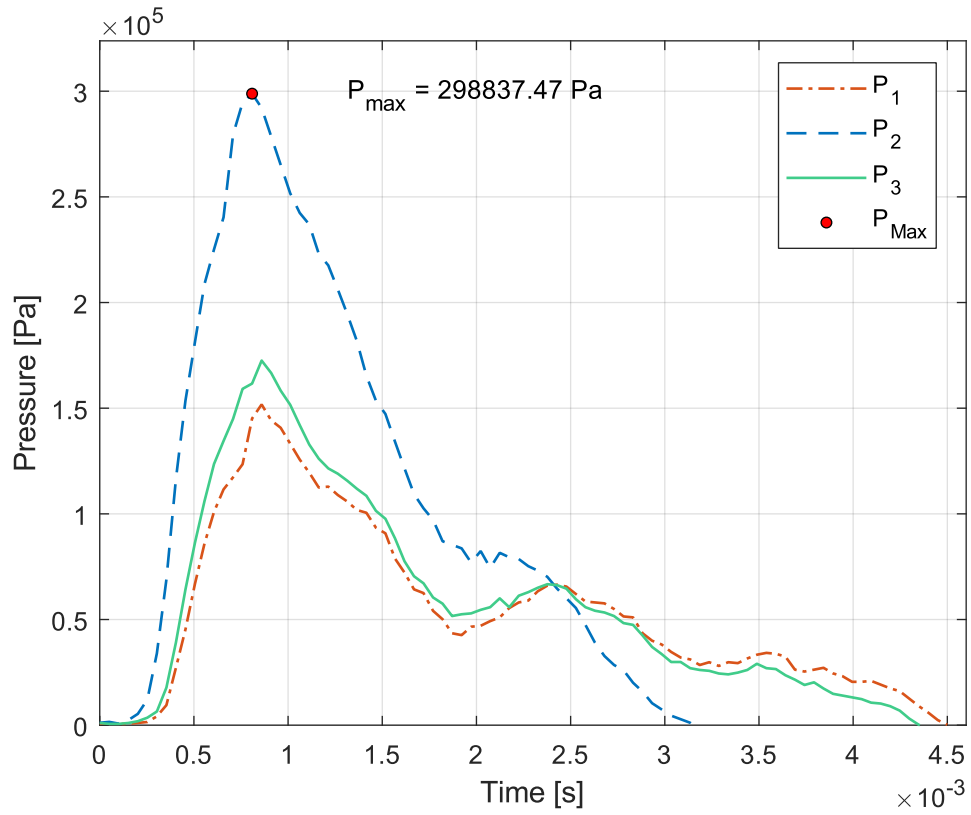


Figure 129. Pressure characterization, triangular layout, R = 0.3 m, Run 4

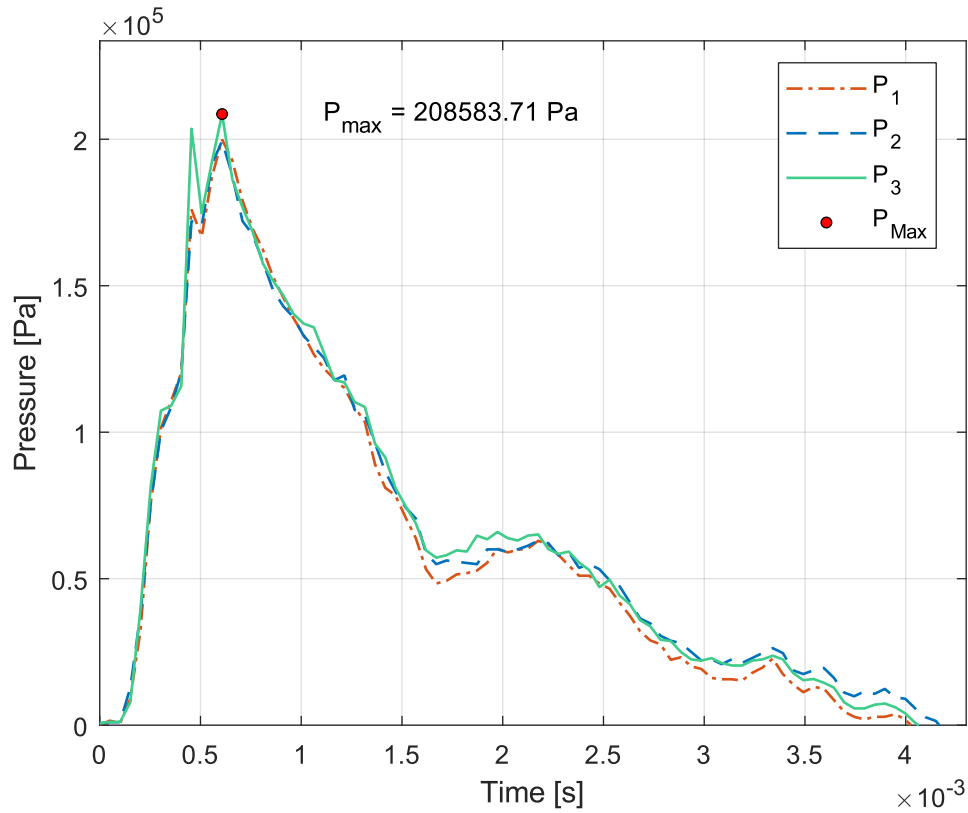


Figure 130. Pressure characterization, triangular layout, R = 0.3 m, Run 5

C. STANDARD LAYOUT PRESSURE RESULTS

1. Sample 3, Three-layer composite, WB, Pressure

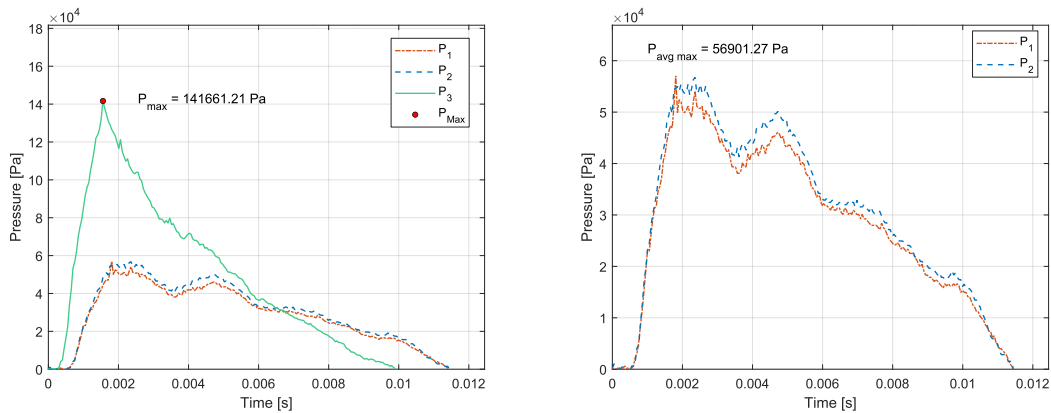


Figure 131. Overall pressure profile (left), plate failure loading (right), WB Sample 3, Run 1, R = 0.61 m

2. Sample 6, Four-layer composite, WB, Pressure

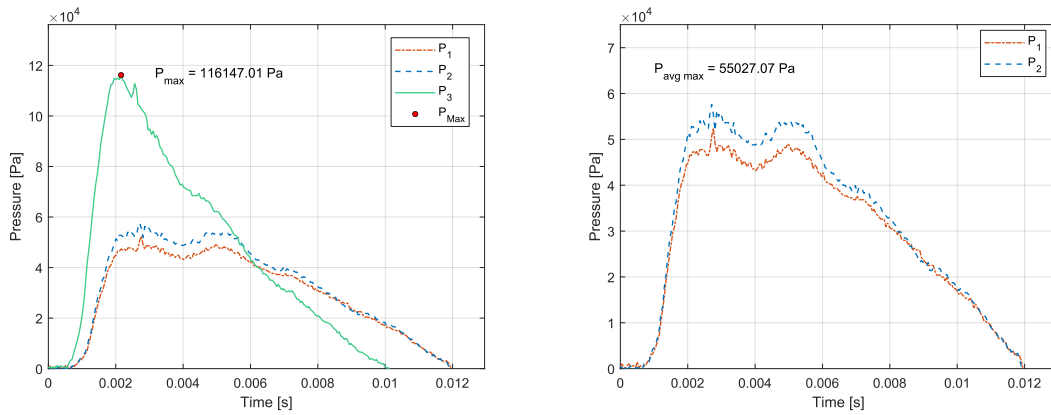


Figure 132. Overall pressure profile (left), plate failure loading (right), WB
Sample 6, Run 1, $R = 0.61 \text{ m}$

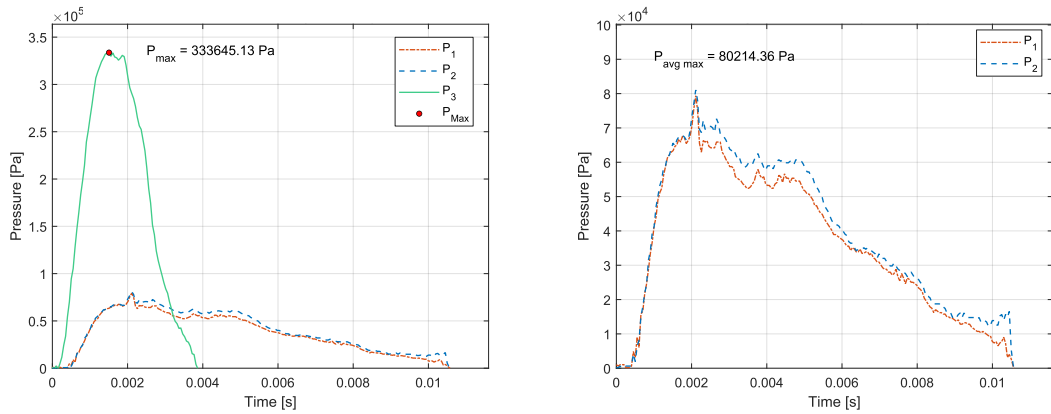


Figure 133. Overall pressure profile (left), plate failure loading (right), WB
Sample 6, Run 2, $R = 0.61 \text{ m}$

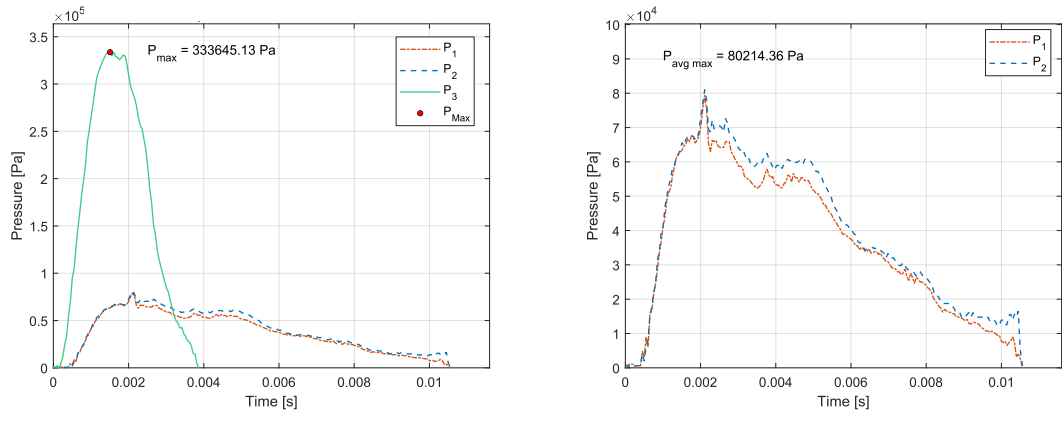


Figure 134. Overall pressure profile (left), plate failure loading (right), WB Sample 6, Run 3, R = 0.46 m

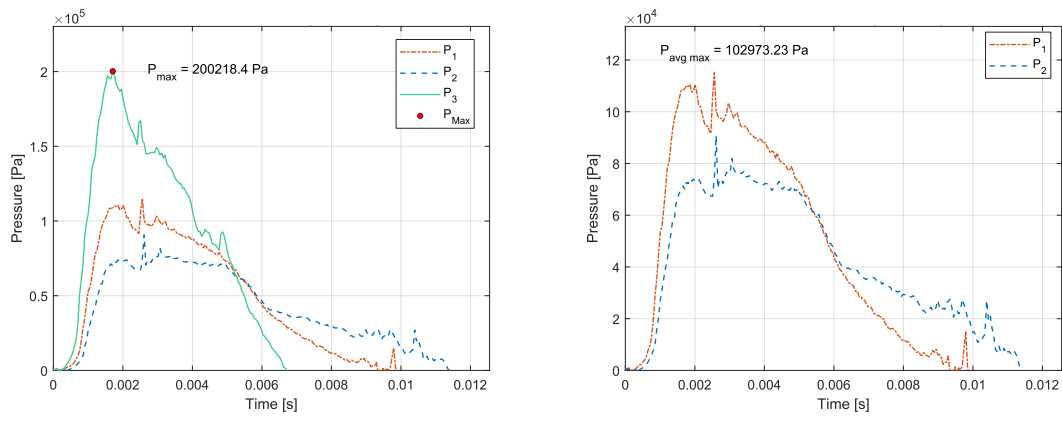


Figure 135. Overall pressure profile (left), plate failure loading (right), WB Sample 6, Run 4, R = 0.3 m

3. Sample 7, Four-layer composite AB, Pressure

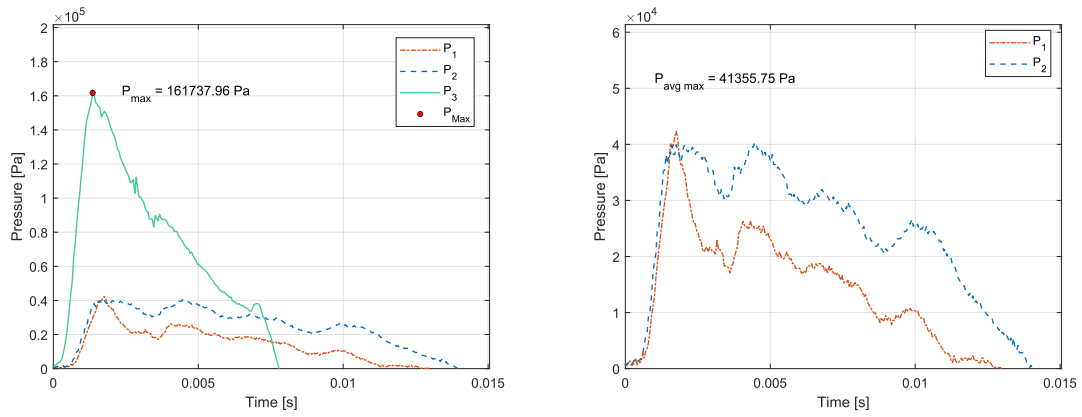


Figure 136. Overall pressure profile (left), plate failure loading (right), AB Sample 7, Run 1, $R = 0.61$ m

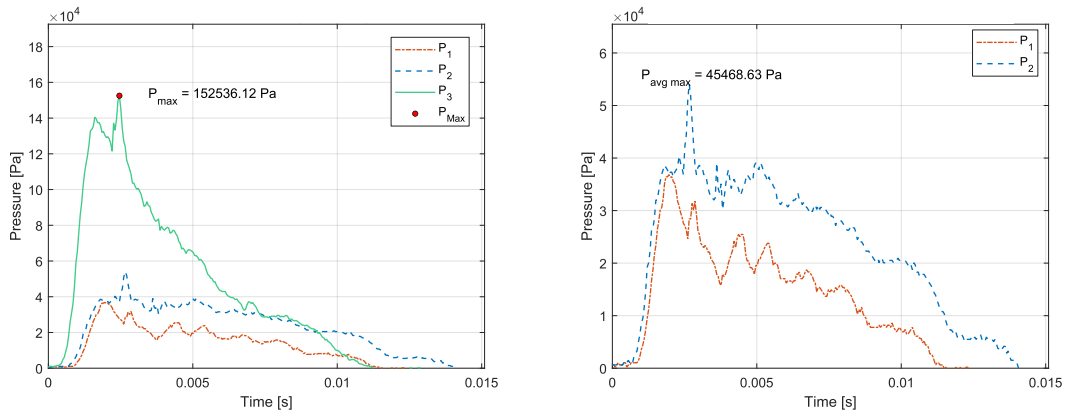


Figure 137. Overall pressure profile (left), plate failure loading (right), AB Sample 7, Run 2

LIST OF REFERENCES

- [1] Tran, P., Wu, C., Saleh, M., Neto, L.B., Nguyen-Xuan, H., Ferreira, A.J.M., 2021, “Composite structures subjected to underwater explosive loadings: A comprehensive review,” *Composite Structures*, 263, 29. <http://dx.doi.org/10.1016/j.comstruct.2021.113684>.
- [2] Mouritz, A.P., 2019, “Advances in understanding the response of fibre-based polymer composites to shock waves and explosive blasts,” *Composites Part A: Applied Science and Manufacturing*, 125: 433–61. <http://dx.doi.org/10.1016/j.compositesa.2019.105502>.
- [3] Leblanc, J., Shukla, A., 2014, “Underwater Explosive Response of Submerged, Air-Backed Composite Materials: Experimental and Computational Studies,” *Blast Mitigation: Experimental and Numerical Studies*. Springer New York, NY. https://doi.org/10.1007/978-1-4614-7267-4_5
- [4] Costanzo, F. A., 2010, “Underwater Explosion Phenomena and Shock Physics,” Proceedings of the IMAC-XXVIII, Jacksonville, FL, February 1–4, 2010. *Structural Dynamics, Volume 3*, 2011–05-12, pp. 917–938. Springer New York, NY. https://doi.org/10.1007/978-1-4419-9834-7_82
- [5] Keil, A.H., 1961, “The Response of Ships to Underwater Explosions,” Annual Meeting, Society of Naval Architects and Marine Engineers, New York, NY, November 16–17, 1961. <https://apps.dtic.mil/sti/pdfs/AD0268905.pdf>
- [6] Reid, W. D., 1996, “Response of Surface Ships to Underwater Explosions,” DSTO Aeronautical and Maritime Research Laboratory Report, DSTO-GD-0109. <https://apps.dtic.mil/sti/pdfs/ADA326738.pdf>
- [7] Nagesh, Gupta, N.K., 2021, “Response of thin walled metallic structures to underwater explosion: A review,” *International Journal of Impact Engineering*, Volume 156, Issue C, 13. <https://doi.org/10.1016/j.ijimpeng.2021.103950>
- [8] Kwon, Y.W., Owens, A.C., Kwon, A.S., Didoszak, J.M., 2010, “Experimental Study of Impact on Composite Plates with Fluid-Structure Interaction,” *The International Journal of Multiphysics*, Volume 4, No. 3, pp. 259–271. <https://doi.org/10.1260/1750-9548.4.3.259>
- [9] U.S. Department of the Navy, 2018, “APPENDIX D: Acoustic and Explosive Concepts,” *Environmental Impact Statement/Overseas Environmental Impact Statement*, Atlantic Fleet Training and Testing, September, 2018, Appendix D. <https://media.defense.gov/2020/May/13/2002299494/-1/-1/1/APPENDIX%20D%20AFTT%20FEIS%20ACOUSTIC%20AND%20EXPLOSIVE%20CONCEPTS.PDF>

- [10] Mouritz, A.P., Saunders, D.S., 1993, “The Damage and Failure of GRP Laminates by Underwater Explosion Shock Loading,” *5th Australian Aeronautical Conference*, September 13–15, 1993, DSTO Report No. ADA283793. <https://apps.dtic.mil/sti/pdfs/ADA283793.pdf>
- [11] Arora, H., Hooper, P.A., Dear, J.P., 2011, “The Effects of Air and Underwater Blast on Composite Sandwich Panels and Tubular Laminate Structures,” *Society for Experimental Mechanics 2011*, Volume 52, pp. 59–81. DOI: 10.1007/s11340-015-0038-9
- [12] Rajendran, R., Lee, J.M., 2008, “A Comparative Damage Study of Air- and Water-Backed Plates Subjected To Non-Contact Underwater Explosion,” *International Journal of Modern Physics B*, Volume 22, No. 9–11 (2008), 1311–1318. ISSN/ISSN: 02179792
- [13] LiVolsi, F., 2014, “Response of Marine Composites Subjected to Near Field Blast Loading,” Master’s Thesis, University of Rhode Island.
- [14] Schiffer, A., Tagarielli, V.L., 2012, “The response of rigid plates to blast in deep water: fluid-structure interaction experiments,” *Proceedings of the Royal Society A*, Volume 468, No. 2145, pp. 2807–2828 (2012). <http://www.jstor.org/stable/41727109>
- [15] Avachat, S., Zhou, M., 2014, “High-speed digital imaging and computational modeling of dynamic failure in composite structures subjected to underwater impulsive loads,” *International Journal of Impact Engineering*, Volume 77, pp. 147–165 (2015). <https://doi.org/10.1016/j.ijimpeng.2014.11.008>
- [16] Schiffer, A., Tagarielli, V.L., 2014, “One-dimensional response of sandwich plates to underwater blast: Fluid-structure interaction experiments and simulations,” *International Journal of Impact Engineering*, Volume 71, pp. 34–49 (2014). <https://doi.org/10.1016/j.ijimpeng.2014.04.001>
- [17] Schiffer, A., Tagarielli, V.L., 2014, “The response of circular composite plates to underwater blast: Experiments and modelling,” *Journal of Fluids and Structures*, Volume 52, pp. 130–144 (2015). <https://doi.org/10.1016/j.jfluidstructs.2014.10.009>
- [18] Avachat, S., Zhou, M., 2017, “Novel experimental and 3-D Multiphysics computational framework for analyzing deformation and failure of composite laminates subjected to water blasts,” *International Journal of Impact Engineering*, Volume 106, pp. 223–237 (2017). <https://doi.org/10.1016/j.ijimpeng.2017.04.017>
- [19] Calister, W.D. Jr., Rethwisch, D.G., 2014, “Materials Science and Engineering: An Introduction, 9th Edition” Wiley, Hoboken, NJ, Chapter 16, ISBN: 0470419970.
- [20] Kwon, Y., private correspondence November 2021.

- [21] Crow, E.N., 2020, “Failure of Composite Plates Subjected to Shock Loading,” Masters Thesis, Naval Postgraduate School, Monterey, CA.
- [22] National Instruments, 2020, “Measuring strain with strain gages” *White Paper: 07*, Accessed online November 4th, 2021. <https://www.ni.com/en-us/innovations/white-papers/07/measuring-strain-with-strain-gages.html>
- [23] Omega Engineering, 1999, “Practical Strain Gage Measurements,” *Application Note 290-1*, Agilent Technologies, 1999. https://www.omega.co.uk/techref/pdf/StrainGage_Measurement.pdf
- [24] Calmont Wire & Cable, “Solid and Stranded Conductor AWG Chart” Accessed online, November 4th, 2021. <https://www.calmont.com/resources/wire-gauge-table/>
- [25] National Instruments, “Engineer’s Guide to Accurate Sensor Measurements,” *White Paper 25188*. Accessed online with an account, November 4th, 2021, https://www.ni.com/gate/gb/GB_EKITENGGUIDEASM/US
- [26] PCB Piezotronics INC., 2019, “Model 138A10 ICP® Pressure Sensor Installation and Operating Manual” *Manual 21354*, Rev E, ECN 5052. Accessed online, November 4th, 2021. http://www.pcb.com/contentStore/docs/pcb_corporate/pressure/products/manuals/138a10.pdf
- [27] Air Products, 2019, “Safety Gram 7: Liquid Nitrogen,” Accessed online, November 4th, 2021. <https://www.airproducts.com/company/sustainability/safetygrams>
- [28] Linde, brochures, “Praxair Specialty Gases and Equipment Solutions” Accessed online, November 4th, 2021. https://www.lindedirect.com/docs/default-source/brochures/specialty-gas-electronics/praxair_specialty_gas_and_equipment_solutions.pdf
- [29] Ansel, T., private communication November 2021.
- [30] Hung, C.F., Hsu, P.Y., Hwang-Fuu, J.J., “Elastic shock response of an air-backed plate to underwater explosion,” *International Journal of Impact Engineering*, Volume 31, pp. 151–168 (2005).

THIS PAGE INTENTIONALLY LEFT BLANK

INITIAL DISTRIBUTION LIST

1. Defense Technical Information Center
Ft. Belvoir, Virginia
2. Dudley Knox Library
Naval Postgraduate School
Monterey, California